GEOCHEMICAL AND CLAY MINERALOGICAL CHARACTERISTICS OF THE WOODFORD SHALE, PAYNE COUNTY, OKLAHOMA

by

SULTAN A. ALKHAMMALI

B.S., King Saud University, 2009

A THESIS

submitted in partial fulfillment of the requirements for the degree

MASTER OF SCIENCE

Department of Geology
College of Arts and Sciences

KANSAS STATE UNIVERSITY
Manhattan, Kansas

2015

Approved by:

Major Professor
Dr. Sambhudas Chaudhuri

Copyright

Abstract

Chemical and mineralogical compositions of < 2 μm-size fraction clays of the shale source rocks of Devonian-Mississippian age in northern Oklahoma were determined to find any link between the minerals and the generation of petroleum. Ten samples of clay separates were analyzed for their mineral composition, major element contents, K/Rb ratios, and REE contents. XRD analyses and SEM showed the presence of discrete illite, the most dominant clay mineral, with smaller amounts of mixed-layer illite/smectite, chlorite, and kaolinite. The non-clay minerals found in the Woodford Shale from this study include quartz, dolomite, calcite, pyrite, feldspar (albite and microcline), and apatite. The clays in these rocks have a range of K/Rb ratios between 160 and 207. These ratios are considerably lower than the ratios of average silicate minerals (clays), with expected ratios between 250 and 350. It could be that clays received K and Rb from a solution, which was partly involved in oil generation by which oil received more K relative to Rb making the aqueous phase depleted in K/Rb ratios (Alvarez, 2015). Thus, the low K/Rb ratios for these clays may be reflecting signatures of reactions involving oil generation. The total REE contents ranged between 13 and 30 ppm. The low total REE contents of < 2 μm-size fraction clays in the Woodford Shale as compared to average sedimentary rocks which may be represented by values given either PAAS 184 ppm or NASC with 178 ppm, may suggest that the formation of the clays was linked to oil generation, having known of the face from the study of Alvarez (2015) that crude oils could have higher specific REE concentrations than the associated formation waters. PAAS-normalized REE patterns for these samples display positive Gd anomalies. Two out of the ten samples had prominent Ce anomalies. Only three out of ten samples had Eu positive anomalies, one of which was quite prominent. All samples had MREE enrichment, superimposed on either a flat REE distribution patterns with enrichment in LREE. Only one pattern showed the distribution

with a distinct HREE enrichment. The MREE anomalies could be from the effect of phosphate mineralization. In fact, the X-ray diffraction patterns of random powder samples showed the presence of fluorapatite and chlorapatite in most of the studied samples. The total organic carbon (TOC) contents of the whole rocks ranged from 0.5 to 6.54 wt.%. Thus, it can be concluded that hydrocarbon generation potential of the Woodford shale (0.8-4.44 wt.%) is significantly higher than Mississippian Lime unit (0.5 wt.%). Only one sample, which belonged to pre-Woodford Shale Hunton group, had the highest value of TOC. The available K-Ar dates of < 2 μm-size fraction clays suggest that the clays are authigenic (illites) for at least some samples. The dates ranged from 318.6 ± 7.9 Ma (Serpukhovian) to 353.9 ± 7.9 Ma (Tournaisian). All dates are younger than the times of deposition of the Woodford Shale. Assuming there is a genetic link between formation of authigenic illite and hydrocarbon generation, this study suggests that oil generation may have taken place on an average about 30 Ma after the deposition of the Woodford Shale.

Table of Contents

List of Figures

List of Tables

Acknowledgements

It is with immense gratitude that I acknowledge the help and support of my Professor and advisor, Dr. Sambhudas Chaudhuri. I would like to thank him for taking me as a graduate student and for providing advice and guidance, as well as patiently sharing his vast knowledge and experience with me from beginning to end. I would also like to extend my gratitude to my committee members, Dr. Abdelmoneam Raef, and Dr. Matthew W. Totten, for taking the time to contribute and participate in this research work. An immense thanks to Michael Cates, from the Diagnostic Medicine/Pathobiology department for allowing me the usage of the lab to perform the scanning electron microscopy (SEM) analyses. My sincere thank you to Amélie Aubert, for providing the X-ray diffraction analyses from the University of Strasbourg in Strasbourg, France. I appreciate the encouragement and moral support from my colleague, Dhaifallah Alsalem. Also, I would like to thank Dr. Ahmed Al-Aswad for his support and help. Lastly, I am indebted to my sponsor, King Abdulaziz City for Science and Technology, for providing me with grants to support this research as well as allowing me the opportunity to extend my academic knowledge in the United States.

Dedication

This work is dedicated to my family who has supported, encouraged and believed in me throughout my life. And to Mercedes, for her patience and understanding throughout this venture.

Chapter 1- Introduction

Oil and gas generation is a geological phenomenon that may occur over a period of time ranging from 5 to 10 million years to more than 100 million years (Tissot and Welte, 1984). Hydrocarbon generation has generally been thought to be a simple process in shale source rocks. Holding this view, Bordenave (1993) and several others (Tissot and Wellte, 1984) have mentioned that oil and gas are generated by gentle cooking of organic matter contained in organic-rich sediments in shale source rocks as they become progressively buried under increased geothermal heat that leads to thermal cracking of the sedimentary organic matter. However, this is only part of the history of oil and gas generation. A model has been suggested by Chaudhdri (personal communication), which is currently labeled as CTC model, after Chaudhuri, Totten, and Clauer, that gives a holistic view about the origin of petroleum. The model emphasizes nearly simultaneous interactions that take place among organic matter, minerals, water, gas, and energy, both geothermal heat and radiation energy, during the process of hydrocarbon liquid and gas generations in the shale source rocks. The configurations of interactions among these various parameters have yet to be resolved, although a holistic view seems to shed more light on the understanding of processes about oil and gas generations in the shale source beds than simplistic view of cracking organic matter under buried heat. The roles of minerals in hydrocarbon generation from kerogen in shale source beds remains uncertain. Currently, two views are held. Some hold the view that minerals may play no role, or at best a very small catalytic role in the hydrocarbon generation process (Huc et al., 1986; Monin and Audibert, 1988; Tissot and Welte, 1984). Surface area of particles has an important influence on reaction processes. Lewan, (1993), observing the results from hydrous pyrolysis experiments, noted that the size of the rock chips had no appreciable effect on hydrocarbon product yield, which seems to suggest that mineral matrices have an

insignificant role in hydrocarbon generation. Contrarily, a number of investigators have held a different view, maintaining that the minerals in shale source rocks play a significant role in the origin of petroleum hydrocarbons (Weiss, 1963; Hunt, 1979; Eisma and Jurg, 1967; Shimoyama and Johns, 1971; Almon and Johns, 1977; Espitalié et al., 1980). As the issue remains unresolved, further study of source rock materials is warranted in order to evaluate whether the composition of source rocks affect the process of hydrocarbon generation.

This study made an investigation on mineralogical and chemical compositions of Devonian-Mississippian the Woodford Shale in Oklahoma, which is well known for commercial productions of oil and gas. The purpose of this study was to determine whether mineral reactions, especially those involving clay minerals genetically linked to organic matter transformation into hydrocarbons. Besides mineralogical and chemical analyses, K-Ar isotope compositions of < 2 μm-size fraction clays in the Woodford Shale were determined to establish possibly the timing of hydrocarbon generation. Samples of well cuttings of the Woodford Shale from oil-producing fields in Payne and Pottawatomie Counties, Oklahoma were used for this study.

Stratigraphic, Structural, and Lithological Settings

The Woodford Shale of the middle Devonian to early Mississippian age is underlain unconformably by Silurian Hunton group (Figure 1), and is overlain by lower Mississippian Lime unit (Bebout et al., 1993; Henry and Hester, 1995; Johnson et al., 1989; Johnson and Cardott, 1992). The Woodford Shale, which is known as the major source rocks for hydrocarbon deposition in the Anadarko and Arkoma basins and also in the Cherokee Platform (Rascoe and Hyne, 1988; Wickstrom and Johnson, 2012), consists largely of fine-grained sediments with a high content of carbon and hydrogen (Ramirez-Caro, 2013). The thickness of the Woodford Shale in the study area ranged between 50 and 100 ft on the shallow shelf region in the northern of Oklahoma, and between 200 and 900 ft thick in the southern Oklahoma Aulacogen (Johnson and Cardott, 1992). The Woodford Shale is an organic-rich siliceous shale with varied amounts of interbedded carbonate and chert beds in association with phosphatic nodules (Andrews, 2009).

During the period between Late Devonian and the Early Mississippian, euxinic sea transgression occurred from south to southeast (Kirkland et al., 1992), resulting in the deposition of black organic rich sediments that included the Woodford Shale (Johnson et al., 1989).

During the late Mississippian to early Pennsylvanian, the Oklahoma region saw epeirogenic uplift and erosion, and followed by periods of orogenesis (Johnson and Cardott, 1992). These events produced the present-day display of depositional and tectonic provinces (Figure 2).

Based on geochemical parameters, geotechnical responses and well logs, the Woodford Shale has been subdivided into three members, Lower, Middle, and Upper (Cardott, 2009; Portas, 2009; Miceli, 2010; Slatt et al., 2013). The lower member contains interbedded black and gray siliceous fine grained rocks whereas the middle member is made up of black to gray fissile shale.

In many ways, the upper member is similar to the lower member. Both include cherty beds, with interbedded black to gray-siliceous shale, but the upper member is noted for presence of abundant included phosphate nodules (Ramirez-Caro, 2013). Most hydrocarbon production comes from the Meddle member. According to Comer and Hinch (1987), there are differences of the organic carbon content. Chert contains less than 0.1 wt.%, while black shale contains 35 wt.% organic carbon. Mostly, the organic matter is oil-prone type II kerogen (Comer and Hinch, 1987). Kerogen Type II commonly contains the remains of plankton (McCarthy et al., 2011).

The Woodford Shale is characterized as a good thermal maturity in shallow depth, and has high silica concentrations that create fractures when the well drills. Vitrinite reflectance information indicates that the Woodford Shale in Oklahoma ranged between <0.5% R_o, which is a low value of oil generation and >0.2% R_o implying high oil generation to dry gas generation (Comer and Hinch, 1987; Comer, 2008a).

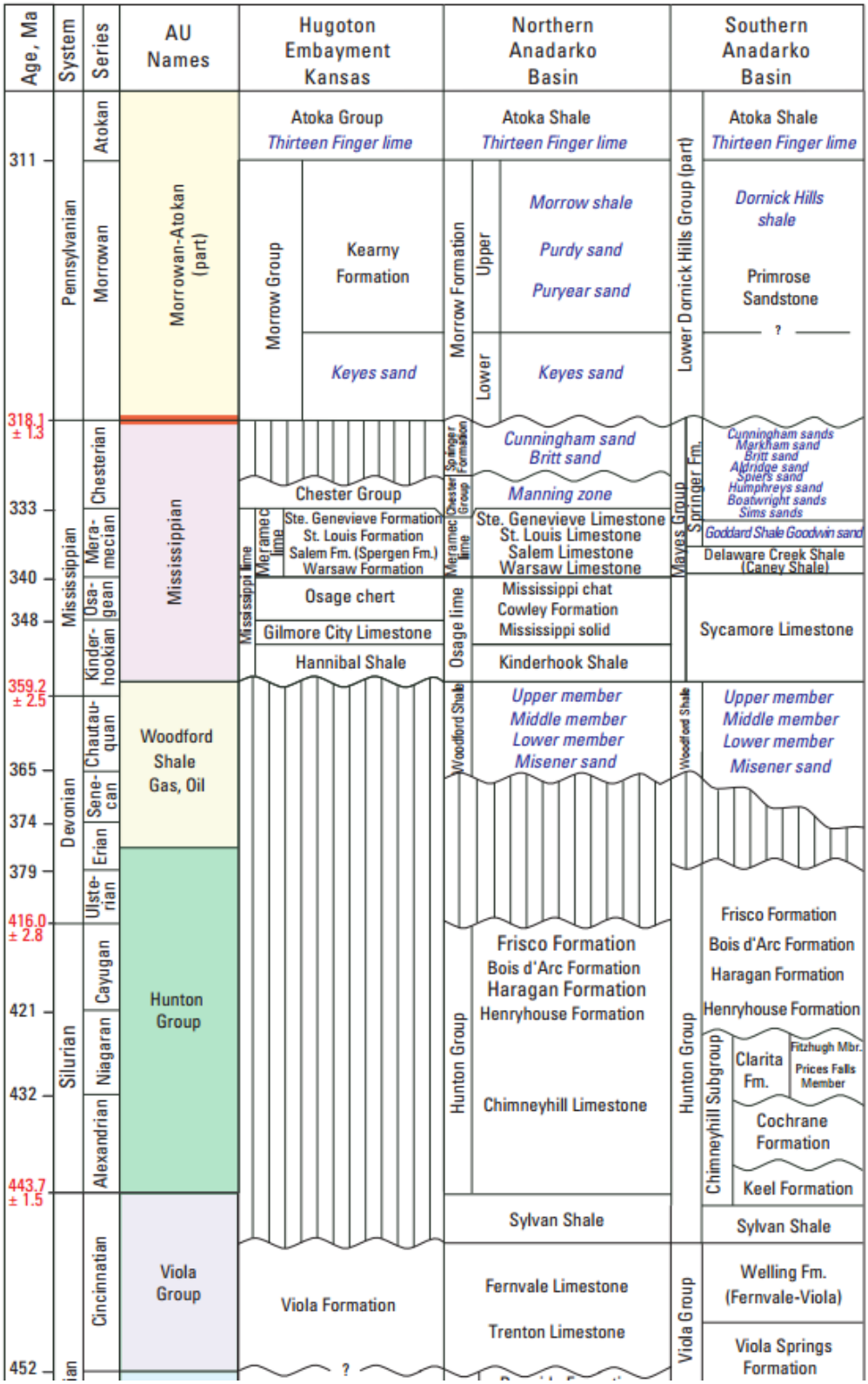

Figure 1: The stratigraphy of the Anadarko Basin, modified by Higley et al., (2014).

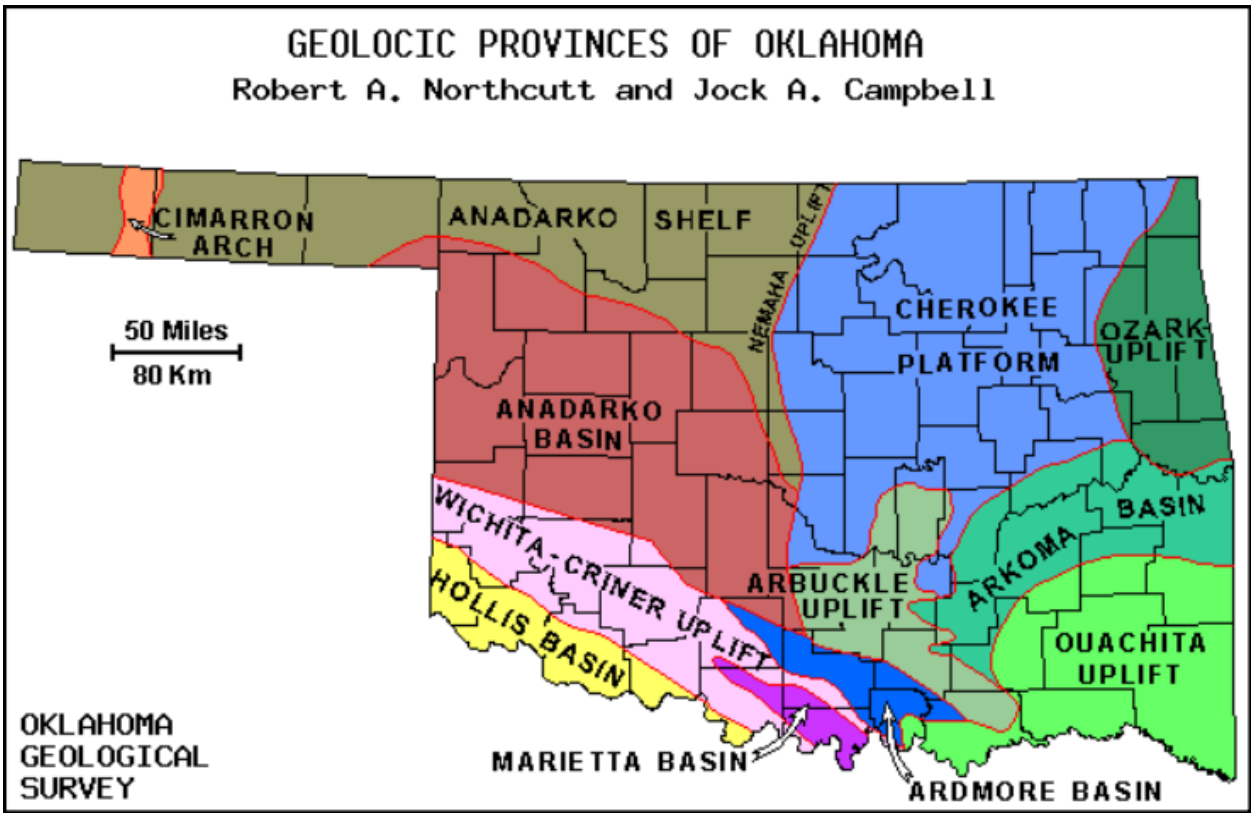

Figure 2:The present-day of geological basins of Oklahoma, modified by Northcuut and Campbell, (1995).

Chapter 2- Materials and Methods

The study area is located in the Cherokee Platform (Figure 2). Ten separate batches of shale rock cuttings, chosen randomly, were collected from Devonian-Mississippian oil-producing buried shale (Figure 3). These samples were selected to provide some range of horizontal and vertical covers for the study. Eight samples from the Woodford Shale and one sample from Hunton group which is below the Woodford Shale, and one sample from Mississippian Lime bed above the Woodford Shale. One of the Woodford shale samples came from Pottawatomi County, Oklahoma whereas the rest came from Payne County, Oklahoma (Table 3). Each collected sample was processed for separation of < 2 μm diameter fraction by a gravitative sedimentation method, following the settling parameter given in Folk (1968) for particle settlings in an aqueous medium. An aliquot of the slurry for each sample was used to make a glass slide coated with the clay derived from drying of slurry. This slide was then used for X-ray diffraction analyses of clay mineral composition of < 2 μm-size fraction sediments of the sample. The remaining slurry, after taking an aliquot to prepare the glass slide, was evaporated to dryness at room temperature to obtain a powdered sample of the < 2 μm-size clay fractions. The powder sample was then used to make chemical analysis for elemental contents, both major and trace element contents, to describe the chemical make-up of each sample and also to make analysis of K-Ar isotopes to obtain an isotopic age of the sample.

Table 1: Location of Samples and their depths.

Sample Name	Well Name	Section	Township	Range	County	Sample depth (ft)	Formation
SA-1	Spicer 1-36H	36	08N	03E	Pottawatomie Co, OK	6180-6200	The Woodford Shale
SA-2	Murlin 1-27H	27	18N	03E	Payne Co, OK	5960-5990	The Woodford Shale
SA-3	Murlin 1-27H	27	18N	03E	Payne Co, OK	6140-6170	The Woodford Shale
SA-4	Boyd 1-18WH	18	20N	02E	Payne Co, OK	5230-5240	The Woodford Shale
SA-5	Boyd 1-18WH	18	20N	02E	Payne Co, OK	6980-7000	The Woodford Shale
SA-6	State 1-15H	22	19N	03E	Payne Co, OK	7410-7440	Hunton group
SA-7	State 1-15H	22	19N	03E	Payne Co, OK	4010-4020	Mississippian Lime
SA-8	State 1-15H	22	19N	03E	Payne Co, OK	4860-4880	The Woodford Shale
SA-9	Stockton 1-34H	34	18N	03E	Payne Co, OK	7510-7540	The Woodford Shale
SA-10	Stockton 1-34H	34	18N	03E	Payne Co, OK	4980-5000	The Woodford Shale

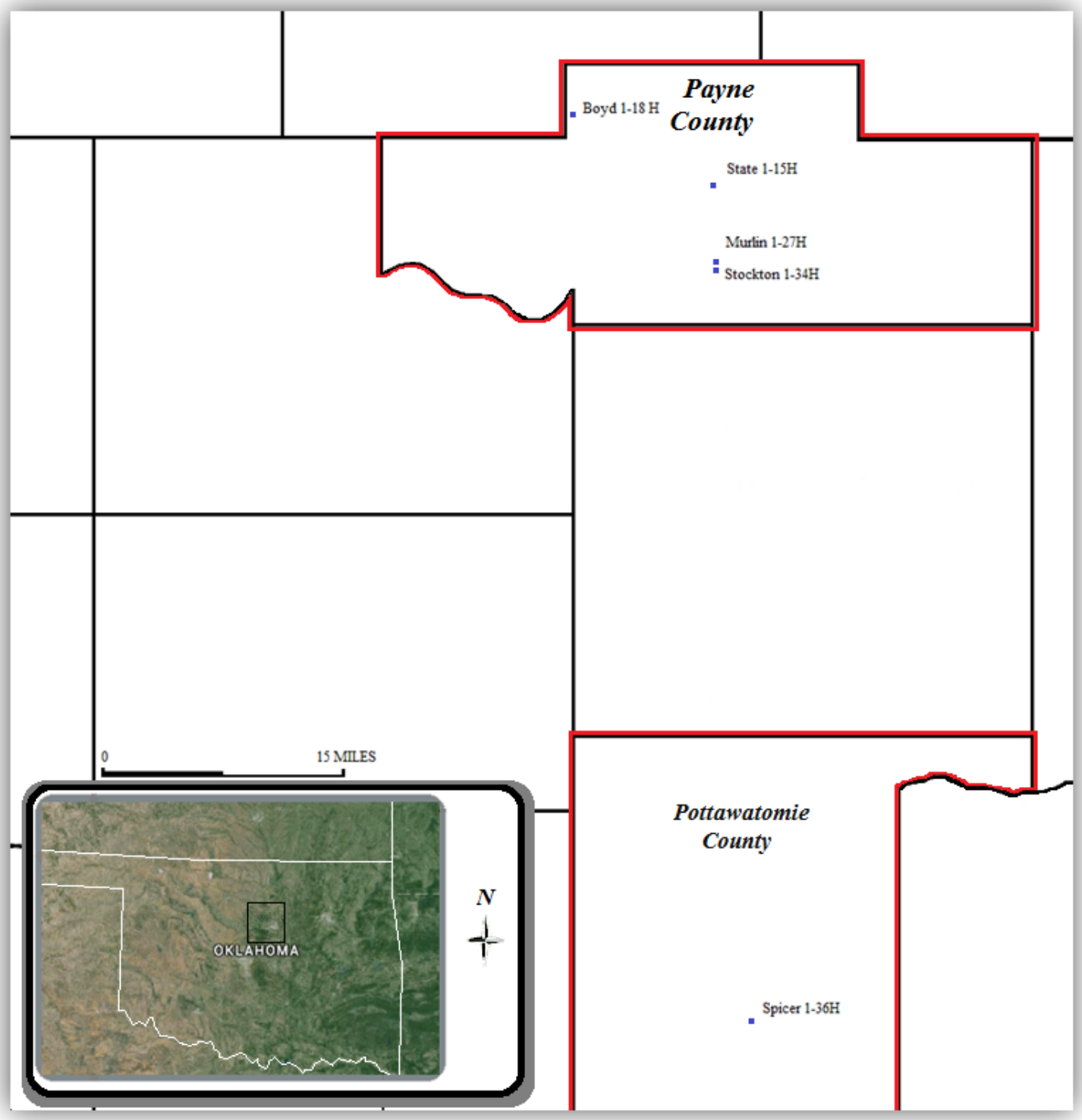

Figure 3: The samples' location and study area.

Mineralogical analyses

X-ray diffractions and scanning electron microscopy analyses

X-ray diffraction patterns for each < 2 μm-size clays were obtained from air-dried, ethylene glycol saturation, heating to 490 º C for one hour and a hydrazine treatment. A semi-quantitative (± 15%) estimation for each different clay sample was made, applying appropriate structural factors to the respective clay mineral reflections following collection of each sample.

Five whole rock samples were selected for their random powder X-ray diffraction to identify different minerals present in each sample. Random powder samples derived from < 2 μm-size fractions of the five samples were also investigated by X-ray diffraction for their mineralogical contents. X-ray diffraction analyses were carried out on each sample by on a Brüker D5000 diffractometer, using Cu-Kα radiation generated at 40kV / 30mA. Oriented samples were run with a scanning step of 0.02º / second and a 2 Θ seeking range between 3 and 30º for the air-dried and ethylene glycol saturated samples, and from 3 to 15º for heating and hydrazine treatments. For powder sample X-ray diffraction runs, a scanning sample rate of 0.02º / second was maintained with a scanning range between 3 and 65º. Random powders of < 2 μm-size were scanned slowly at a rate of 0.03º / 25 second for the 2 Θ range between 57 and 65º for finding the 060 reflections of the clay minerals (Moore and Reynolds, 1997). All X-ray diffraction analyses were made in the X-ray analytical lab at the University of Strasbourg in Strasbourg, France.

A semi-quantitative estimate of the samples was made for mineralogical compositions of each sample from comparisons with standard samples made up of clay minerals, quartz, calcite, apatite, feldspar and pyrite that were mixed in different proportions. Scanning electron microscopy SEM investigations of < 2 μm-size fractions were made, using the facilities available at Kansas State University, to help characterize morphologies of the clay particles.

Geochemical analyses

ICP-AES and ICP-MS

A known amount about 100 mg of each < 2 μm-size fraction clays was placed in a cap-fitting Teflon crucible, to which was added 15 ml of high purity of hydrofluoric acid, and about 3 ml of perchloric acid. The crucible was then put on a hot plate at 70-80 °C in a fume hood to digest the sample in the acid mixture for nearly 18 hours. The lid was then removed to let the remaining solution be evaporated to dryness. Following this dryness, about 5 ml of deionized water was added. This solution was evaporated again. The residue was dissolved in a small volume about 5 to 6 ml of mixture of highly purified nitric acid and highly purified hydrochloric acid (1:2). The solution then again was evaporated to dryness. The crucible was removed from the hot plate to let the evaporated mass cool to room temperature. Now the dried mass was dissolved in a known volume of highly purified 0.5 normal nitric acid. This is the final solution that was analyzed for major and trace element contents by ICP-AES and ICP-MS. These analyses were done at the University of Strasbourg in Strasbourg, France. All major chemical data have analytical accuracy within 2 to 5% at 95% confidence level and that within 5 to 10% accuracy at 95% confidence for trace or miner elements data, as reported by the chemical laboratory at the University of Strasbourg.

Determination of total organic carbon (TOC) and Rock-Eval Pyrolysis

Three Woodford Shale whole-rock samples, one Mississippian Lime whole-rock sample, and one Hunton group whole-rock sample were analyzed for total organic carbon and also for Rock-Eval pyrolysis. The total organic carbon and Rock-Eval analyses were performed by GeoMark Laboratory in Humble, Texas.

The K-Ar isotopic data

Five sample of < 2 μm-size fraction clays were analyzed for their K-Ar dates. K-Ar analyses were done by the Commonwealth Scientific and Industrial Research Organisation (CSIRO), in Australia, using techniques that were similar to that Dalrymple and Lanphere (1969), Bonhomme et al (1975) and Steiger and Jäger (1977).

Chapter 3 – Results

Mineralogical analyses

Oriented samples of < 2 μm-size fraction clays

The X-ray diffraction analyses of the < 2 μm-size fraction clays revealed that they consisted of discrete illite, the most dominant clay mineral, with smaller amounts of mixed-layer illite/smectite (about 90-95% of which was illite), chlorite and kaolinite (Figure 4).

X-ray diffraction patterns of < 2 μm-size fraction clays (oriented slides) illustrated discrete illite as a very sharp (well crystalline) and asymmetry on (001) peak at 9.99 Å. Moreover, a mixed-layer illite/smectite was found in a few samples, glycolated peak a slight tail near 10.4 Å. On the reflection of heating condition showed two peaks at 9.98 Å and the other at 10.41 Å. The 9.98 Å reflection may reflect of distinct illite, and 10.48 Å reflection could be other type of mixed-layer clays of illite-smectite composition, but highly dominated by illite, possibly smectite with hydroxyl interlayer.

Table 2: The clays < 2µm-size fraction.

Sample	% Clay Minerals
SA-1	84.8
SA-2	88.05
SA-3	89.21
SA-4	83.44
SA-5	82.45
SA-6	90.3
SA-7	85.43
SA-8	63.48
SA-9	90.36
SA-10	61.5

Figure (5) illustrates the X-ray diffraction pattern of sample SA-8, which is a typical representative of all other samples. X-ray diffraction (XRD) patterns for other samples can be found in Appendix A.

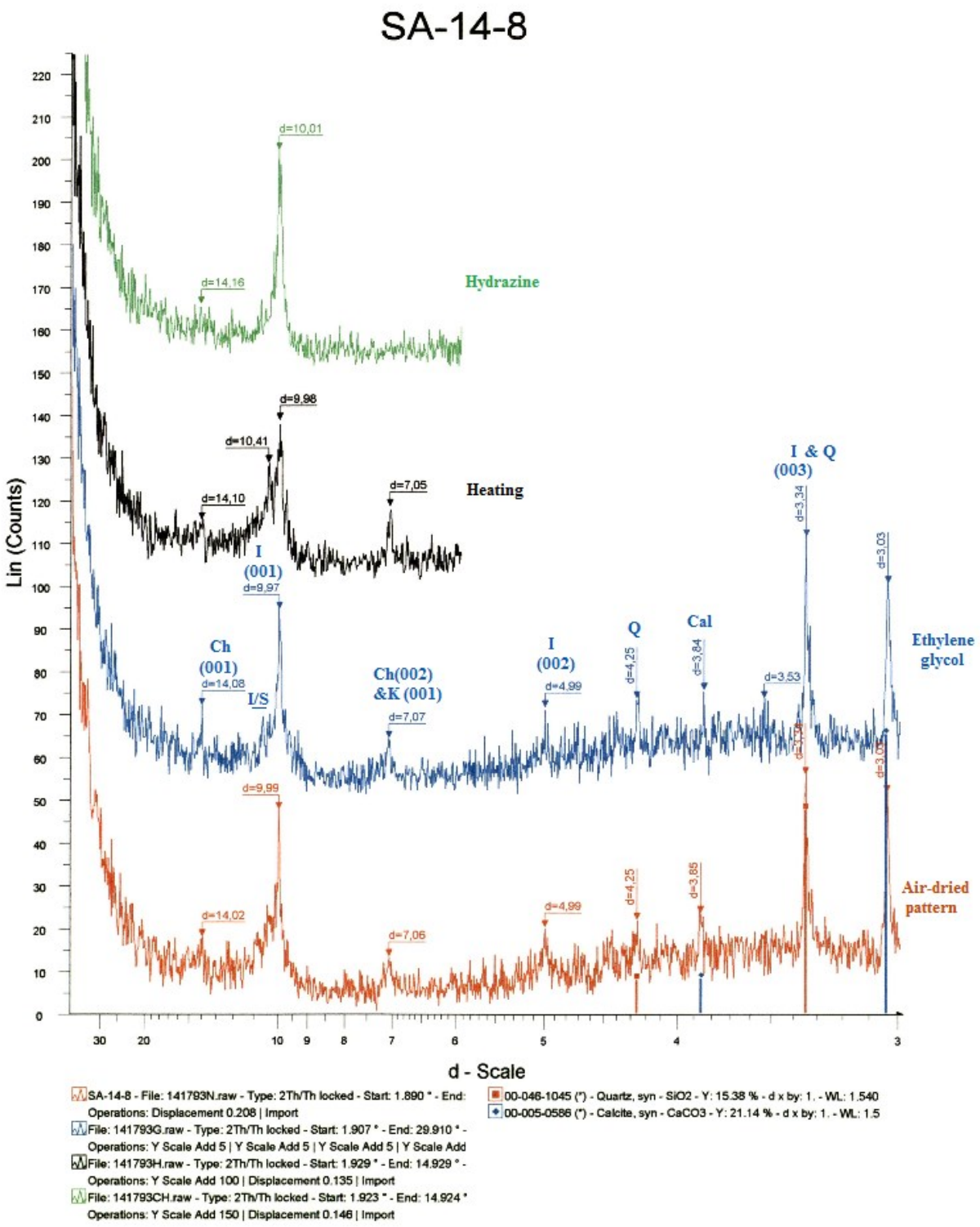

Figure 4: XRD patterns of the oriented sample underwent four treatments. Ch: chlorite, I: illite, I/S: mixed-layer illite/smectite, K: kaolinite, Q: quartz and Cal: calcite.

X-ray diffraction random powder of < 2 µm-size fraction clays (slow record)

Powder diffraction diagrams of the clay samples provided information about the dioctahedral-trioctahedral characteristics of the clays. The presence of 1.50 Å peaks, which characterized the d_{060}-spacing of the clays, suggested that the illite clay minerals were primarily dioctahedral in composition (Figure 5).

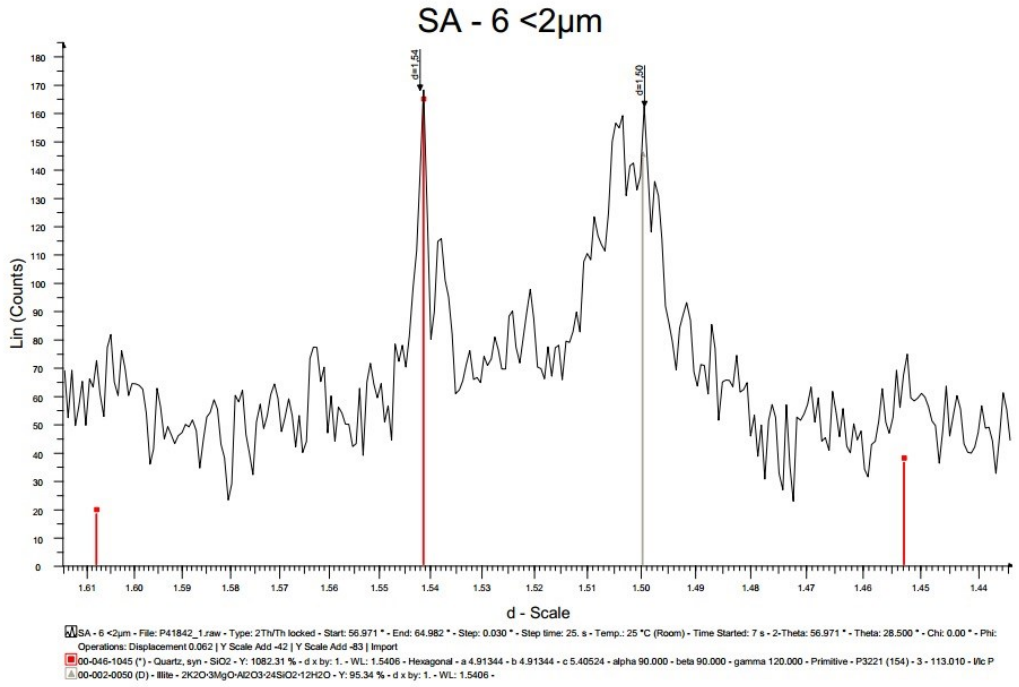

Figure 5: The reflection pattern of disoriented sample illustrates the reflection of d(060) plane.

SEM investigations

SEM diagrams provide a good view of morphology of clay minerals and their distinctive textures. All samples illustrated the presence of discrete illites. Based on scanning electron microscopy images, it was observed that illite showed different distinctive morphologic features and texture. In general, it illustrated common types of illite that are curled at the edges and platy

shape that trend to be laminated, which is similar to the description of illite provided by Keller et al., (1986). The morphology of mixed-layer illite/smectite (I/S) was difficult to observe because there was a small amount of mixed-layer illite/smectite in the samples, compared to the proportion of illite. Only figure of SA-8 sample illustrated the presence of mixed-layer illite/smectite as flat-lying plate and the edges (Figure 6). Kaolinite was also noted in the image of SA-8 sample. SEM micrograph of sample illustrated the presence of kaolinite as a shape pseudo-hexagonal plate with smooth plane (Figure 7). The SEM photomicrographs of other samples are located in Appendix E.

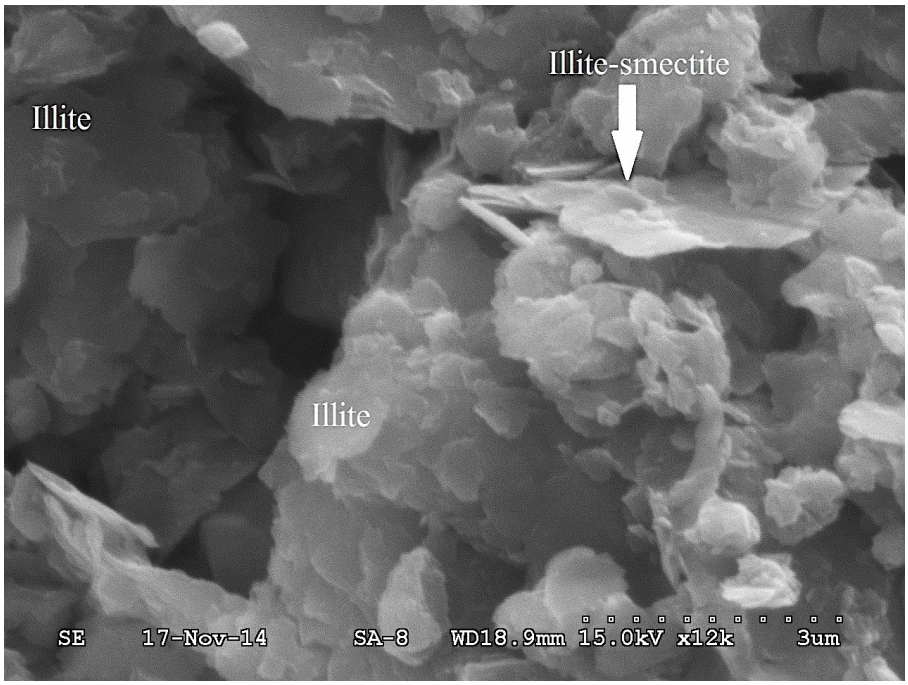

Figure 6: Platy-shaped illite and mixed-layer I/S as flat-lying plate with edge (SA-8).

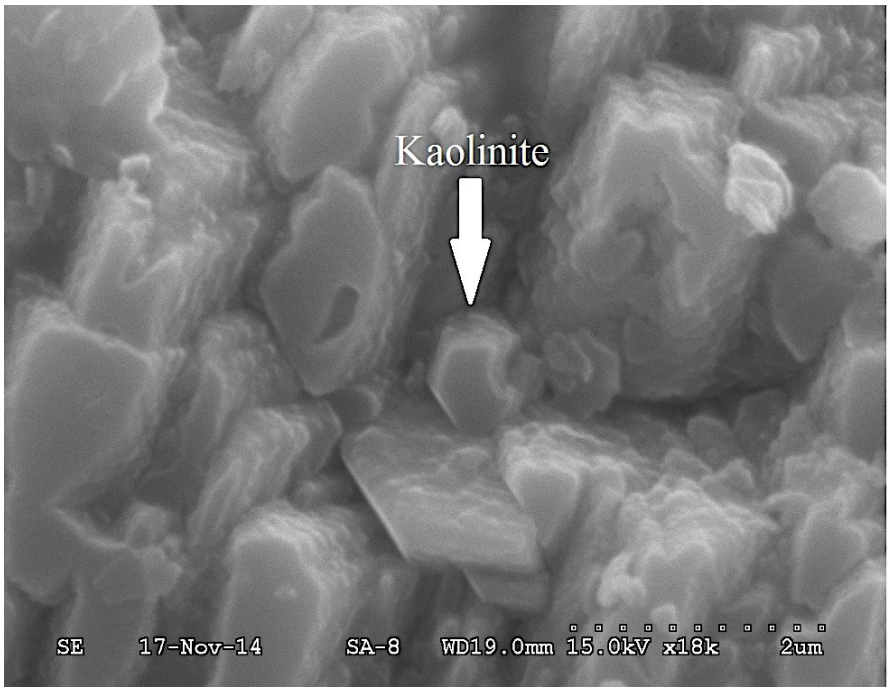

Figure 7: Kaolinite, pseudo-hexagonal shaped at low magnification.

X-ray diffraction of random powder whole-rock

Powder sample with random orientations provide a good illustration of the presence of non-clay minerals (Figure 8). Quartz has been found to be the dominant mineral in all the Woodford shale samples. Quartz ranged from 43 to 76 %. Less abundant mineral is calcite. The average content of calcite is 19 %, ranging from 2 to 42 %. SA-8 and SA-10 samples have the highest percentages of calcite. Dolomite was another common mineral, which could be found in nearly all samples, ranging from 5 to 14 %. Pyrite, feldspar (albite and microcline), fluorapatite and chlorapatite were also found in these samples, but they were in smaller amount. Pyrite constituted about 4 to 7 %, Feldspar about 3.5 to 7.5 %, and apatite about 2 to 7 %.

Table 3: The percentages of minerals in random powder whole-rock (as shown in XRD measurement).

Minerals	SA-5	SA-6	SA-7	SA-8	SA-10
Illite	4.18	3.74	2.22	3.06	3.63
Chlorite	2.90	4.62	1.94	3.74	2.47
kaolinite	-	-	2.23	2.87	1.43
Quartz	66.67	76.20	68.77	69.26	43.65
Dolomite	14.37	7.56	-	7.08	5.54
Calcite	4.3	9.17	2.31	39.02	42.56
Pyrite	7.31	6.35	-	3.92	3.88
Albite	5.87	7.40	5.66	4.36	4.93
Microcline	3.48	-	-	-	-
Fluorapatite	-	6.79	2.22	4.45	-
Chlorapatite	-	-	-	-	3.66

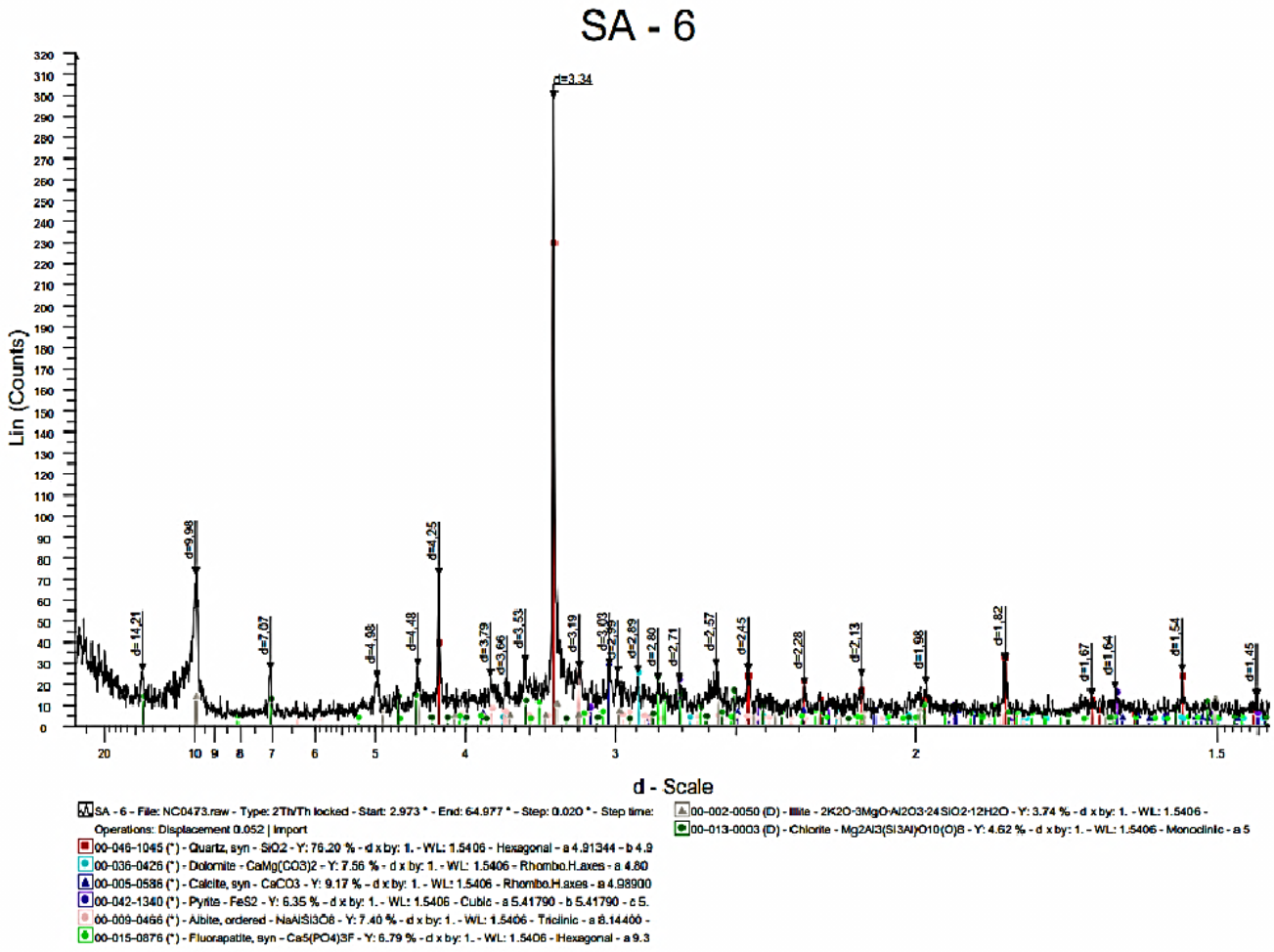

Figure 8: X-ray diffraction of random powder whole-rock.

X-ray diffraction of random powder < 2µm-size fraction clays

Quartz ranged from 52 to 93 %. Calcite ranged from 14 to 23 %. Only two samples (SA-5 and SA-10) indicated the presence of dolomite, the contents of which ranged between 5 and 9 %. Other minerals were found in some samples e.g. pyrite, albite, microcline, fluorapatite and chlorapatite (Figure 9 and Table 4).

Table 4: The percentages of minerals in random powder of fraction clays < 2 µm.

Minerals	SA-5	SA-6	SA-7	SA-8	SA-10
Illite	20.48	13.45	11.39	11.80	4.27
Chlorite	10.71	12.46	12.00	10.29	4.28
Kaolinite	-	-	28.60	12.01	6.51
Quartz	52.19	85.59	93.07	84.05	55.42
Calcite	14.62	15.46	22.97	-	-
Dolomite	9.65	-	-	-	5.89
Pyrite	10.64	18.55	-	15.20	5.20
Albite	11.82	19.95	26.48	17.86	7.99
Microcline	14.78	-	-	-	-
Fluorapatite	-	18.30	19.50	-	-
Chlorapatite	-	-	-	-	5.54

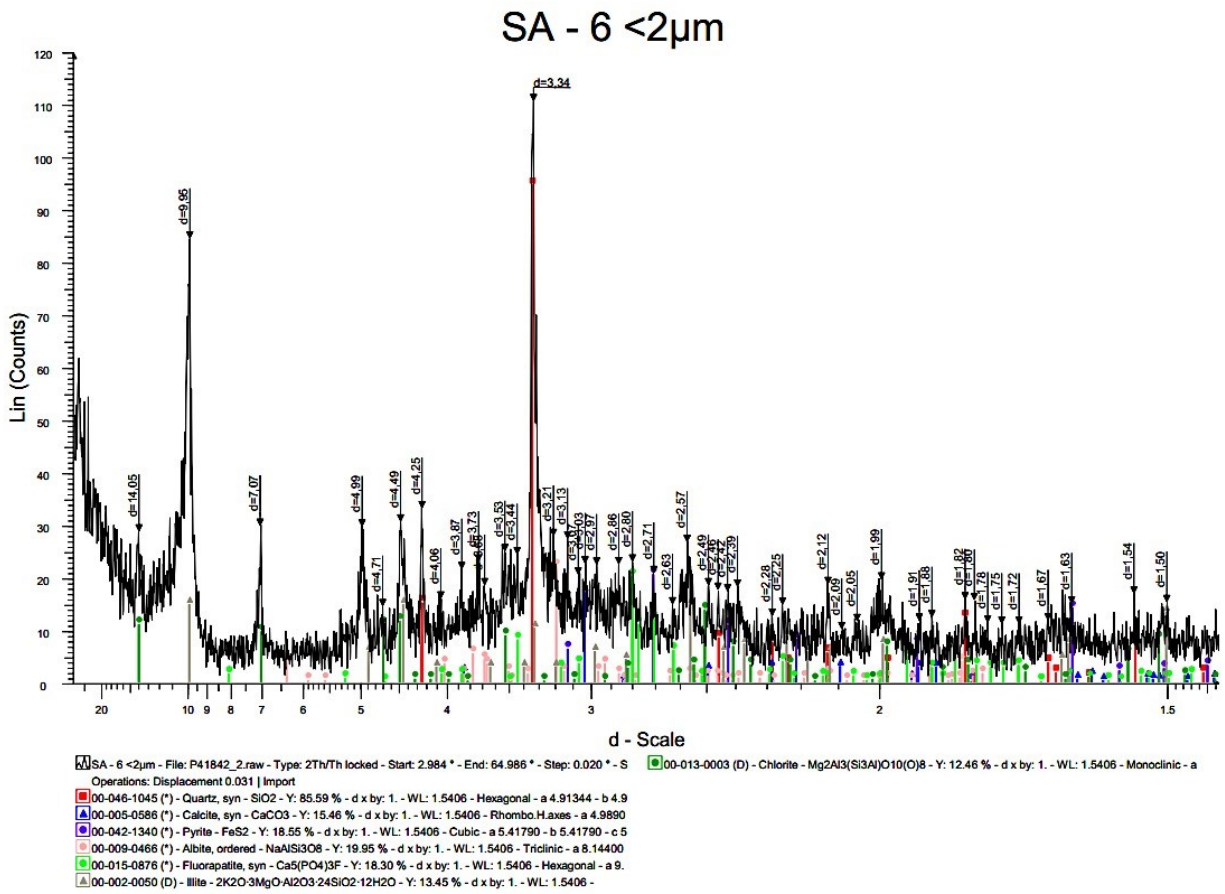

Figure 9: XRD of random powder < 2µm fraction clays.

Chemical Data of < 2 µm-size fraction clays

Major element and trace element data are presented in table 5 and 6.

Table 5: Major element contents (ppm), in < 2 µm-size fraction clays.

Samples	Al	Mg	Ca	Fe	Mn	Ti	Na	K	P
SA-1	8960	1168	2096	3056	15.68	340.8	320	2400	64
SA-2	9680	1632	1824	3408	18.88	356.8	400	3520	38.4
SA-3	10480	1816	1104	3448	17.6	395.2	320	3840	36.8
SA-4	9840	2056	2080	4072	27.04	395.2	400	3520	102.4
SA-5	13440	2320	1088	4488	29.6	412.8	400	4960	59.2
SA-6	11680	1840	960	4208	20.16	347.2	320	4160	134.4
SA-7	15680	1920	1888	8240	92	652.8	560	3680	131.2
SA-8	5880	1680	14960	2336	27.36	241.6	320	1840	432
SA-9	9600	1784	1120	3360	18.24	347.2	400	3760	38.4
SA-10	6208	1536	22080	2312	28.32	305.6	400	1920	206.4

Table 6: Trace elements content (ppm) for < 2 µm fraction clays.

Element	SA-1	SA-2	SA-3	SA-4	SA-5	SA-6	SA-7	SA-8	SA-9	SA-10	*PAAS
Cr	11.84	13.44	14.4	14.72	17.6	16.8	18.56	16.16	12.48	13.12	
Co	4.272	3.712	3.328	7.472	3.104	1.68	3.904	0.8	3.008	1.728	
Ni	16.96	14.24	12.56	16.8	12.32	14.48	8.32	7.408	11.92	5.856	
Cu	1.6	1.52	1.896	2.248	2.104	3.264	2.144	1.96	1.8	0.64	
Zn	87.2	96	43.6	56.4	54.4	39.04	26.64	20.72	39.36	69.12	
Rb	15.04	20.48	23.2	20.32	28.64	25.44	21.92	11.36	20.48	9.28	
Sr	11.2	8.96	9.6	9.84	9.68	9.76	27.36	25.6	9.04	33.92	
Y	1.712	2.032	2.16	3.072	2.96	4.048	2.768	4.384	1.936	2.688	
Zr	6.304	7.648	8.16	8.16	8.8	7.744	9.12	3.52	7.856	3.744	
Cd	0.033	0.0591	0.043	0.106	0.043	0.108	0.134	0.019	0.046	0.0308	
Cs	0.888	1.352	1.576	1.232	1.544	1.76	1.128	0.6712	1.384	0.5272	
Ba	32.8	31.36	34.88	39.36	54.56	40.16	65.44	28	46.88	30.88	
La	2.848	3.168	3.44	4.032	3.472	3.2	5.952	3.968	3.04	2.896	38.2
Ce	6.496	5.776	6.304	11.36	7.12	5.888	12.72	4.784	5.616	5.12	79.6
Pr	0.632	0.683	0.737	0.912	0.808	0.753	1.448	0.904	0.662	0.631	8.83
Nd	2.448	2.688	2.848	3.68	3.184	3.072	5.856	3.824	2.608	2.592	33.9
Sm	0.433	0.493	0.521	0.6992	0.585	0.588	1.168	0.731	0.475	0.485	5.55
Eu	0.088	0.104	0.109	0.156	0.183	0.12	0.248	0.155	0.1	0.105	1.08
Gd	0.404	0.469	0.496	0.68	0.544	0.536	1.04	0.776	0.452	0.514	4.66
Tb	0.055	0.063	0.068	0.092	0.067	0.074	0.129	0.103	0.062	0.0698	0.774
Dy	0.32	0.375	0.396	0.52	0.397	0.436	0.661	0.607	0.364	0.402	4.68
Ho	0.064	0.0746	0.0799	0.101	0.08	0.0896	0.1192	0.122	0.0724	0.0796	0.991
Er	0.204	0.232	0.254	0.314	0.252	0.292	0.351	0.36	0.228	0.239	2.85
Tm	0.0292	0.034	0.036	0.043	0.035	0.042	0.047	0.045	0.0324	0.0306	0.405
Yb	0.202	0.232	0.244	0.279	0.2408	0.292	0.318	0.284	0.224	0.194	2.82
Lu	0.059	0.036	0.038	0.042	0.036	0.044	0.046	0.042	0.034	0.028	0.433
Pb	3.528	2.544	1.912	2.872	2.312	3.456	4.64	1.096	1.92	2.632	
Th	0.824	0.784	0.872	1.072	1.208	1.08	1.808	0.712	0.888	0.624	
U	4.16	6.992	6.672	5.36	3.312	3.648	0.528	1.12	6.592	1.568	
K/Rb	159.58	171.88	165.52	173.22	173.19	163.53	167.89	161.98	183.59	206.89	
U/Th	5.05	8.92	7.66	5	2.75	3.55	0.29	1.58	7.43	2.52	
Ce/Ce*	0.082	0.073	0.079	0.143	0.089	0.074	0.16	0.061	0.071	0.065	
Eu/Eu*	0.082	0.096	.01	0.144	0.168	0.112	0.229	0.143	0.093	0.098	
∑REE	14.28	14.43	15.57	22.906	17.005	15.43	30.102	16.7005	13.97	13.39	184.773

(*PAAS as reference for REE).

K/Rb ratios

The K/Rb ratios of the clay fractions ranged from about 160 to 207. The K/Rb rations of the clay fractions are shown in a histogram (Figure 10). A comparison with the K/Rb ratios of common crustal silicate rocks and modern plant values is also shown in this figure (Chaudhuri et al., 2007).

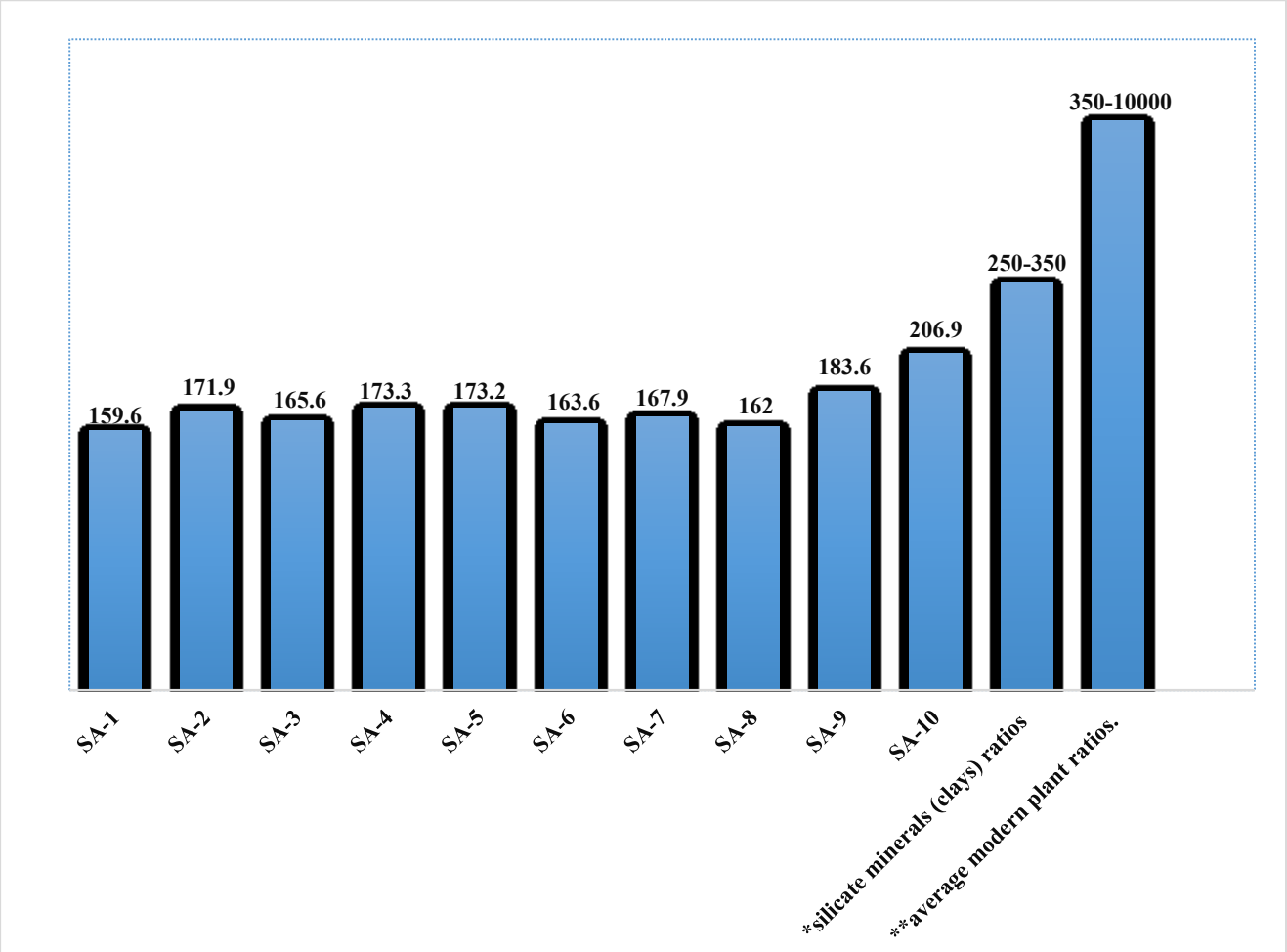

Figure 10: K/Rb ratios of less than 2 µm fraction clays with average of *silicate minerals (clays) ratios and **average modern plant ratios.

U/Th ratios

Uranium contents ranged from 0.5 to 7 ppm, whereas thorium contents ranged from 0.6 to 1.2 ppm. U/Th ratios ranged between 0.2 and 9. Only one had a low ratio of about 0.3 (SA-7), but all others had values higher than 1.5. Among the samples with high ratio values, five of them had values between 5 and 9. Although the U concentrations are not as high as in black shales, whose concentrations usually range between 20 ppm- 250 ppm (Swanson, 1961; Lewan and Buchardt, 1989), the U/Th ratios are higher than average shale and crustal rocks (Figure 11).

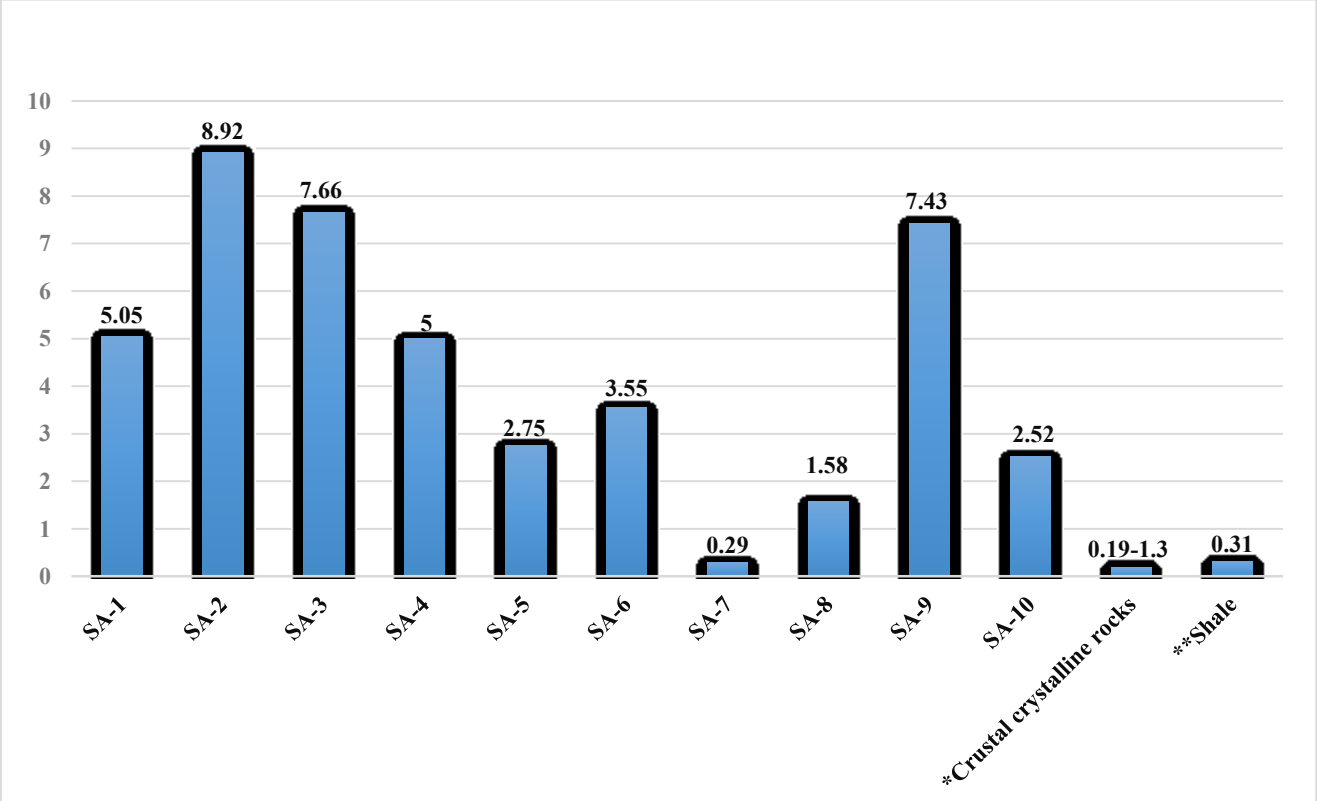

Figure 11: U/Th ratios.

Rare Earth Elements

The total REE concentrations ranged between 13 and 30 ppm. The total REE concentrations of < 2 µm fraction clays are illustrated in Figure 12. Less than 2 µm fraction clays are significantly lower than the concentration of an average shale such as Post-Archean Australian Shale PAAS with 184 ppm (Taylor and McLennan, 1985) and North American Shale Composite NASC with 178 ppm (Goldstein and Jacobsen, 1988).

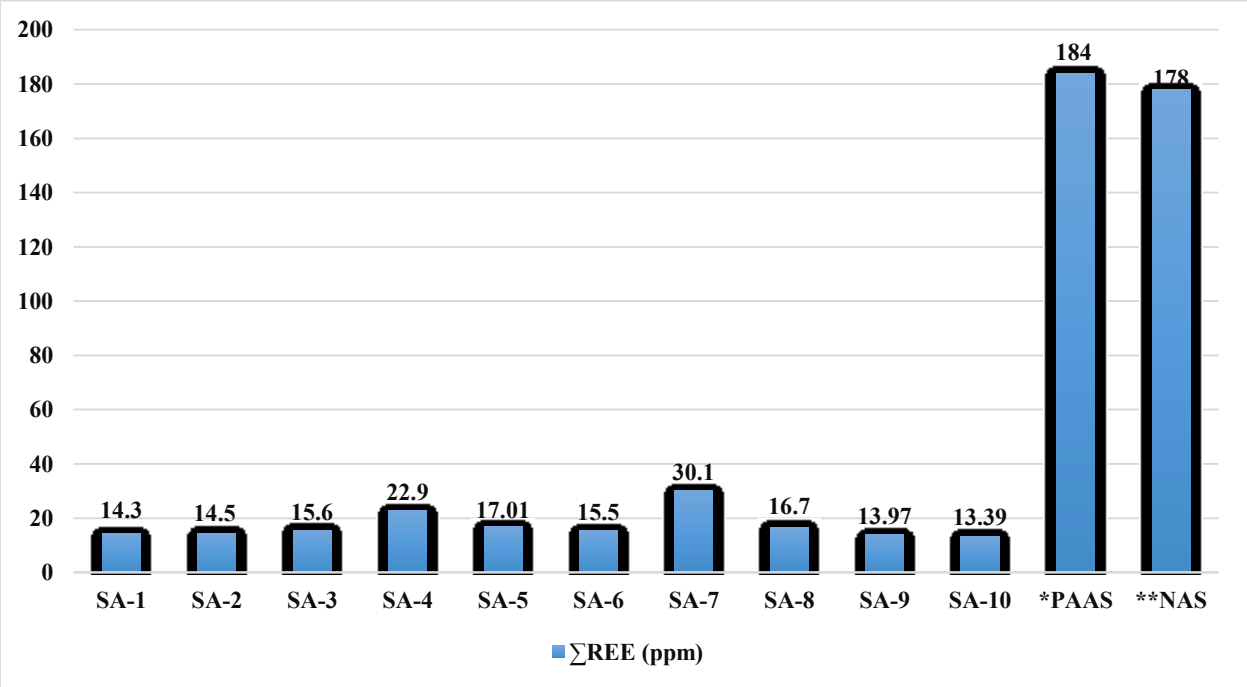

Figure 12: REE concentrations (ppm).

REE distribution patterns of < 2 µm clay fractions

It well known that an understanding of the distribution pattern of the REEs in samples of a rock has the potential to reveal significant amount of information about the geochemical history of the rock. The REE distribution pattern of a sample is generally shown by displaying the trend seen from a diagram wherein the concentration of given REE element is divided by the concentration of the same element of a reference sample to get a ratio, which then plotted against

the atomic number of the REE in a sequence of increasing atomic number. The study has chosen to use to PAAS as the reference sample.

By customary practice, La, Ce, Pr, Nd, Sm, and Eu collectively make up the light rare earth element (LREE) group. Because Sm and Eu are also part of Middle rare earth element (MREE) group, it may convenient to consider only La, Ce, Pr, Nd to define LREE distribution trend, which will be particularly necessary in the event of either a prominent MREE enrichment or prominent MREE depletion. Based on the situation with the present study, wherein prominent MREE enrichment exists the LREE distribution trend, defined by La to Nd, is just about flat for nearly all but two samples (SA-7 and SA-8) that are apparently with a slight LREE depletion trend. Two samples had prominent Ce anomalies, one (SA4) with a positive Ce anomaly and the other (SA-8) with the prominent negative Ce anomaly (Figure 13 and 14).

The MREEs include Sm, Eu, Gd, Tb, Dy, and Ho. All samples were found to be with MREE enrichments by varied amounts. A repeated feature that associated with the MREE enrichment was Gd positive anomalies (Figure 15). One sample (SA-5) was found to be with a prominent Eu positive anomaly. Samples (SA-4 and SA-7) also appeared to be with slight Eu positive anomalies (Figure 16).

The HREEs include Gd, Tb, Dy, Ho, Er, Tm, Yb, and Lu. Four (SA-4, SA-7, SA-8, and SA-10) out of ten samples displayed slightly depleted HREE distribution patterns (Figure 17), whereas one (SA-6) could be with a slight HREE enrichment (Figure 18). HREE distribution

patterns of the remaining samples were flat. A several of them appeared to be with slight Ho negative anomalies.

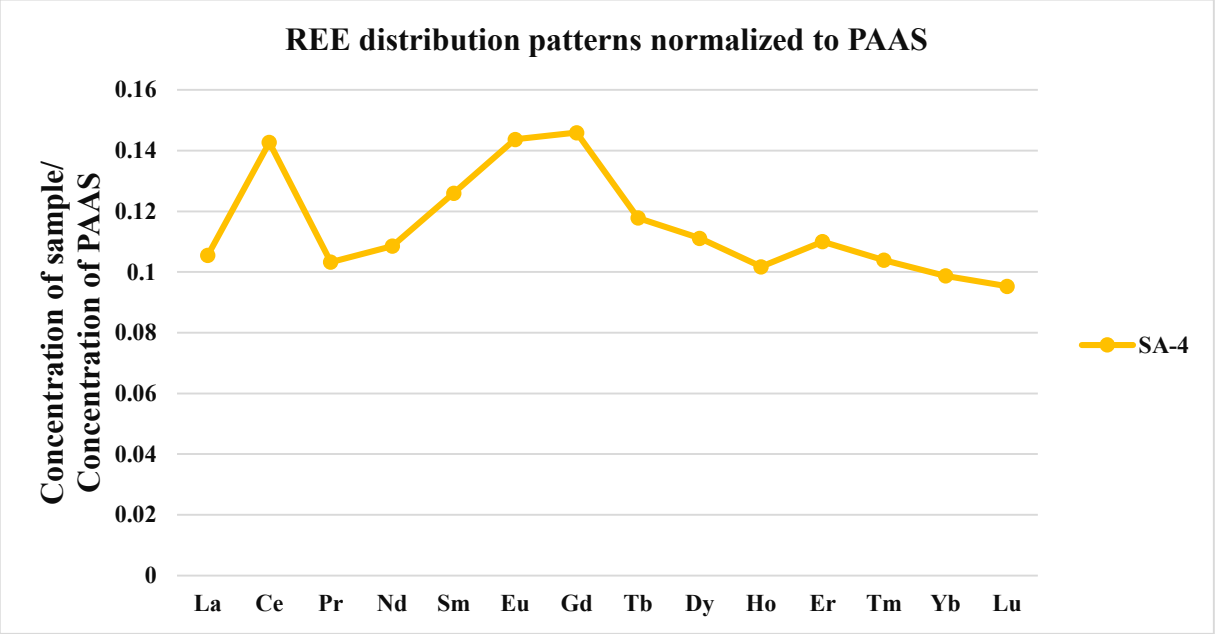

Figure 13: Positive Ce anomaly.

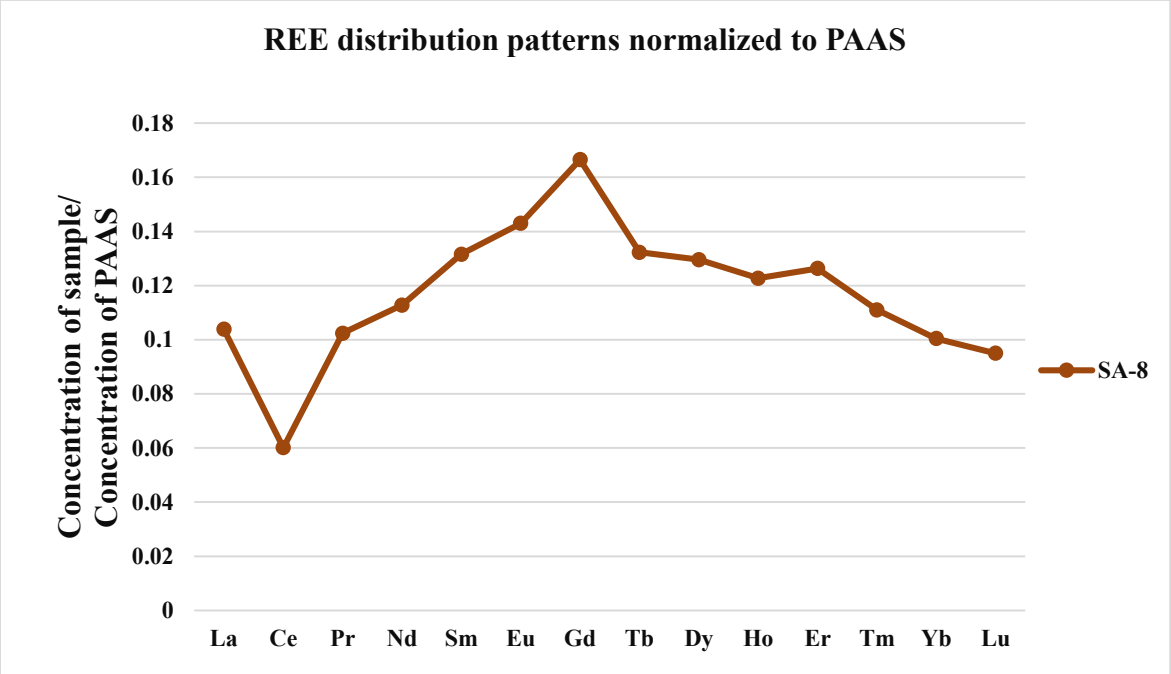

Figure 14: Negative Ce anomaly.

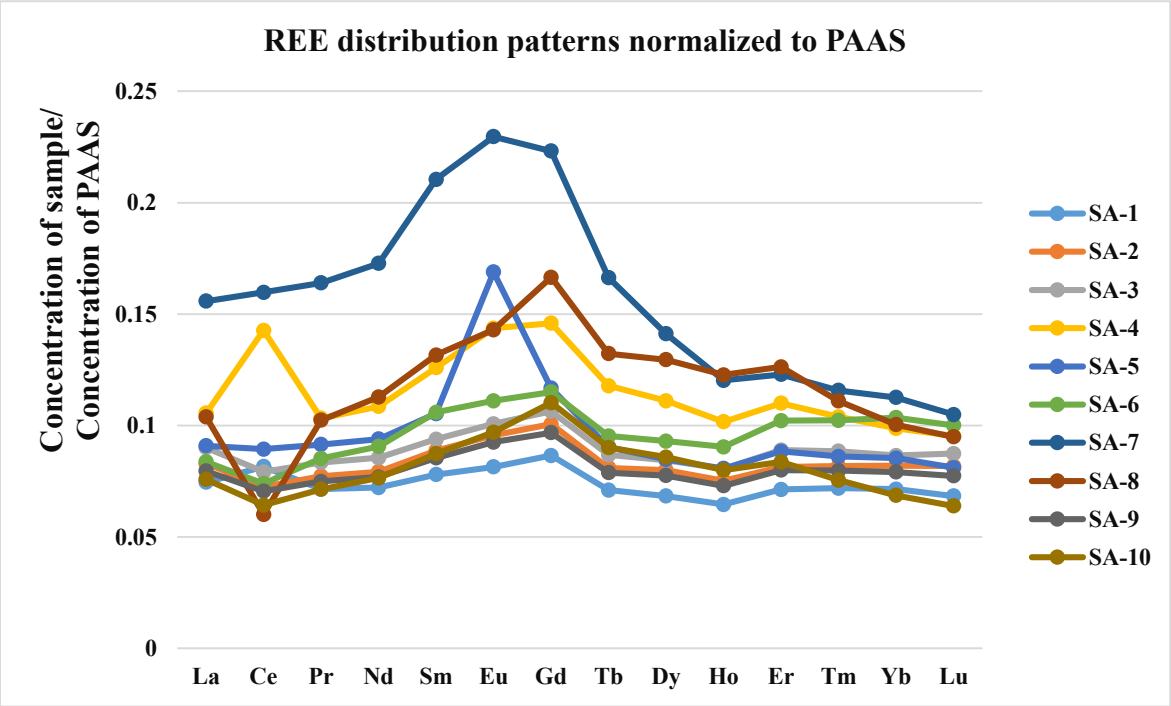

Figure 15: MREE enrichment and positive Gd anomalies.

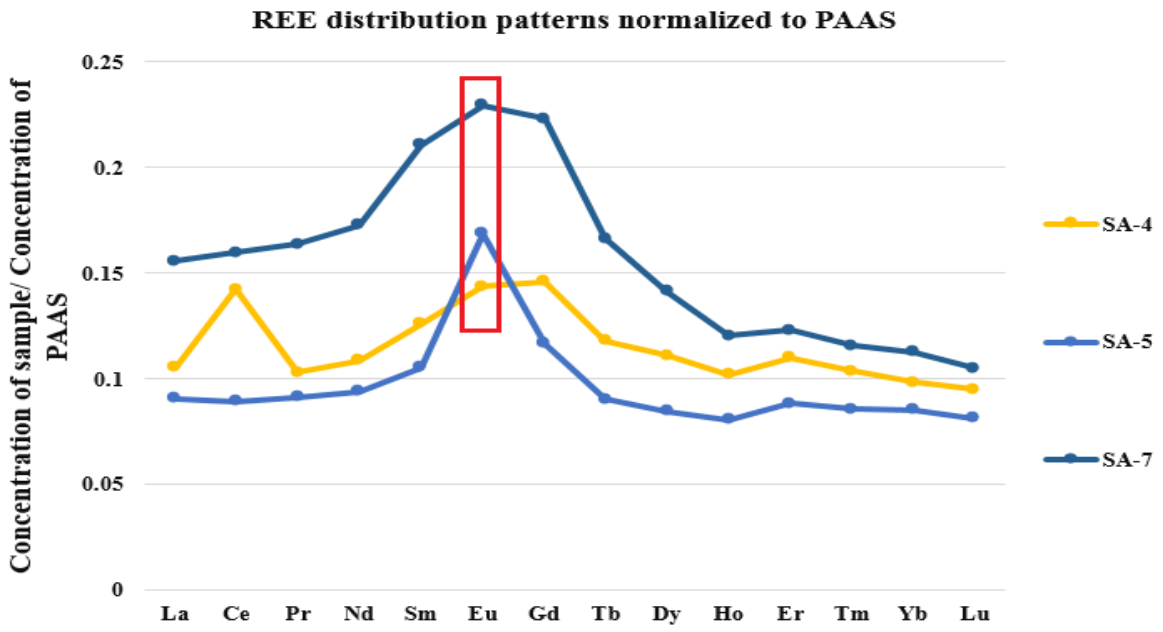

Figure 16: Positive Eu anomalies.

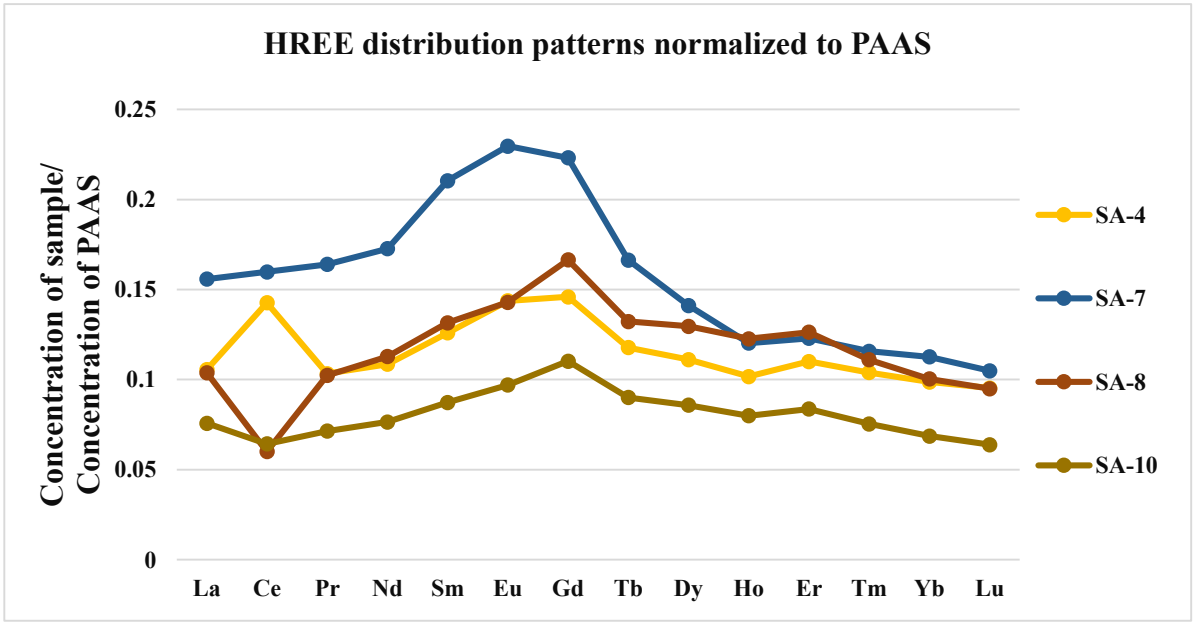

Figure 17: Four samples displayed slightly depleted HREE distribution patterns.

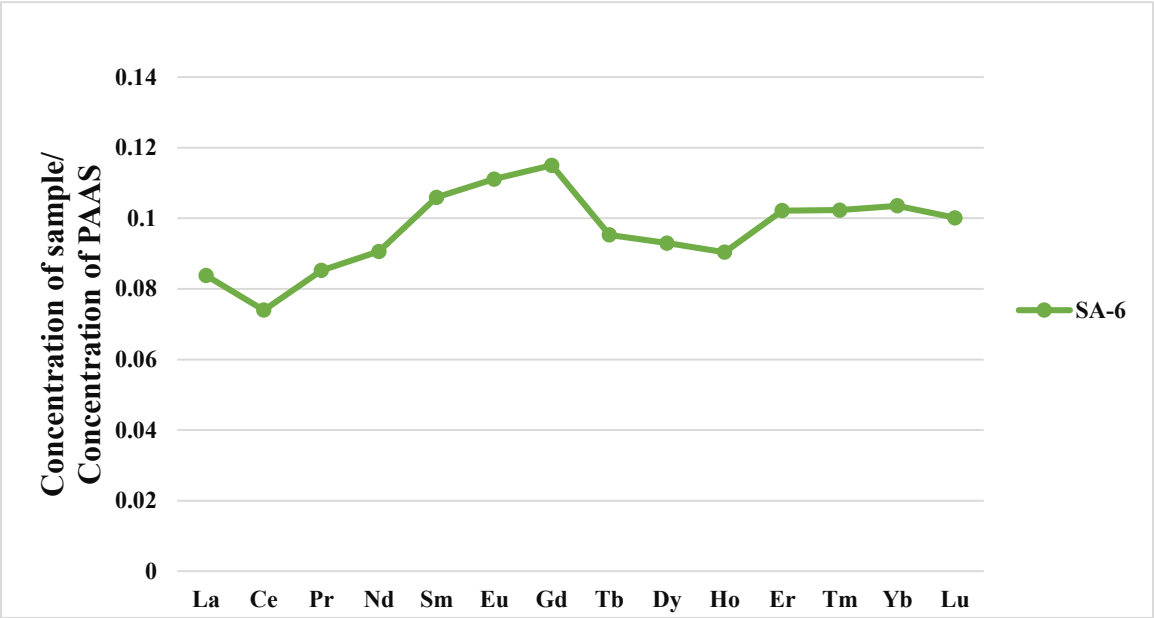

Figure 18: HREE enrichment.

Organic Geochemical Data

The organic richness of the samples was assessed by analyzing the total organic carbon (TOC) contents of the shale samples. The whole rock samples from the Woodford Shale showed a range of TOC values between 0.81 and 4.44 wt.%, with one sample, which belonged to the Mississippian Lime unit had low value of 0.5 wt.% (Table 7). One sample of Hunton group had 6.54 wt.%, which is the highest sample of TOC. To find out the thermal maturity of the samples and the kerogen type, Hydrogen Index (HI), Oxygen Index (OI) and T_{max} were determined as well (Figure 18). As cited by Ugochukwu (2010), parameters of pyrolysis are S_1, S_2, S_3 and T_{max}, where S_1 is the amount of free gas and oil in the sample (mg of HC/ g of rock), S_2 is the amount of hydrocarbons generated through thermal cracking of non-volatile organic matter, S_3 is the amount of CO_2 (mg CO_2/ g of rock), and T_{max} is the maximum temperature to release hydrocarbons (top of S_2 peak) from cracking of kerogen that occurs during pyrolysis (Wapples, 1985**)**. The hydrogen Index is given as,

$$\mathrm{HI} = \frac{\mathrm{S2} \times 100}{\mathrm{TOC}}$$

The oxygen index is given as,

$$\mathrm{OI} = \frac{\mathrm{S3} \times 100}{\mathrm{TOC}}$$

Table 7: The TOC and Rock-Eval results.

Sample ID	Depth (ft)	Percent Carbonate (wt. %)	Leco TOC (wt. %)	Rock-eval-2 S1 mg HC/g	Rock-eval-2 S2 mg HC/g	Rock-eval-2 S3 mg HC/g	Rock-eval-2 (°C)	Calculated %Ro (RE	* HI	** OI	S2/S3 ConcMg HC/mg CO_2	S1/TOC Norm. Oil Content	Experimental Notations
SA-5	6980-7000	12.09	4.44	2.09	18.64	0.32	0.72	420	7	58	47	0.10	Low Temp S2 Shoulder
SA-6	7410-7440	7.15	6.54	2.30	34.33	0.48	0.80	525	7	72	35	0.06	
SA-7	4010-4020	10.13	0.50	0.15	0.41	0.33	0.81	82	66	1	30	0.27	
SA-8	4860-4880	33.14	1.78	0.80	7.36	0.35	0.69	431	20	21	45	0.10	Low Temp S2 Shoulder
SA-10	4980-5000	52.05	0.81	0.54	1.93	0.47	0.72	238	58	4	67	0.22	

Thermal maturity

To classify organic matter (Kerogen) in shale, the Pseudo Van Krevelen diagram was used. It is a modification of the Van Krevelen Plot, published in 1961. In this study, two index were determined, the Hydrogen Index (HI) and the Oxygen Index (OI). OI is pyrolyzable organic carbon (mg) divided by TOC. According to this diagram, the kerogens in the shale samples are of two types (Figure, 19). Three samples (SA-5, SA-6 and SA-8) were of type II kerogen, which corresponds to marine plankton-bearing sedimented in an anoxic environment. Two samples (SA-7 and SA-10) were found to be of type III kerogen, which corresponds to land-plant debris that sedimented in terrestrial environments in marine and lacustrine delta settings. These results are similar to the data that was described by Lambert (1992) and other studies in the same formation.

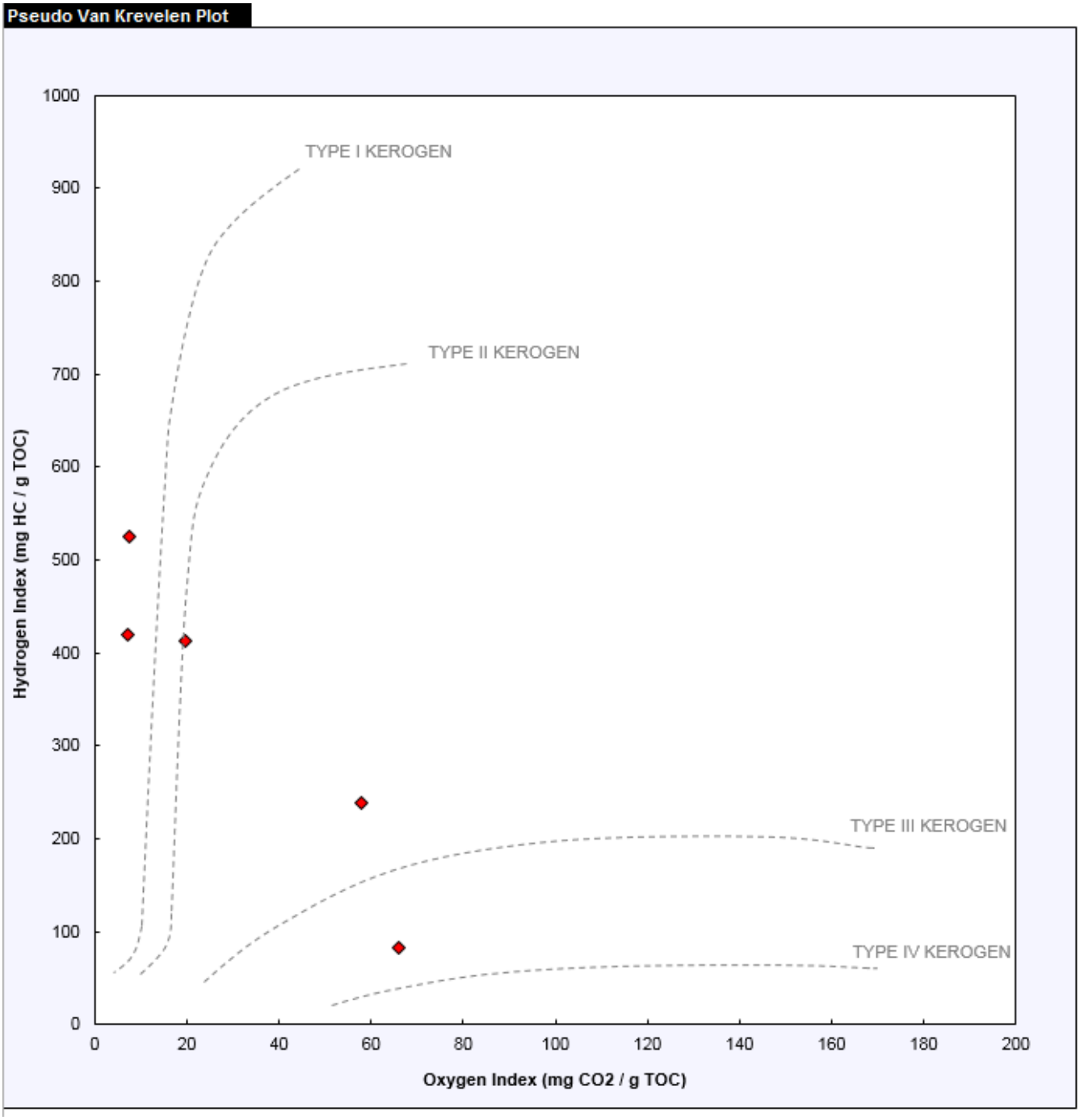

Figure 19: Van Krevelen diagram based on HI (mg HC/g TOC) versus OI (mg CO2/g TOC).

K-Ar Dates

K-Ar isotopic data of the < 2 μm clay fractions are presented in (Table 8). Radiogenic ^{40}Ar amounts ranged from 1.1667E-09 mol/g to 3.2621E-09 mol/g, and K amounts ranged from 1.93 wt% to 4.86 wt%. The following equation was used, to calculate the ages of clay minerals.

$$t = \frac{1}{\lambda} \ln \left[\frac{^{40}Ar}{^{40}K} \left(\frac{\lambda}{\lambda e} \right) + 1 \right]$$

Where (t) value is the age of the mineral, λ is total decay constant of ^{40}K and λe is the decay constant of ^{40}K to ^{40}Ar.

The K-Ar calculated dates ranged between 318.6 ± 7.9 Ma, corresponding to the time of Serpukhovian stage dating of the Upper Mississippian and 353.9 ± 7.9 Ma, corresponding to the time of Tournaisian stage dating of the Lower Mississippian (Gradstein and Ogg, 2004). All the clays indicated that dates were found to be younger than stratigraphic ages of the samples. The data illustrated a good linear correlation between both, K and radiogenic ^{40}Ar (Figure 20).

Table 8: K-Ar isotopic data of the < 2 µm clay fractions.

Sample ID	K [%]	Rad. ^{40}Ar [mol/g]	Rad. ^{40}Ar [%]	Age [Ma]	Gradstein and Ogg (2004) Timescale: Period –Epoch-stage
SA-5	4.86	3.2621E-09	96.63	350.6 ± 8.5	Carboniferous-Lower Mississippian-Tournaisian
SA-6	4.83	3.0942E-09	94.43	336.0 ± 8.0	Carboniferous-Middle Mississippian-Visean
SA-7	3.36	2.2789E-09	94.76	353.9 ± 7.9	Carboniferous-Lower Mississippian-Tournaisian
SA-8	2.46	1.5628E-09	93.89	333.9 ± 7.8	Carboniferous-Middle Mississippian-Visean
SA-10	1.93	1.1667E-09	91.27	318.6 ± 7.9	Carboniferous-Upper Mississippian-Serpukhovian

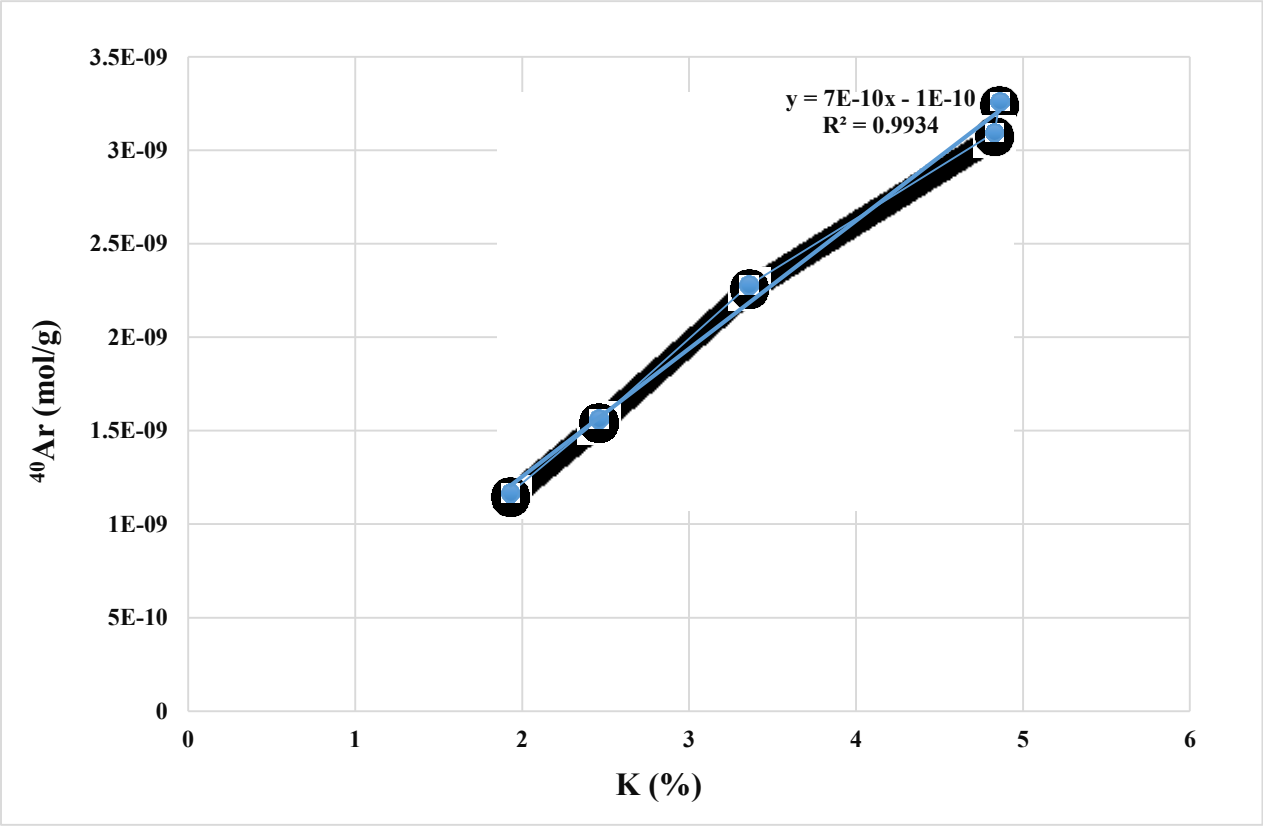

Figure 20: Correlation between K (%) and 40Ar.

Chapter 4 – Discussion

The dominant clay minerals present are discrete illite, with very small amounts of mixed-layer illite/smectite, chlorite and kaolinite. The illites have high crystallinity and they are of dioctahedral composition. The percentages of illite appeared to increase with an increase in depth as indicated by the semi-quantitative abundance data of three samples (SA-6, SA-7, and SA-8) that came from the same well (Figure 21). This may signify that a process associated with the burial had promoted diagenetic growths of illite in the Woodford Shale.

The concept of diagenetic growth is further supported by the K-Ar dates of the clays (318 and 353 Ma), which were lower than the stratigraphic depositional dates of the sediments that contained the clay minerals.

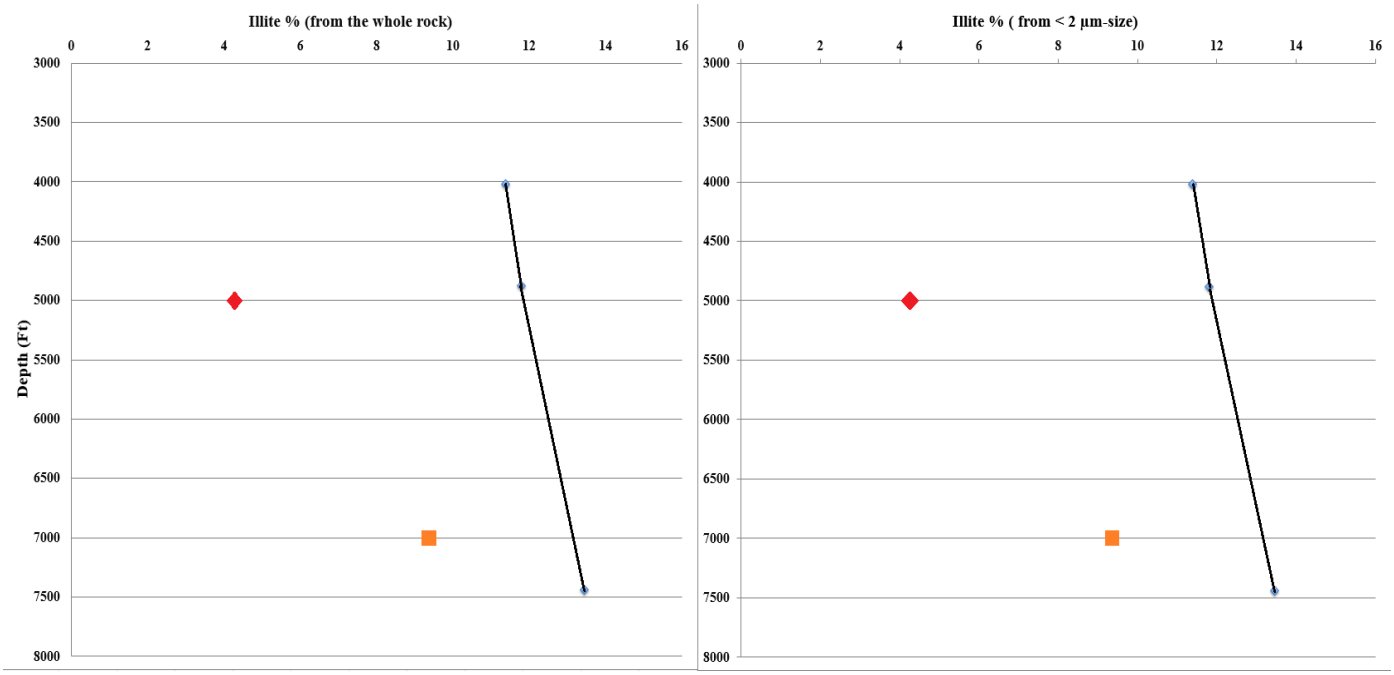

Figure 21: Black line illustrated vertical samples.

Diagenetic growths of illite in the Woodford Shale could have happened along two pathways: (a) solute reaction precipitation during burial diagenesis, the reaction of which may be expressed as:

$$K + Al + (Mg, Fe) + Si + H_2O \rightarrow \text{illite} ;$$

(b) transformation of smectite to illite during deep burial of the sediments, having the transformation as:

$$\text{Smectite} + (Al) + K \rightarrow \text{illite} + (Mg, Fe) + Si + H_2O$$

Regardless of the process by which illites formed in the Woodford Shale, a source of K must be available to drive the illite formation process. A large potential source of K for illitization in the Woodford Shale, is organic matter that is associated with sediments.

The contributions of organic source for K supply may be supported by evidence on K/Rb ratios. The K/Rb ratios of the clay fractions of the Woodford Shale were values between 160 and 207. If K and Rb had come from organic matter or kerogen with which the clays were associated, then one would have expected to see K/Rb ratios of the clays to be closer to the organic matter source. Chaudhuri et al., (2007) reported that the K/Rb ratios of modern organic materials are generally high with values between 350 and 10,000 or higher. The K/Rb ratios of the clays are much lower than the ratios of organic matter or plants; in fact lower than that of average crustal sedimentary rocks with values 250 and 350. A process must have operated to explain how the clays could have lower K/Rb ratios than organic matter source. It could be that clays received K and Rb from a solution, which was partly involved in oil generation, wherein oil received more K relative to Rb making the aqueous phase depleted in K/Rb ratios. It has been reported by Alvarez (2015) that K/Rb ratios of oil could be significantly higher than formation waters associated with oils.

The influence of organic matter on the history of diagenetic formation can be further supported by REE data. The REE contents were low for the clay fractions, which were enriched in MREE due to a possible link to the phosphate mineralization process. The low total REE contents of < 2 μm-size fraction clays in the Woodford Shale (as compared to average sedimentary rocks which may be represented by values given either Post Archean Australian Shale PAAS with 184 ppm or North America Shale Composite NASC with 178 ppm), may suggest that the clays formed during oil generation. To support this suggestion, it has been found by Alvarez (2015) that crude oils have higher specific REE concentrations than the associated formation waters.

Another diagenetic phenomenon of clay mineral formation within the Woodford Shale is revealed by chlorite-kaolinite relationship that has been found within the Woodford Shale. Analyses of samples from a single well seem to indicate an increase in chlorite content with an increase in depth (Figure 22), a feature of sediment diagenesis that has also been previously reported in the literature discussing about deeply buried sediments. Hower et al. (1976) presented a clear evidence of increase in chlorite content with an increase in depth, while kaolinite abundance is found to decrease with an increase in depth. The present study showed similar results. The formation of diagenetic chlorite may occur from dolomite-quartz-kaolinite reaction with water, forming calcite, chlorite and carbon dioxide. Hutcheon et al., (1980) expressed this reaction as:

$$10\ CaMg\ (CO_3)_2 + 2\ SiO_2 + Al_4\ Si_4\ O_{10}\ (OH)_8 + 2\ H_2O \rightarrow$$

$$10\ CaCO_3 + Mg_{10}\ Al_4\ Si_6\ O_{20}\ (OH)_{16} + 10\ CO_2$$

Another possible chlorite formation path is:

$$\text{Kaolinite} + Mg + Si + H_2O \rightarrow \text{Chlorite}$$

In fact, XRD data illustrated the presence of dolomite, quartz, kaolinite, calcite and chlorite in studied samples, as stated earlier. Magnesium is necessary to produce chlorite from kaolinite. This could obviously come from dolomite dissolution. Organic matter or kerogen may be a second source of Mg during hydrocarbon generation. Silicon is also needed to advance the kaolinite to chlorite reaction. It could come from dissolution of quartz and organic matter as well. Carbon dioxide is part of the reaction produced from kaolinite to chlorite conversion. Hydrous pyrolysis experiments, involving the reaction between water and rock chips, have noted CO_2 development. Studies of such experiments have explained that oxygen needed to form CO_2 essentially comes from H_2O (Lewan, 1997). The kaolinite decreased as the attendant chlorite increased, which could at least partly explain the CO_2 generation in natural environment.

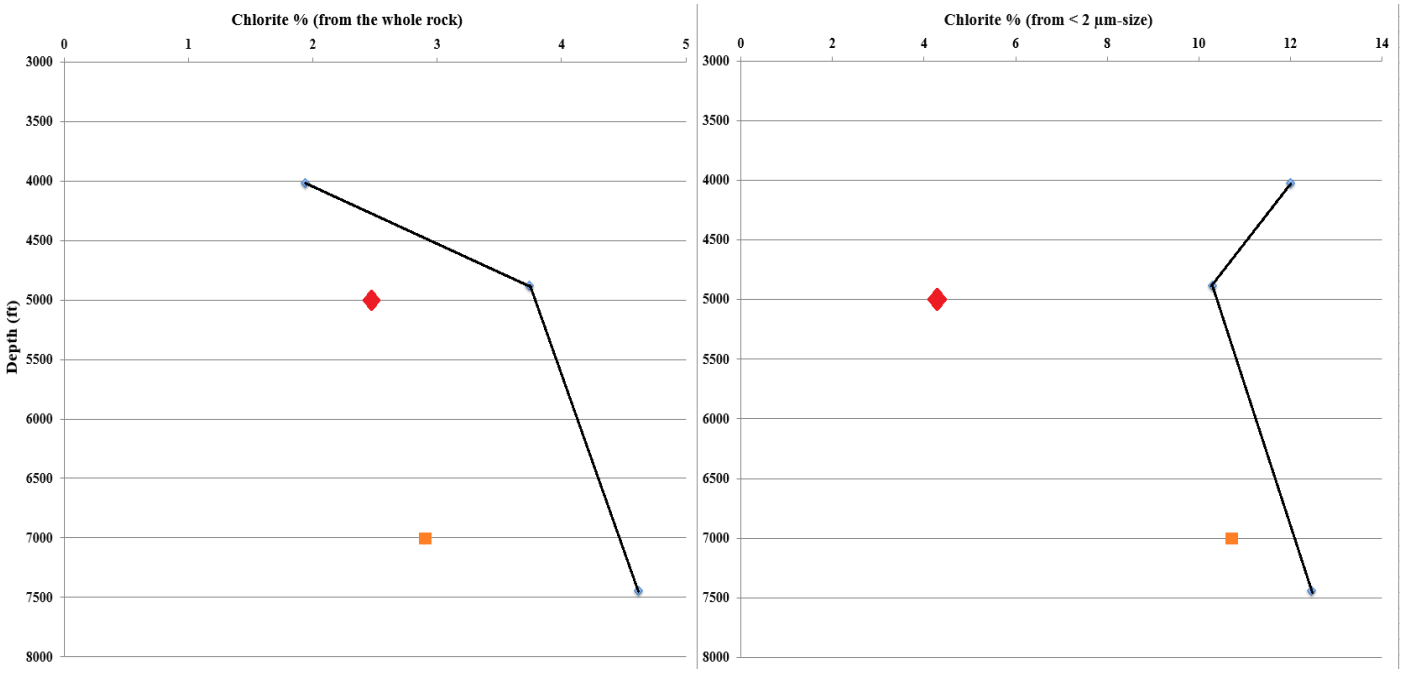

Figure 22: Chlorite (%) verses the depth (ft).

The non-clay minerals found in the Woodford Shale from this study include quartz, dolomite, calcite, Pyrite, feldspar (albite and microcline), fluorapatite and chlorapatite. No discernible trend could be established for these non-clay minerals with depth. In conclusion, the source of inorganic constituents that are needed to form clay minerals and others in the Woodford Shale could have come from preexisting minerals and the organic materials during their decomposition under thermal stress.

Uranium contents of < 2 μm-size fraction clays ranged approximately from 0.5 to 7 ppm. Thorium contents ranged from 0.6 to 1.2 ppm. U/Th ratios ranged between 0.2 and 9. Although the U are not as high as in marine black shales (20 ppm- 250 ppm) (Swanson, 1961; Lewan and Buchardt, 1989), the U/Th ratios of the clay fractions of the Woodford Shale are higher than that of average black shale and crustal rocks (Figure 11). Dilution by the presence of high amount of quartz could be one reason for the low U and Th contents of the Woodford Shale clay fractions. Another reason could be that the clays are inherently low in U and Th concentrations. Plants have been known with higher U/Th ratios than associated clay substrates. The clay fractions having a high U/Th ratio would then imply that the clays had some input of their U and Th from organic matter.

The total REE concentrations of the clay fractions in this study are low and ranged between 13 and 30 ppm, as compared to average sedimentary or crystalline rocks. The low values for the clay fractions could be attributed to dilution by quartz which is largely devoid of REE. A second explanation that could be suggested for low total REE contents of the clays, is that the clays formed diagenetically from solutes in formation water that was in close association with petroleum.

It has been found that petroleum can have higher specific REE concentrations than brines, the petroleum having higher concentrations than brines could have happened because

complexes with organic compounds generally have strong multi-dented sites for binding cations with high charge, such as REEs (Alvarez, 2015). This suggestion that the clays have had an association with organic environment is an agreement with previous explanation for their low K/Rb ratios.

The clay fractions are varied in their REE distribution patterns (Figures, 13-18). Alternatively, the clay fractions nearly the same patterns, but variations in the patterns resulted from the clays fractions containing different amounts of accessory non-clay minerals with different REE distribution patterns.

A common feature within the varied distribution patterns is presence of MREE enrichment. The MREE enrichment may be a reflection of the REE inherence from biologic sources or phosphate minerals. In fact, X-ray diffraction of random powder samples have shown the presence of fluorapatite and chlorapatite are included in studied samples. Phosphate minerals are an important group of REE-bearing materials. Many phosphate phases, such as apatite, monazite, and biogenic phosphate are known to be enriched in the MREE (Nagasawa, 1970; Gromet and Silver, 1983; Demartin et al., 1991; Grandjean and Albarede, 1989). In addition, chemical data (Table 6) indicated that phosphorus contents are varied in samples, which ranged from 37 to 432 ppm. For samples with high phosphorus contents, their MREE enrichment appeared high.

An important aspect of REE characteristics of clay fraction is the presence of the cerium (Ce) anomaly and some other anomalies in the clay fractions. Ce is the second element of series light rare earth element (LREE). The differences in Ce anomalies positive or negative, for samples that came from different localities could be linked to the differences in organic material sources. Studies have shown that Mn-oxyhydroxides (MnO_2) preferentially take-up Ce (IV), leaving the solution from which oxidized participation occurs to be depleted in Ce, a case that it seen with

ocean waters from which MnO_2 apparently participated to form MnO_2 nodules on ocean floors (Davranche, et al., 2005). Pourret et al., (2008) concluded from their studies that positive Ce anomalies have only been reported in alkaline water. They explained that positive Ce anomalies could be a common characteristics of alkaline, aerobic waters.

Anomaly of Eu is significant feature of the REE distribution patterns of the clay samples. The presences of Eu positive anomalies have been observed in some clay fractions (SA-4, SA-5 and SA-7). It has been commonly suggested that positive Eu anomalies are a response to a crystallographic factor, such as feldspar minerals which favor accommodations of Eu^{2+} over a trivalent species (Ramirez-Caro, 2013). Another explanation was suggested by Chaudhuri et al., (2007) that Eu positive anomalies in plants relative to their growth substrates. They believe that a plant enzyme effect plays an important role in Eu anomalies in the organic materials. Hence, the clay fractions showing Eu anomalies of varied magnitudes could be suggested of the REE in them in part of organic sources.

The PAAS-normalized distribution patterns of the REE in most samples commonly contained Gd positive anomalies. All samples also showed Ho anomaly. Gd and Ho, link all other HREEs have trivalent oxidation state. Therefore, Gd and Ho are not influenced by any change in the oxidation-reaction environment. Enzyme factors in biological roots could discriminate one or more REEs from the rest. Consequently, Gd and anomalies could be suggestive of the REEs in the clays in the clays coming from organic sources.

The PAAS-normalized REE distribution patterns for some clay minerals were formed with noticeable heavy rare earth element enrichment. The REE-carbonate complexes or REE-carboxylate complexes or both could explain such enrichment. If the anomalies and complexation

events happened during the same time, then organic matter transformation event is highlighted by these REE features.

The signatures of diagenetic influences are recorded by the K-Ar dates, which have been found to be post-Woodford Shale deposition time, at least for some samples. The K-Ar dates of illites from the Woodford shale indicated the clays being authigenic in origin. Discrete illite and mixed-layer illite/smectite occurring together may suggestive of two phases of illite formation. The K-Ar dates of illite ranged between 318.6 ± 7.9 Ma, corresponding to the time of Serpukhovian (age) stage within the Upper Mississippian and 353.9 ± 7.9 Ma, corresponding to the time of Tournaisian (age) stage within the Lower Mississippian. The date of illite from Mississippian Lime unit (SA-7) may be suggestive of diagenetic formation of the minerals shortly after the deposition of the sediments. Sample SA-7, SA-8 and SA-6 are form the same well, SA-7 being at the top and SA-6 being at the bottom within this vertical column (Figure 23).

SA-10 sample, from different a location had the lowest K content, lowest radiogenic ^{40}Ar and consequently had the youngest age of all samples. It suggests that some amounts of time, nearly 20-30 Ma Ma, have passed after the deposition period, for authugenic illites to form. This illitization event could be regarded as a period of hydrocarbon production in the Woodford Shale.

A study of petroleum system of the Woodford Shale by Higley et al., 2014, concluded that oil generation in the Woodford Shale started about 330 Ma. They established this timing for oil generation by analysis of vitrinite reflectance and transformation ratios through time from one-dimensional (1D) and four-dimensional (4D) models.

In the present study, a time difference of about 30-40 Ma has been seen from the time of the Middle the Woodford Shale began (about 360 Ma) to the time illite formation arising from

burial diagenesis happened about 318-326 Ma. Within this interval of 30-40 Ma time, the Woodford Shale had to be buried by about 853 m (2800 ft). By this time the earliest Middle Woodford Shale would have experienced a burial temperature of about 40-50 °C, based on geothermal gradient of 25 °C / 1000 m. This calculated burial temperature is about 20-30 °C short of the temperature needed. An estimate of additional sediment deposition would be about 1200 m, which will then make 318 date to be potential time of oil generation corresponding to Mississippian-Pennsylvanian time (Figure, 24).

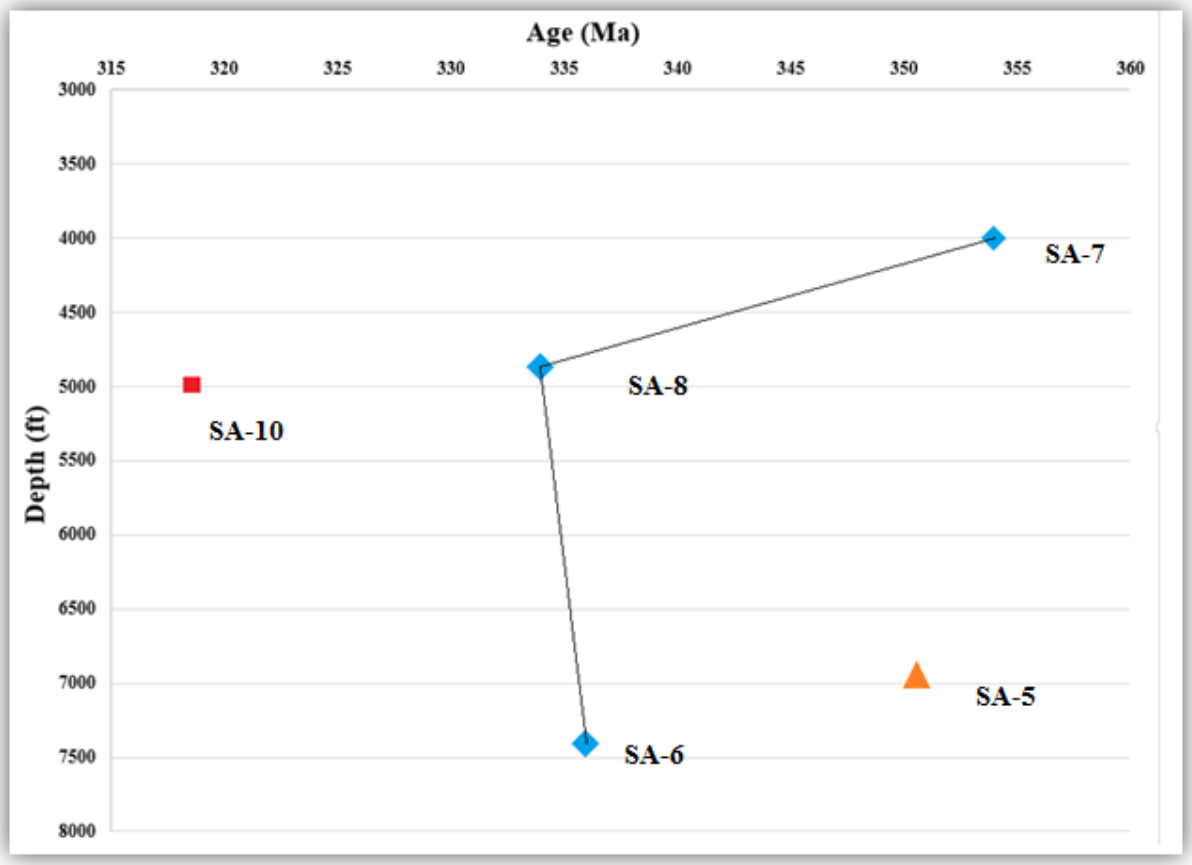

Figure 23: Age (Ma) versus depth (ft).

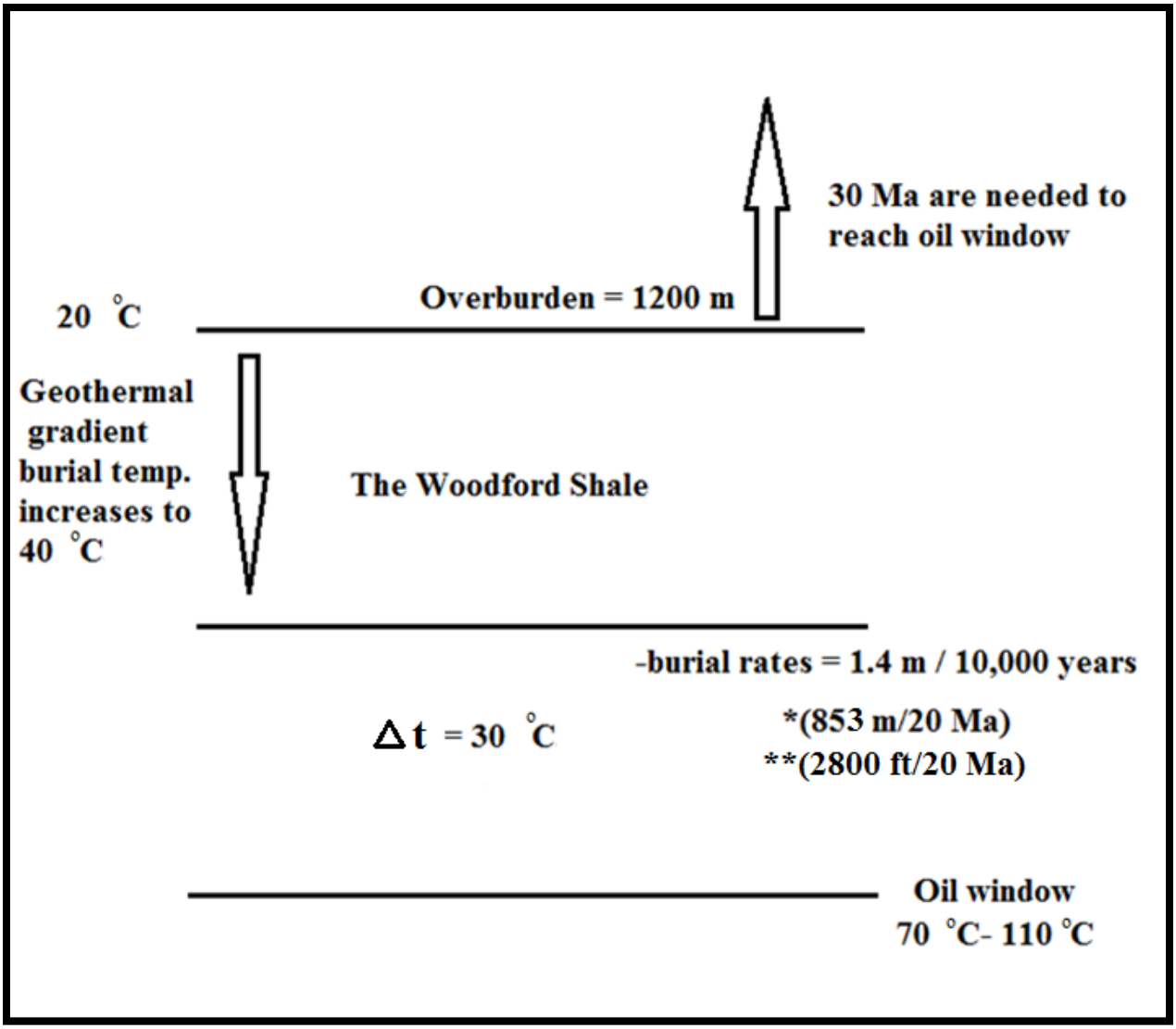

Figure 24: A load arising from additional deposition of sediments on top of it could provide the necessary temperature increase to reach the oil window of about 70°C.

Chapter 5 - Conclusion

The organic matter or kerogen undergoing maturation under thermal stress during burial could have provided K, at least in part, that was necessary to form diagenetic illite in the Woodford shale. Illitization might have been linked to oil generation process. The K-Ar dates of < 2 μm-size fraction clays suggest that oil in the Woodford Shale formed about 30 Ma after the deposition of the Woodford Shale. Inorganic constituents that are needed to form illite minerals and others in the Woodford Shale could have come from preexisting minerals and organic materials during their decomposition under thermal stress. The study provides some evidence that lends support to the suggestion that minerals, water, organic matter and gas interactions happening simultaneously should always be considered in the formation of oil generation.

References

Almon W. R. and Johns W. D., 1977. Petrleum-formaing reactions; The mechanisms and rate of clay catalyzed fatty acid decarboxylation, p. 157-172. In, R. Campos and Goni (eds.), Advances in organic Geochemistry: Nacional Adaro de Investigacions Minerals, S. A. Madrid.

Alvarez, H., 2015. Chemistry of Brine in an Unconventional Shale Dominated Source Bed: Understanding Water-Organic Material-Mineral Interactions During Hydrocarbon Generation. Thesis. Kansas State University Graduate School, 2015. Manhattan. Kansas State University.

Andrews, R.D., 2009. Production decline curves and payout thresholds of horizontal Woodford wells in the Arkoma Basin, Oklahoma: The Shale Shaker, v. 60, p. 103–112.

Bardenave, M. L., 1993. Applied Petroleum Geochemistry (p. 524pp). Paris: Éditions Technip.

Bebout, D.G., White, W.A., Hentz, T.F., and Grasmick,M.K., eds., 1993, Atlas of major mid-continent gas reservoirs: Bureau of Economic Geology, 85p.

Bonhomme, M.G., Thuizat, R., Pinault., Clauer, N., Wendling, R., Winker, R., 1975. Methode de datation potassium-argon. Apperillage et technique. Strasbourg, 53pp.

Cardott, B. J. 2009. Overview of Woodford Gas-Shale Play in Oklahoma." Woodford Gas Shale Conference. Oklahoma Geological Survey, 23 May 2007.

Chaudhuri S., Clauer N., Semhi K., 2007. Plant decay as a major control of river dissolved potassium, A first estimate: Chemical geology, v. 243, p.178-190.

Chaudhuri, S., Totten, M., Clauer, N., Miesse J., Riepl, G., Massie, S., Semhi, K., 2011. RareEarth Elements as a Useful Geochemical Tracer in Hydraulic Fracturing Schemes: Shale Shaker, The Journal of the Oklahoma City Geological Society, v. 62, p. 214-223.

Comer, J. B., 2008a. Reservoir Characteristics and Production Potential of the Woodford Shale. World Oil 229.

Comer, J.B., 2008. Reservoir characteristics and production potential of the Woodford Shale: World Oil, v. 229/8, p. 83-89.

Comer, J.B., Hinch, H.H., 1987. Recognizing and quantifying expulsion of oil from the Woodford Formation and age-equivalent rocks in Oklahoma and Arkansas: AAPG Bulletin, v. 71, No. 7, p 844-858.

Dalrymple, G. B., Lanphere, M.A., 1969. Potassium-Argon dating. W. H. Freeman, San Francisco, 258 P.

Davranche, M. O., Pourret, G., Grauau, A., Dia, M., Le Coz-Bouhnik, 2005. Adsorption of REE (III)-humate complexes onto MnO2, Experimental evidence for cerium anomaly and lanthanide tetrad effect suppression: Geochimica et Cosmochimica Acta v. 69, p. 4825-4835.

Demartin F., Pilati T., Diella V. Donzelli S. and Gramaccioli C.M., 1991. Alpine monazite: further data, Canadian Mineralogist, vol. 29, P. 61-67.

Eisma E. and Jurg J. W., 1967. Fundamental aspects of the diagenesis of organic matter and the formation of hydrocarbons, p. 61-72. In, 7th World Petroleum Congress Proceedings, v. 2, London, Elsevier.

Espitalié J., Madec M., and Tissot B., 1980. Role of mineral matrix in kerogen pyrolysis: Influence on Petroleum generation and migration: American Associtioin of Petroleum Geologist Bulletin, v. 64, p. 59-66.

Folk, R. L., 1968. Petrology of Sedimentary rocks: Hemphill`s, Austin, Taxes, 170.

Goldstein, S.J., and Jacobsen, S.B., 1988b. Rare earth elements in river waters. Earth and Planetary Science Letters. 89, 35-47.

Goldstein, S.J., and Jacobsen, S.B., 1988a. REE in the Great Whale River estuary, northwest Quebec. Earth and Planetary Science Letters. Sci. Left. 88, 24l-252.

Gradstein, F., Ogg, J., 2004. Geologic Time Scale 2004- why, how, and where next! 37(0024-1164.), 175-181. Retrieved February 16, 2015, from http://eesc.columbia.edu/courses/w4937/Readings/Gradstein_Ogg_2004.pdf

Gromet L.P, and Silver L.T., 1983. Rare earth element distributions among minerals in a granodiorite and their petrogenetic implications: Geochimiea et Cosmochimica Acta, vol. 47, p: 925-939.

Henry,M.E., and Hester, T.C., 1995, Anadarko Basin Province (058), in Gautir, D.L., Dolton, G.L., Takahashi, K.I., and Varnes, K.L., eds., 1995 National assessment of United State oil and gas resources on CD-Rom: U.S.Geological Survey Digital Date Series 30, 51 p. http://energy.cr.usgs.gov/oilgas/noga/1995.html.

Higley, D.K., Cook, T.A., Pawlewicz, M.J., 2014. Petroleum systems and assessment of undiscovered oil and gas in the Anadarko Basin Province, Colorado, Kansas, Oklahoma, and Texas—Woodford Shale Assessment Units, chap. 6, in Higley, D.K., compiler, Petroleum systems and assessment of undiscovered oil and gas in the Anadarko Basin Province, Colorado, Kansas, Oklahoma, and Texas—USGS Province 58: U.S. Geological Survey Digital Data Series DDS–69–EE, 24 p., http://dx.doi.org/10.3133/ds69EE.

Hower, J., Eslinger, E.V., Hower, M.E., and Perry, E.A., 1976. Mechanism of burial metamorphism of argillaceous sediment: 1. Mineralogical and chemical evidence. Geological Society of American Bulletin, 87, 725-737.

http://gsabulletin.gsapubs.org/content/87/5/725.full.pdf

Huc A. Y., Durand B., Roucache J., Vandenbroucke M., and Pittion J.L., 1986. Comparisons of three series of organic matter of continental origin: Organic Geochemistry, v. 10, p. 65-72.

Hunt J. M., 1995. Petroleum Geochemistry and Geology: W. H. Freeman and Co., New York, 743pp.

Hutcheon, I., Oldershaw, A., and Ghent, E. D., 1980. Diagenesis of Cretaceous sandstones of the Kootenay Formation at Elk Valley (southeast British Columbia) and MI. Allan (southwestern Alberta): Geochim. Cosmochim. Acta 44, 1425-1435.

Johnson, K.S., Cardott, B.J., 1992. Geologic framework and hydrocarbon source rocks of Oklahoma, in K.S. Johnson and B.J. Cardott, eds., Source rocks in the southern Midcontinent, 1990 symposium: OGS Circular 93, p. 21-37.

Johnson, K.S., Amsden, T.W., Denison, R.E., Dutton, S.P., Goldstein, A.G., Rascoe, B., Jr., Sutherland, P.K., and Thompson, D.M., 1989. Geology of the Southern Midcontinent: Oklahoma Geological Survey, Special Publication 89-2.

Keller, W., Reynolds, R., & Inoue, A., 1986. Morphology of Clay Minerals in the Smectite-to-Illite Conversion Series by Scanning Electron Microscopy. Clays and Clay Minerals, 34(2), 187-197. Retrieved December 18, 2014, from http://www.clays.org/journal/archive/volume 34/34-2-187.pdf

Kirkland, D.W., Denison, R.E., Summers, D.M., and Gormly, J.R., 1992. Geology and Organic Geochemistry of the Woodford Shale in the Criner Hills and Western Arbuckle Mountains, Oklahoma. Oklahoma Geological Survey Circular 93, 38-69.

Lambert, M.W., 1992. Internal Stratigraphy of the Chattanooga Shale in Kansas and Oklahoma. Oklahoma Geological Survey Circular 93, 1992.

Lewan, M.D., Buchardt, B., 1989. Irradiation of organic matter by uranium decay in the Alum Shale, Sweden: Geochimica et Cosmochimica Acta, v.53, p. 1307-1322.

Lewan, M.D., 1993. Laboratory simulation of petroleum formation- hydrous pyrolysis, p. 419-442. In, organic Geochemistry (eds. M. Engel and S. Mackoj: plenum press.

McCarthy, K., Rojas, K., Niemman M., Peters, K., Stankiewicz, A., 2011. Basic Petroleum Geochemistry for Source Rock Evaluation: Schlumberger Oilfield Review 23, no. 2, p. 32-43.

Miceli, A., 2010. Geochemical Characterization of the Woodford Shale, Central and Southeastern Oklahoma. Thesis. University of Oklahoma, 2010. University of Oklahoma, 2010.

Monin J. C. and Audibert A., 1988. Thermal cracking of heavy oil/mineral matrix systems: SPE Reservoir Engieering, paper 16269, November, 1988.

Moore, D.M. and Reynolds, R.C., 1997. Identification of Clay Minerals and Associated. In X-Ray Diffraction and the Identification and Analysis of Clay Minerals (Second Edition ed., p. 245). New York, New York: Oxford University Press.

Nagasawa H., 1970. Rare earth concentrations in zircons and apatites and their host dacites and granites; Earth and Planetary Science letters, vol. 9, p. 359-364.

Northcutt, R.A., and Campbell, J.A., 1995. Abstract: Geologic Provinces of Oklahoma, by R. A. Northcutt and J. A. Campbell; #90957. AAPG

Portas, R., 2009. Characterization and Origin of Fracture Patterns in the Woodford Shale in Southeastern Oklahoma for Application to Exploration and Development. Thesis. University of Oklahoma, 2009.

Pourret, O., Davranche, M., Gruau, G., and Dia, A. 2008. New insights into cerium anomalies in organic-rich alkaline waters. Chemical Geology, 251, 120–127-120–127. Retrieved March 7, 2015, from file:///C:/Users/labguest/Downloads/Pourret et al. chemgeol 2008.pdf .pdf

Ramirez-Caro, D., 2013. Rare Earth Elements (REE) as Geochemical Clues to Reconstruct Hydrocarbon Generation History. Thesis. Kansas State University Graduate School, 2013. Manhattan. Kansas State University.

Rascoe, B., Hyne, N.J., 1988. Petroleum geology of the mid-continent: Tulsa Geological Society Special Publication 3, 162 p.

Shimoyama A. and Johns W. D., 1971. Catalytic conversion of fatty acids to petroleum-like paraffins and their maturation: Nature, v. 232, p. 140-144.

Slatt, R., 2013. Sequence Stratigraphy of the Woodford Shale and Application to Drilling and Production. AAPG Search and Discovery, Article #50792. Retrieved March 1, 2015.

Steiger, R.H., Jager, E., 1976. Subcommission on geochronology: convention on the use of dacay constants in geo- and cosmochronology, Earth and Planetary.

Swanson, V.E., 1961. Geology and Geochemistry of Uranium in Marine Black Shales A Review. Uranium in Carbonaceous Rocks. United State Departemnt of The Interior. Geological Survey, p 70. http://pubs.usgs.gov/pp/0356c/report.pdf

Taylor, S.R., and McLennan, S.M., 1985. The continental crust: Its compostion and evolution: Oxford, Blackwell, 312.

Tissot, B., & Welte, D., 1984. Formation of Petroleum in Relation to Geological processes. Timing of Oil and Gas Generation. In Petroleum Formation and Occurrence (2nd edn., p. 699pp). Berlin: Springer-Verlag.

Ugochukwu, I., 2010. Subsurface Evalution of Source Rock and Hydrocarbon Potential of the Anambera Basin, South Eastern Nigeria. Retrieved January 2, 2015, from https://books.google.com/books?id=Ger5YmiUzCAC&pg=PA30&lpg=PA30&dq=Walkey and Black, 1934; Bauluz et al, 2000 and Wapples, 1985&source=bl&ots=wI8yHUczK0&sig=ms1wJSqFBL2q9vvVG-HRYsYNu58&hl=en&sa=X&ei=fv4UVdPVH5LkoASEuIH4DA&ved=0CB8Q6AEwAA#v=onepage&q=Walkey and Black, 1934; Bauluz et al, 2000 and Wapples, 1985&f=false

Waples D. W., 1980. Time and temperature in petroleum formation – application of Lopatin's method to petroleum exploration: American Association of Petroleum Geologists Bulletin, v. 64, p. 916-926.

Weiss A., 1963. Organic derivatives of mica-type layer-silicates: Angew. Chem. Internat. Edit., v. 2, p.134-144.

Wickstrom, C.W., Johnson, C.J., 2012. Structure and Stratigraphy of the Mississppian System, East of the Nemaha Uplift in Oklahoma: AAPG Search and Discovery Article #10442, Web accessed 14 April 2015. http://www.searchanddiscovery.com/documents/2012/10442wickstrom/ndx_wickstrom.pdf

Appendix A – XRD of oriented samples < 2 micro fraction clays

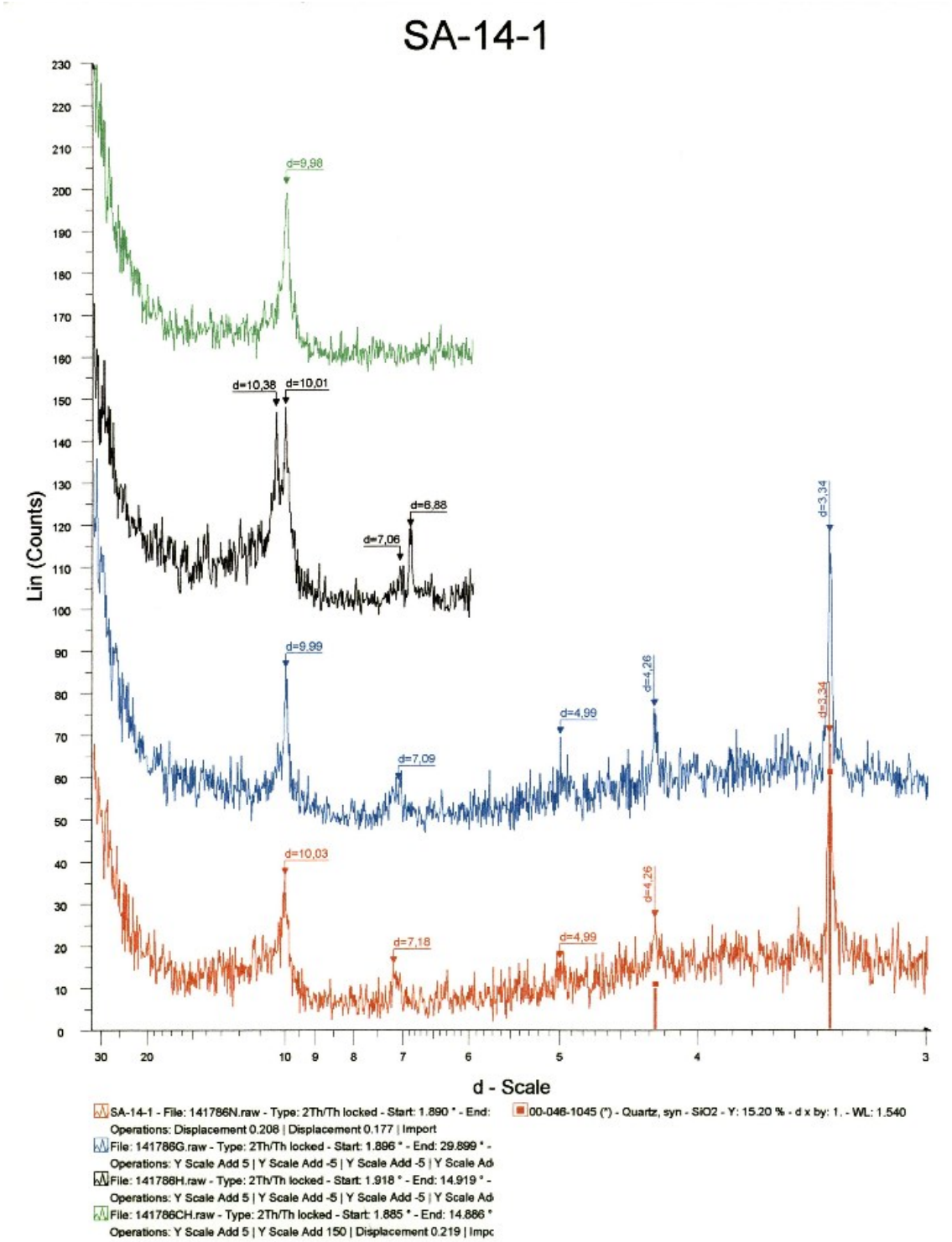

SA-14-2

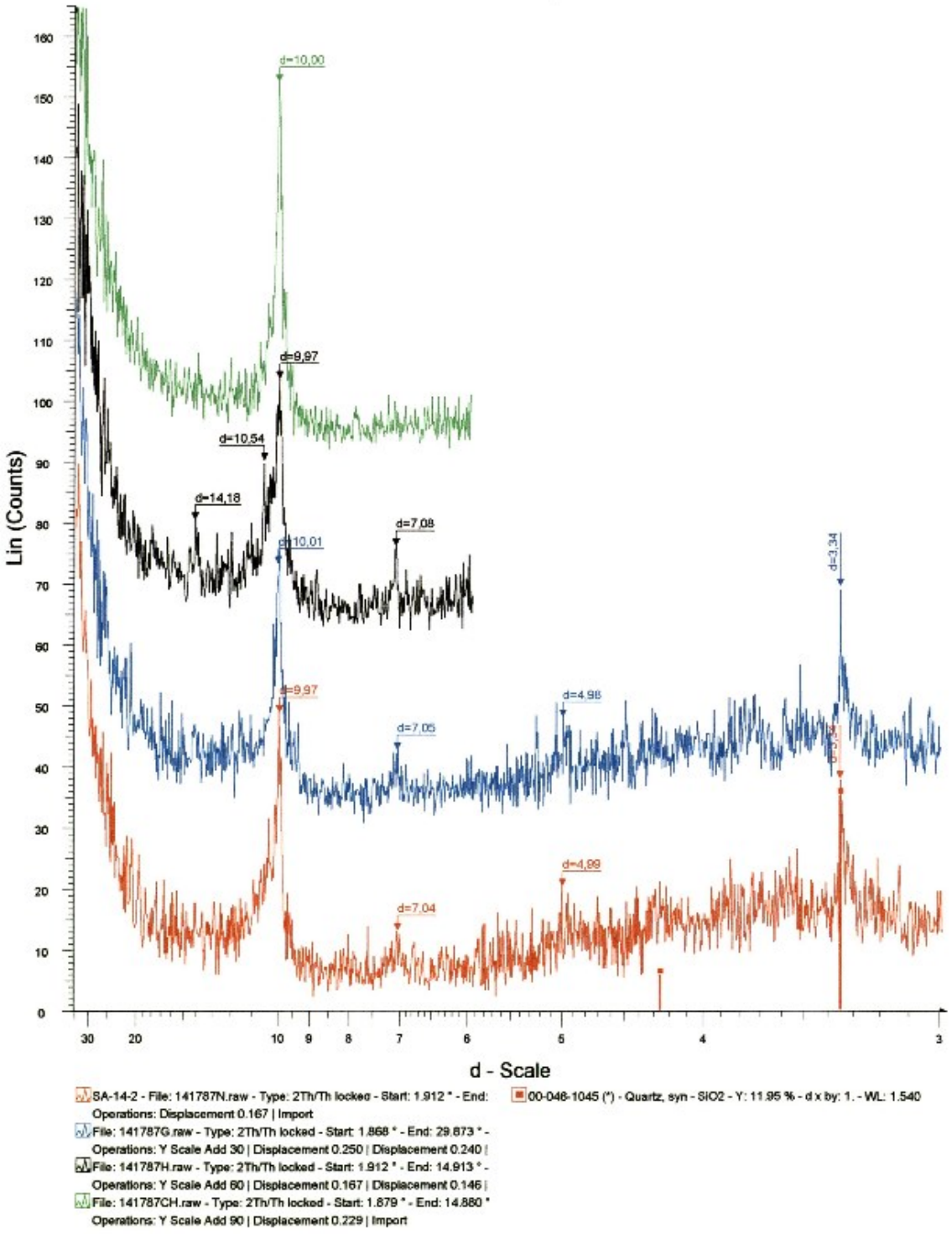
Lin (Counts)
d - Scale
d=10,00
d=9,97
d=10,54
d=14,18
d=7,08
d=10,01
d=3,34
d=4,98
d=7,05
d=4,99
d=7,04
SA-14-2 - File: 141787N.raw - Type: 2Th/Th locked - Start: 1.912 ° - End:
Operations: Displacement 0.167 | Import
File: 141787G.raw - Type: 2Th/Th locked - Start: 1.868 ° - End: 29.873 ° -
Operations: Y Scale Add 30 | Displacement 0.250 | Displacement 0.240 |
File: 141787H.raw - Type: 2Th/Th locked - Start: 1.912 ° - End: 14.913 ° -
Operations: Y Scale Add 60 | Displacement 0.167 | Displacement 0.146 |
File: 141787CH.raw - Type: 2Th/Th locked - Start: 1.879 ° - End: 14.880 °
Operations: Y Scale Add 90 | Displacement 0.229 | Import
00-046-1045 (*) - Quartz, syn - SiO2 - Y: 11.95 % - d x by: 1. - WL: 1.540

SA-14-3

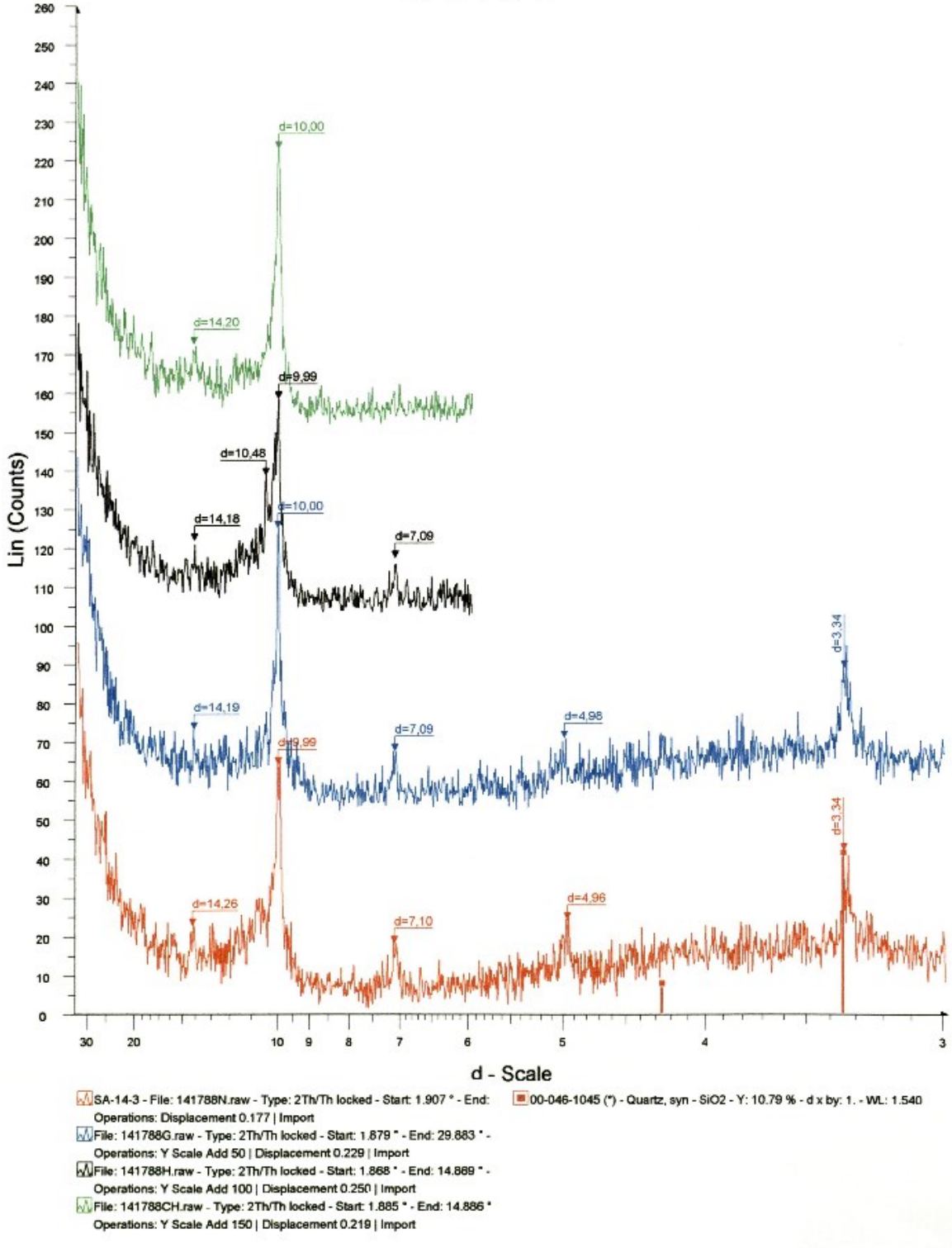
Lin (Counts)
d - Scale
d=10,00
d=14,20
d=9,99
d=10,48
d=14,18
d=10,00
d=7,09
d=3,34
d=14,19
d=7,09
d=4,98
d=9,99
d=3,34
d=14,26
d=7,10
d=4,96
SA-14-3 - File: 141788N.raw - Type: 2Th/Th locked - Start: 1.907 ° - End:
Operations: Displacement 0.177 | Import
File: 141788G.raw - Type: 2Th/Th locked - Start: 1.879 ° - End: 29.883 ° -
Operations: Y Scale Add 50 | Displacement 0.229 | Import
File: 141788H.raw - Type: 2Th/Th locked - Start: 1.868 ° - End: 14.889 ° -
Operations: Y Scale Add 100 | Displacement 0.250 | Import
File: 141788CH.raw - Type: 2Th/Th locked - Start: 1.885 ° - End: 14.886 °
Operations: Y Scale Add 150 | Displacement 0.219 | Import
00-046-1045 (*) - Quartz, syn - SiO2 - Y: 10.79 % - d x by: 1. - WL: 1.540

SA-14-4

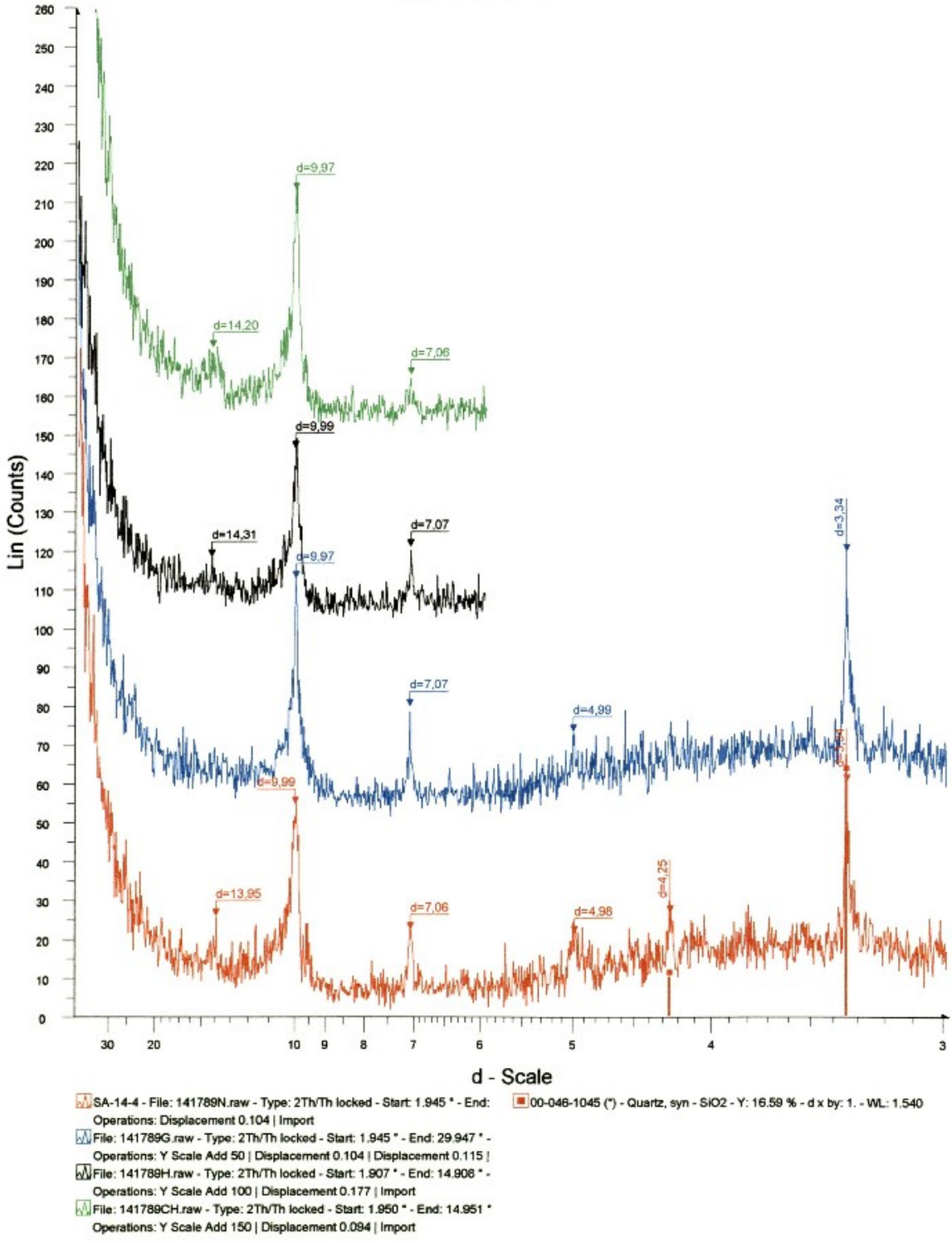
Lin (Counts)
d - Scale
d=9,97
d=14,20
d=7,06
d=9,99
d=14,31
d=7,07
d=9,97
d=3,34
d=7,07
d=4,99
d=9,99
d=13,95
d=7,06
d=4,98
d=4,25
SA-14-4 - File: 141789N.raw - Type: 2Th/Th locked - Start: 1.945 ° - End:
Operations: Displacement 0.104 | Import
File: 141789G.raw - Type: 2Th/Th locked - Start: 1.945 ° - End: 29.947 ° -
Operations: Y Scale Add 50 | Displacement 0.104 | Displacement 0.115 |
File: 141788H.raw - Type: 2Th/Th locked - Start: 1.907 ° - End: 14.908 ° -
Operations: Y Scale Add 100 | Displacement 0.177 | Import
File: 141788CH.raw - Type: 2Th/Th locked - Start: 1.950 ° - End: 14.951 °
Operations: Y Scale Add 150 | Displacement 0.094 | Import
00-046-1045 (*) - Quartz, syn - SiO2 - Y: 16.59 % - d x by: 1. - WL: 1.540

SA-14-5

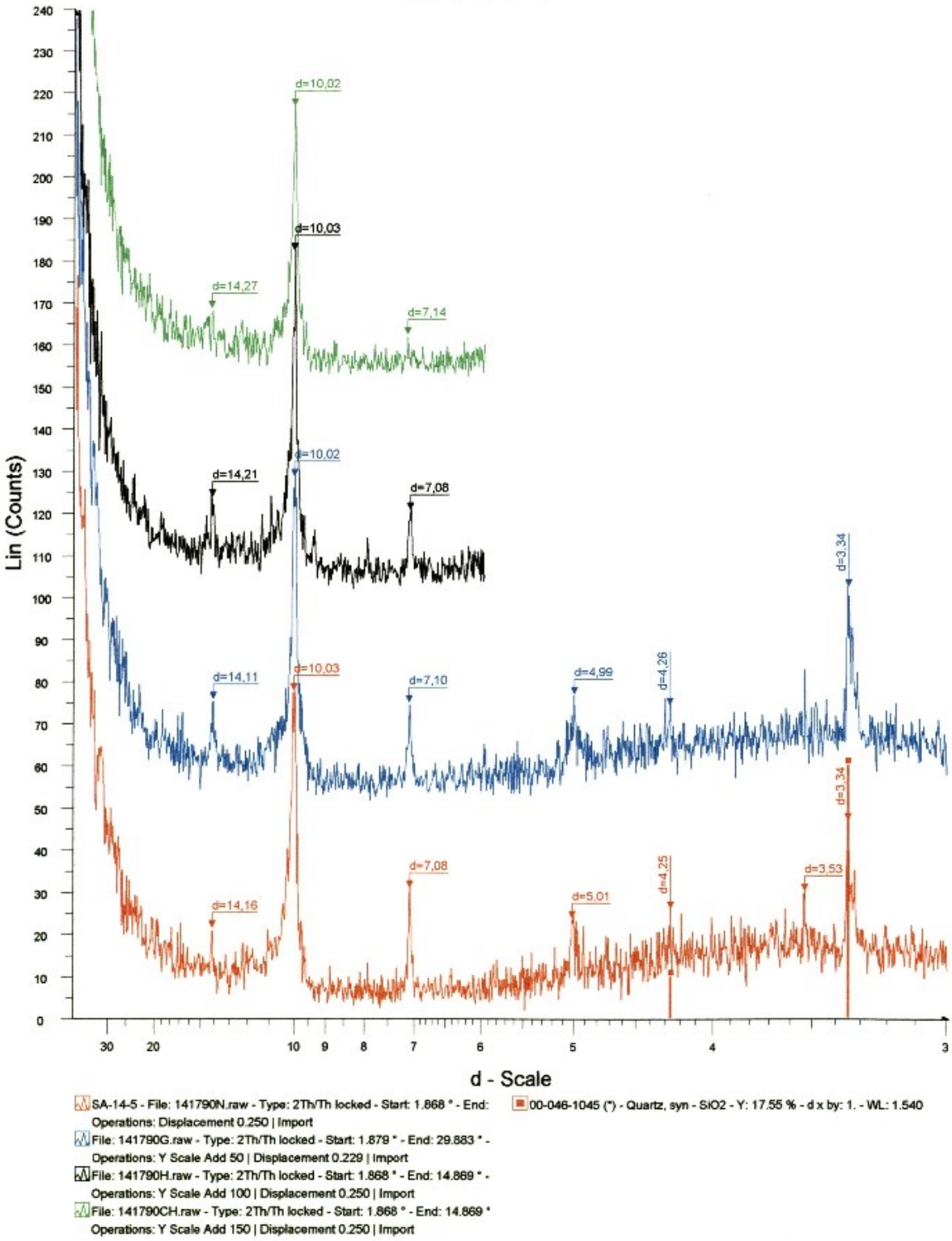
Lin (Counts)
d - Scale
d=10,02
d=10,03
d=14,27
d=7,14
d=14,21
d=10,02
d=7,08
d=3,34
d=14,11
d=10,03
d=7,10
d=4,99
d=4,26
d=3,34
d=7,08
d=14,16
d=5,01
d=4,25
d=3,53
SA-14-5 - File: 141790N.raw - Type: 2Th/Th locked - Start: 1.868 ° - End:
Operations: Displacement 0.250 | Import
File: 141790G.raw - Type: 2Th/Th locked - Start: 1.879 ° - End: 29.883 ° -
Operations: Y Scale Add 50 | Displacement 0.229 | Import
File: 141790H.raw - Type: 2Th/Th locked - Start: 1.868 ° - End: 14.869 ° -
Operations: Y Scale Add 100 | Displacement 0.250 | Import
File: 141790CH.raw - Type: 2Th/Th locked - Start: 1.868 ° - End: 14.869 °
Operations: Y Scale Add 150 | Displacement 0.250 | Import
00-046-1045 (*) - Quartz, syn - SiO2 - Y: 17.55 % - d x by: 1. - WL: 1.540

SA-14-6

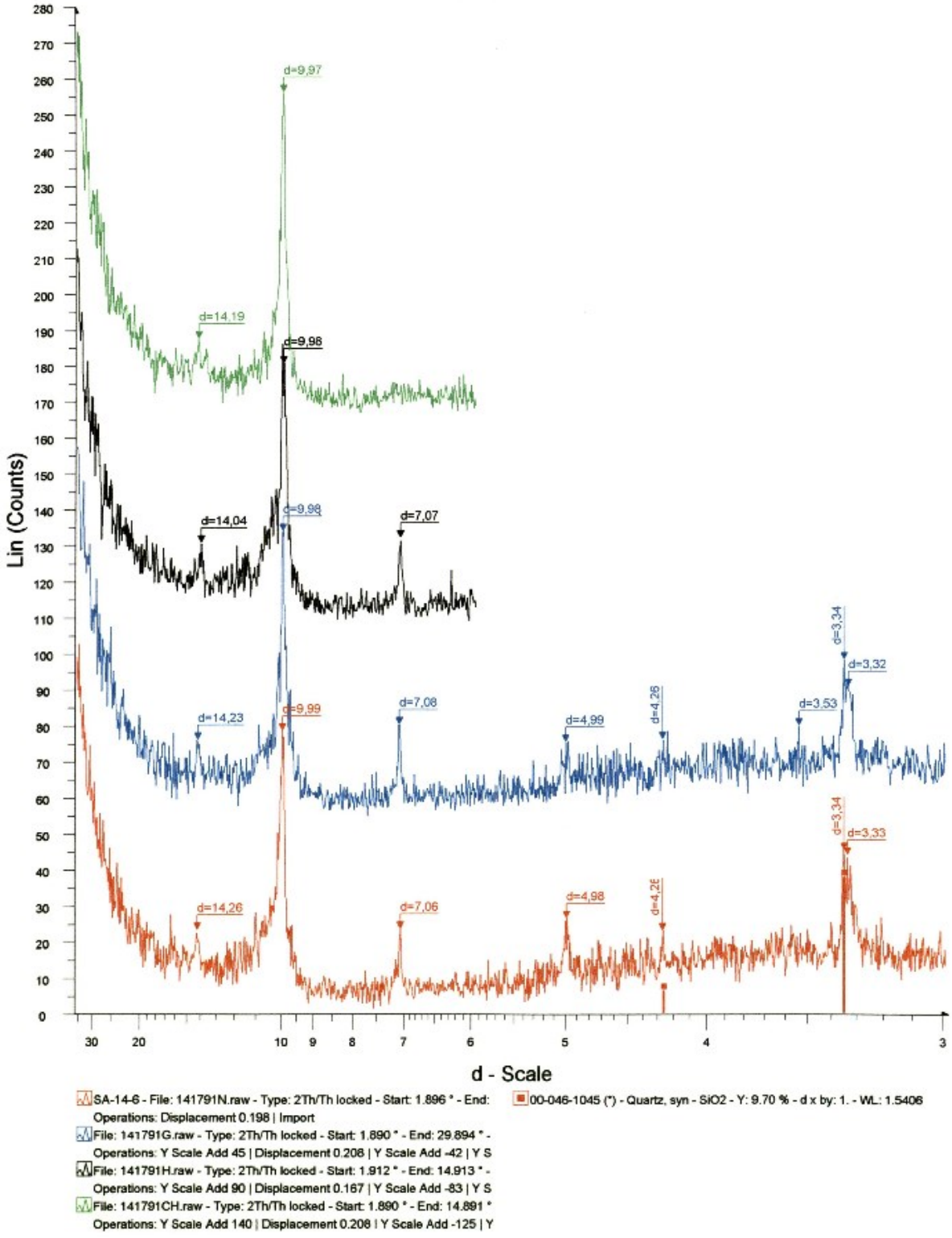
Lin (Counts)
d - Scale
d=9,97
d=14,19
d=9,98
d=14,04
d=9,98
d=7,07
d=14,23
d=9,99
d=7,08
d=4,99
d=4,26
d=3,53
d=3,34
d=3,32
d=14,26
d=7,06
d=4,98
d=4,26
d=3,34
d=3,33
SA-14-6 - File: 141791N.raw - Type: 2Th/Th locked - Start: 1.896 ° - End:
Operations: Displacement 0.198 | Import
File: 141791G.raw - Type: 2Th/Th locked - Start: 1.890 ° - End: 29.894 ° -
Operations: Y Scale Add 45 | Displacement 0.208 | Y Scale Add -42 | Y S
File: 141791H.raw - Type: 2Th/Th locked - Start: 1.912 ° - End: 14.913 ° -
Operations: Y Scale Add 90 | Displacement 0.167 | Y Scale Add -83 | Y S
File: 141791CH.raw - Type: 2Th/Th locked - Start: 1.890 ° - End: 14.891 °
Operations: Y Scale Add 140 | Displacement 0.208 | Y Scale Add -125 | Y
00-046-1045 (*) - Quartz, syn - SiO2 - Y: 9.70 % - d x by: 1. - WL: 1.5406

SA-14-7

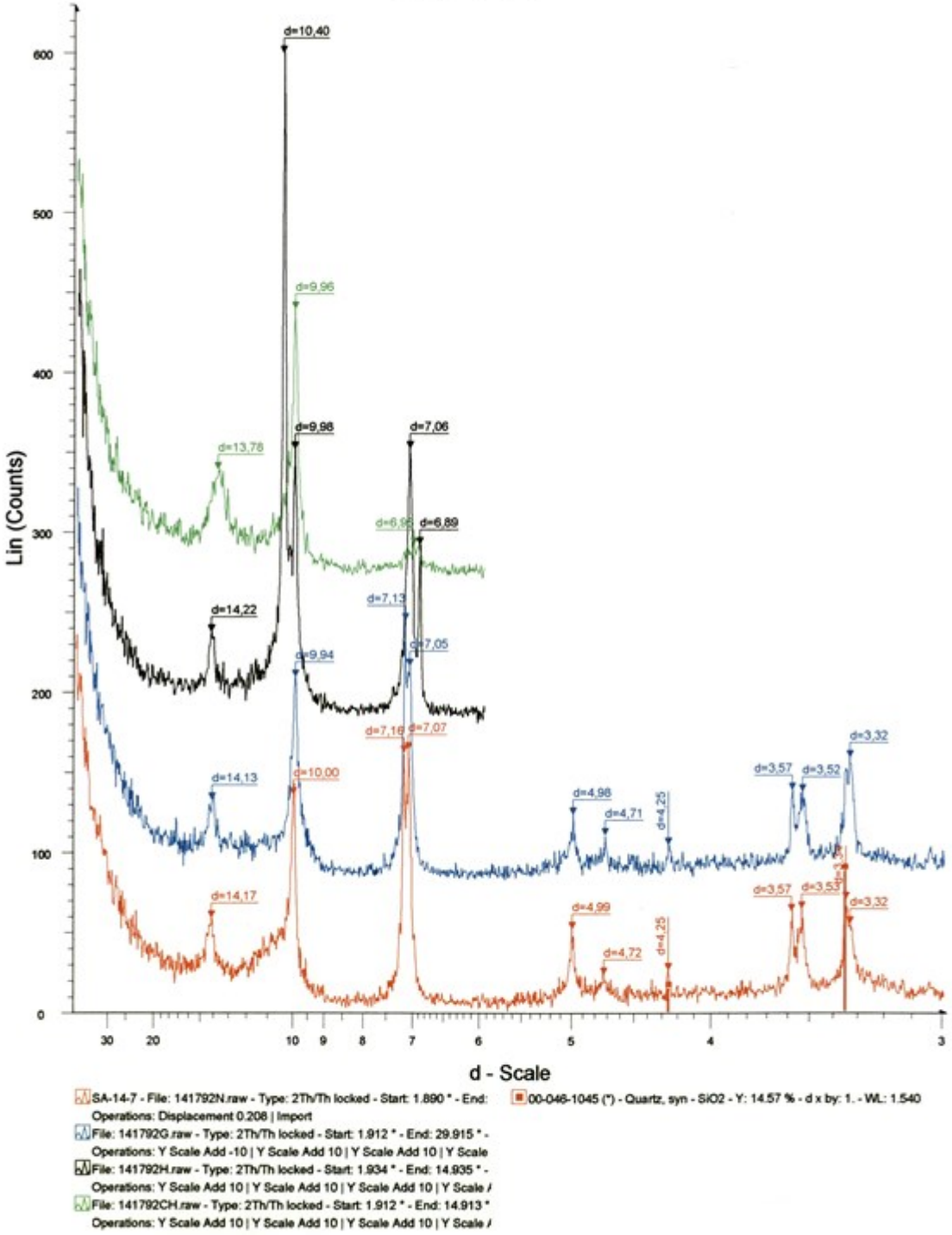
Lin (Counts)
d - Scale
d=10,40
d=9,96
d=9,98
d=7,06
d=13,78
d=6,96
d=6,89
d=14,22
d=7,13
d=7,05
d=9,94
d=7,16
d=7,07
d=14,13
d=10,00
d=4,98
d=4,71
d=4,25
d=3,57
d=3,52
d=3,32
d=14,17
d=4,99
d=4,72
d=4,25
d=3,57
d=3,53
d=3,32
SA-14-7 - File: 141792N.raw - Type: 2Th/Th locked - Start: 1.890 * - End:
Operations: Displacement 0.208 | Import
File: 141792G.raw - Type: 2Th/Th locked - Start: 1.912 * - End: 29.915 * -
Operations: Y Scale Add -10 | Y Scale Add 10 | Y Scale Add 10 | Y Scale
File: 141792H.raw - Type: 2Th/Th locked - Start: 1.934 * - End: 14.935 * -
Operations: Y Scale Add 10 | Y Scale Add 10 | Y Scale Add 10 | Y Scale A
File: 141792CH.raw - Type: 2Th/Th locked - Start: 1.912 * - End: 14.913 *
Operations: Y Scale Add 10 | Y Scale Add 10 | Y Scale Add 10 | Y Scale A
00-046-1045 (*) - Quartz, syn - SiO2 - Y: 14.57 % - d x by: 1. - WL: 1.540

SA-14-8

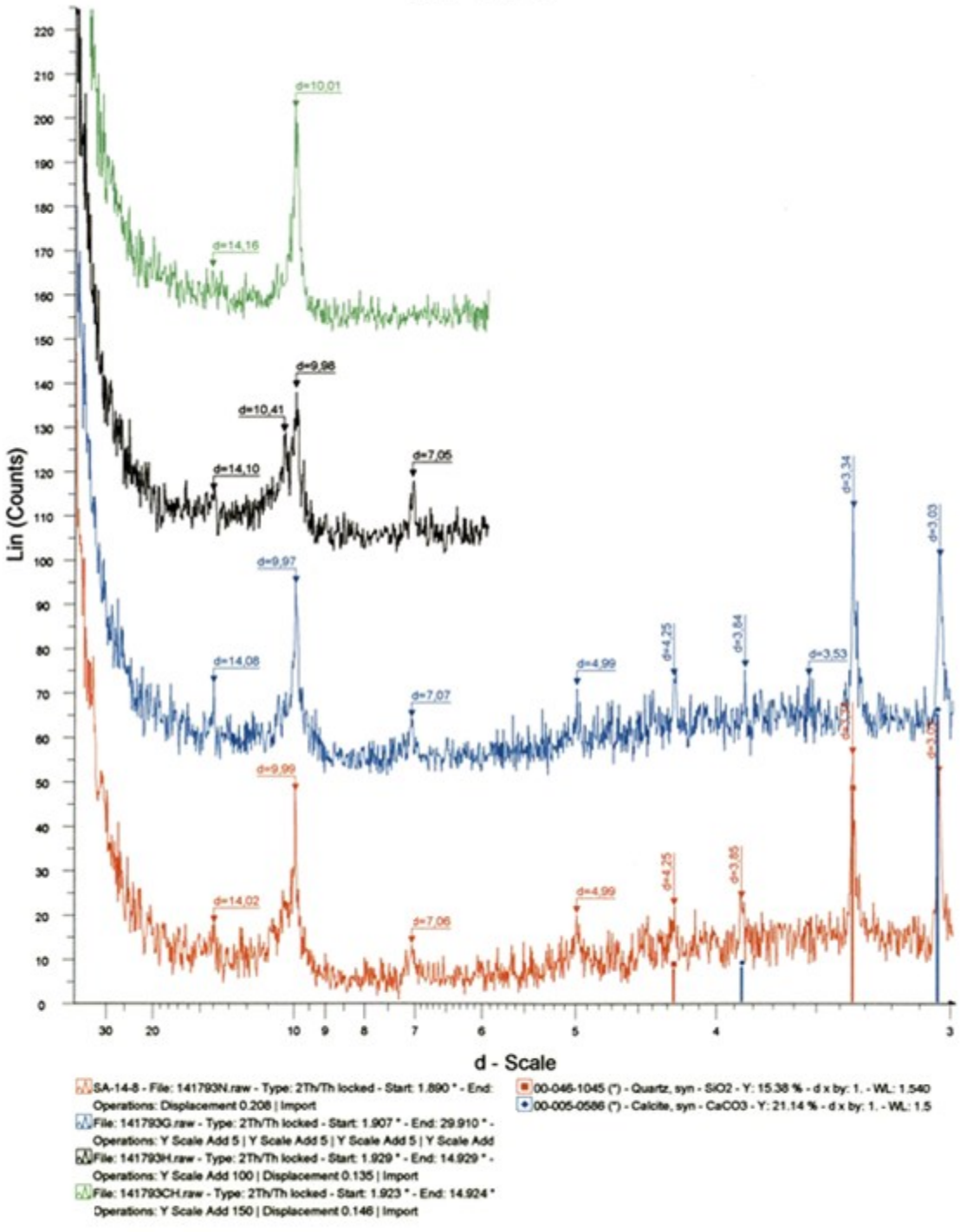
Lin (Counts)
d - Scale
d=10,01
d=14,16
d=9,96
d=10,41
d=14,10
d=7,05
d=9,97
d=14,08
d=7,07
d=4,99
d=4,25
d=3,84
d=3,53
d=3,34
d=3,03
d=9,99
d=14,02
d=7,06
d=4,99
d=4,25
d=3,85
SA-14-8 - File: 141793N.raw - Type: 2Th/Th locked - Start: 1.890 ° - End:
Operations: Displacement 0.208 | Import
File: 141793G.raw - Type: 2Th/Th locked - Start: 1.907 ° - End: 29.910 ° -
Operations: Y Scale Add 5 | Y Scale Add 5 | Y Scale Add 5 | Y Scale Add
File: 141793H.raw - Type: 2Th/Th locked - Start: 1.929 ° - End: 14.929 ° -
Operations: Y Scale Add 100 | Displacement 0.135 | Import
File: 141793CH.raw - Type: 2Th/Th locked - Start: 1.923 ° - End: 14.924 °
Operations: Y Scale Add 150 | Displacement 0.146 | Import
00-046-1045 (*) - Quartz, syn - SiO2 - Y: 15.38 % - d x by: 1. - WL: 1.540
00-005-0586 (*) - Calcite, syn - CaCO3 - Y: 21.14 % - d x by: 1. - WL: 1.5

SA-14-9

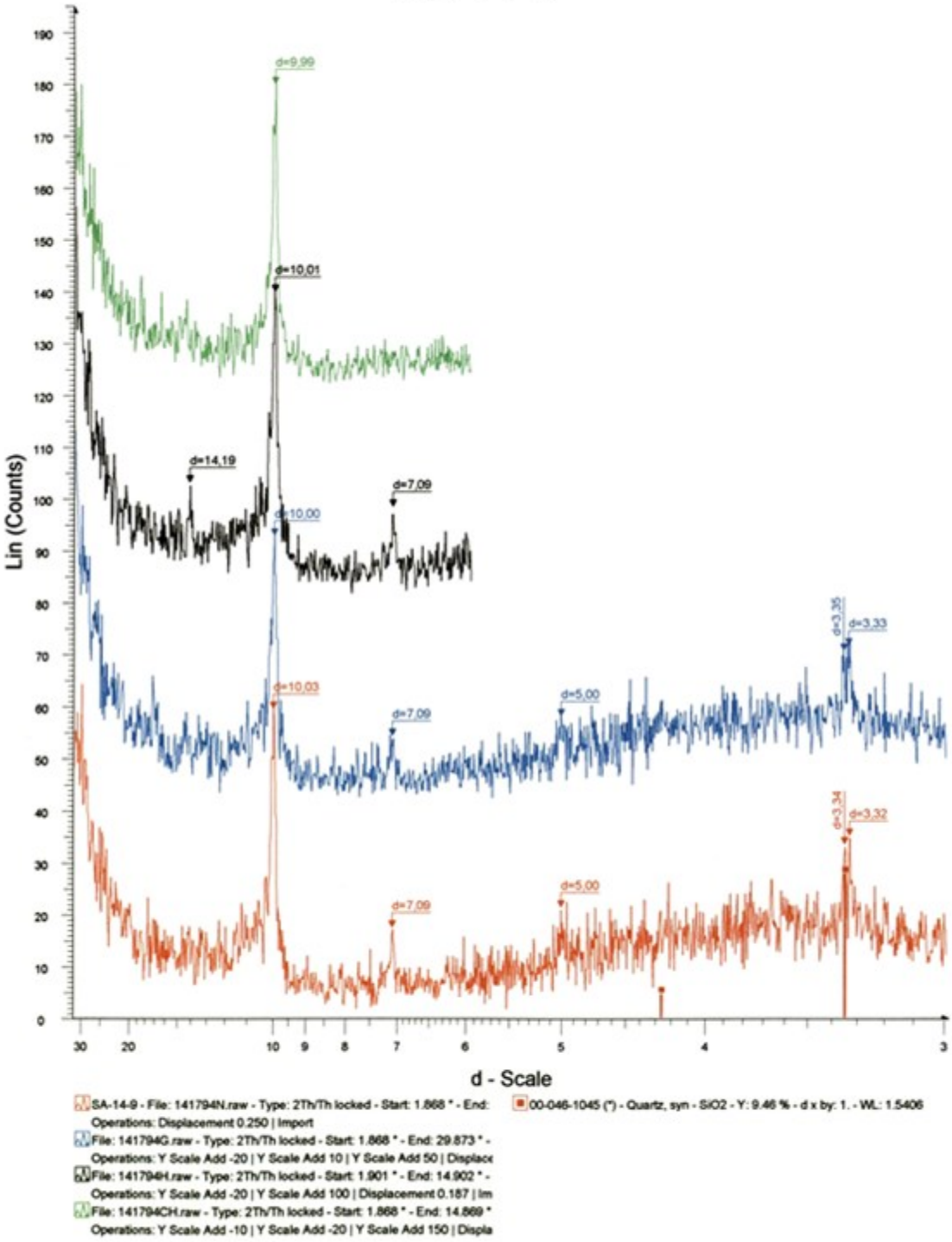
Lin (Counts)
d - Scale
d=9,99
d=10,01
d=14,19
d=7,09
d=10,00
d=3,35
d=3,33
d=10,03
d=7,09
d=5,00
d=3,34
d=3,32
d=7,09
d=5,00
SA-14-9 - File: 141794N.raw - Type: 2Th/Th locked - Start: 1.868 ° - End:
Operations: Displacement 0.250 | Import
File: 141794G.raw - Type: 2Th/Th locked - Start: 1.868 ° - End: 29.873 ° -
Operations: Y Scale Add -20 | Y Scale Add 10 | Y Scale Add 50 | Displace
File: 141794H.raw - Type: 2Th/Th locked - Start: 1.901 ° - End: 14.902 ° -
Operations: Y Scale Add -20 | Y Scale Add 100 | Displacement 0.187 | Im
File: 141794CH.raw - Type: 2Th/Th locked - Start: 1.868 ° - End: 14.869 °
Operations: Y Scale Add -10 | Y Scale Add -20 | Y Scale Add 150 | Displa
00-046-1045 (*) - Quartz, syn - SiO2 - Y: 9.46 % - d x by: 1. - WL: 1.5406

SA-14-10

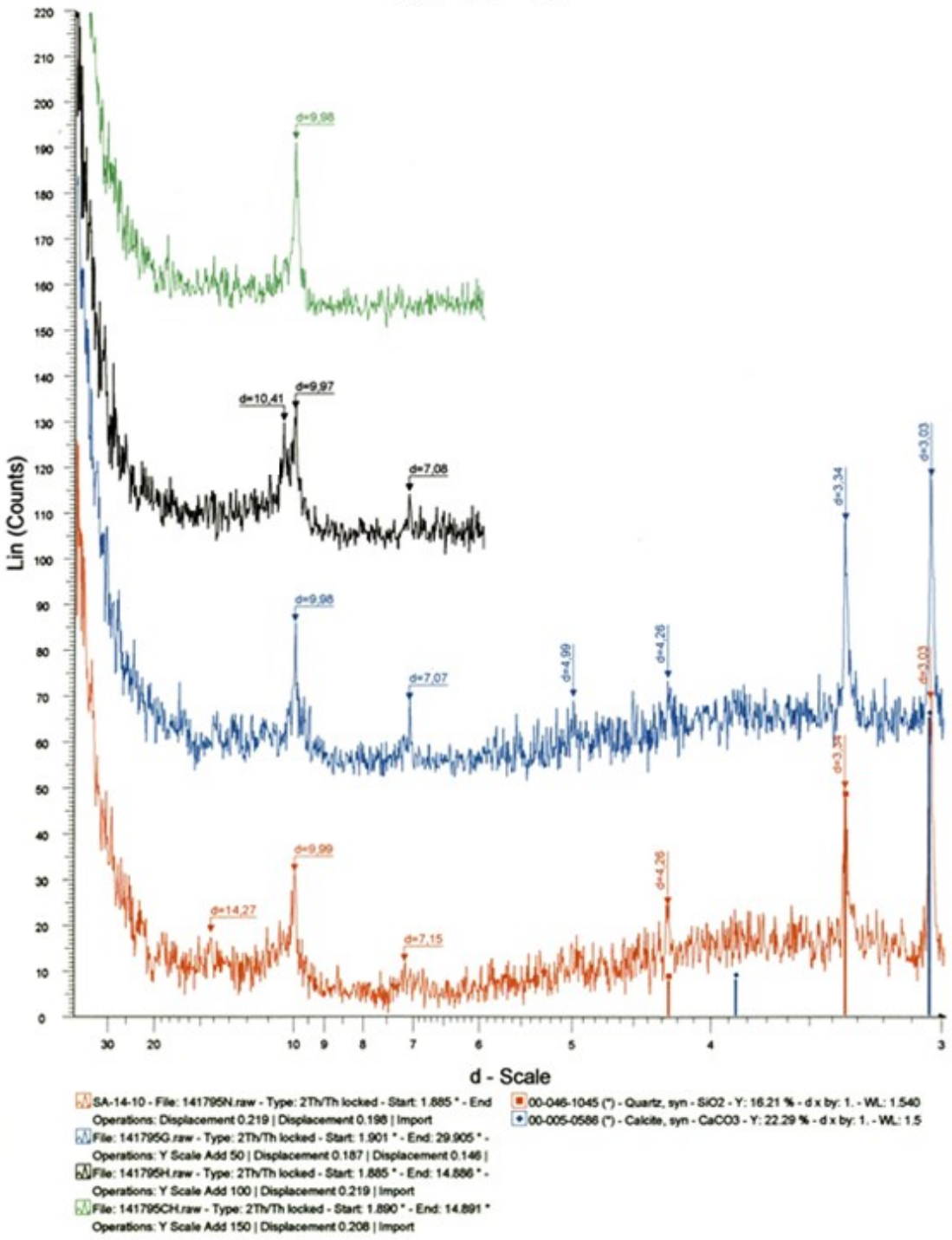
Lin (Counts)
d - Scale
d=9,98
d=10,41
d=9,97
d=7,08
d=9,98
d=7,07
d=4,99
d=4,26
d=3,34
d=3,03
d=9,99
d=14,27
d=7,15
d=4,26
d=3,34
SA-14-10 - File: 141795N.raw - Type: 2Th/Th locked - Start: 1.885 ° - End
Operations: Displacement 0.219 | Displacement 0.198 | Import
File: 141795G.raw - Type: 2Th/Th locked - Start: 1.901 ° - End: 29.905 ° -
Operations: Y Scale Add 50 | Displacement 0.187 | Displacement 0.146 |
File: 141795H.raw - Type: 2Th/Th locked - Start: 1.885 ° - End: 14.886 ° -
Operations: Y Scale Add 100 | Displacement 0.219 | Import
File: 141795CH.raw - Type: 2Th/Th locked - Start: 1.890 ° - End: 14.891 °
Operations: Y Scale Add 150 | Displacement 0.208 | Import
00-046-1045 (*) - Quartz, syn - SiO2 - Y: 16.21 % - d x by: 1. - WL: 1.540
00-005-0586 (*) - Calcite, syn - CaCO3 - Y: 22.29 % - d x by: 1. - WL: 1.5

Appendix B – XRD of random powder samples whole-rock

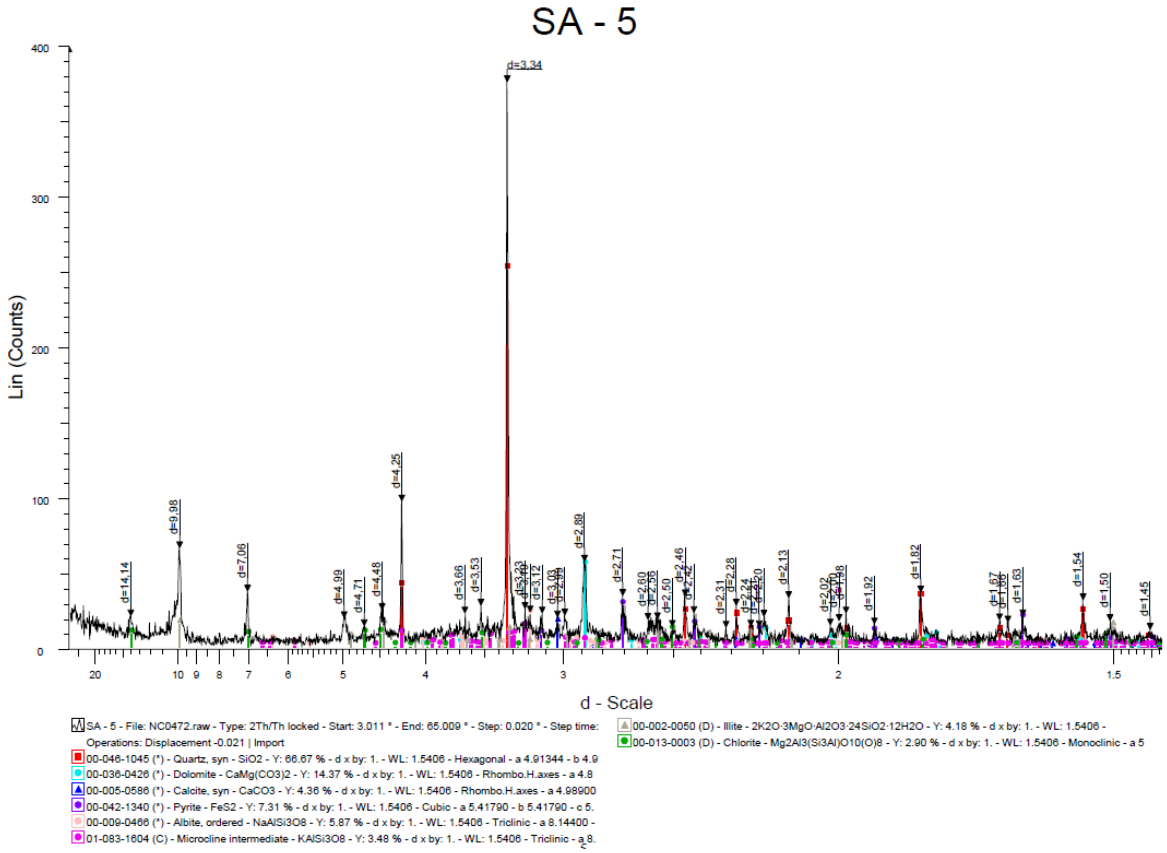

SA - 6

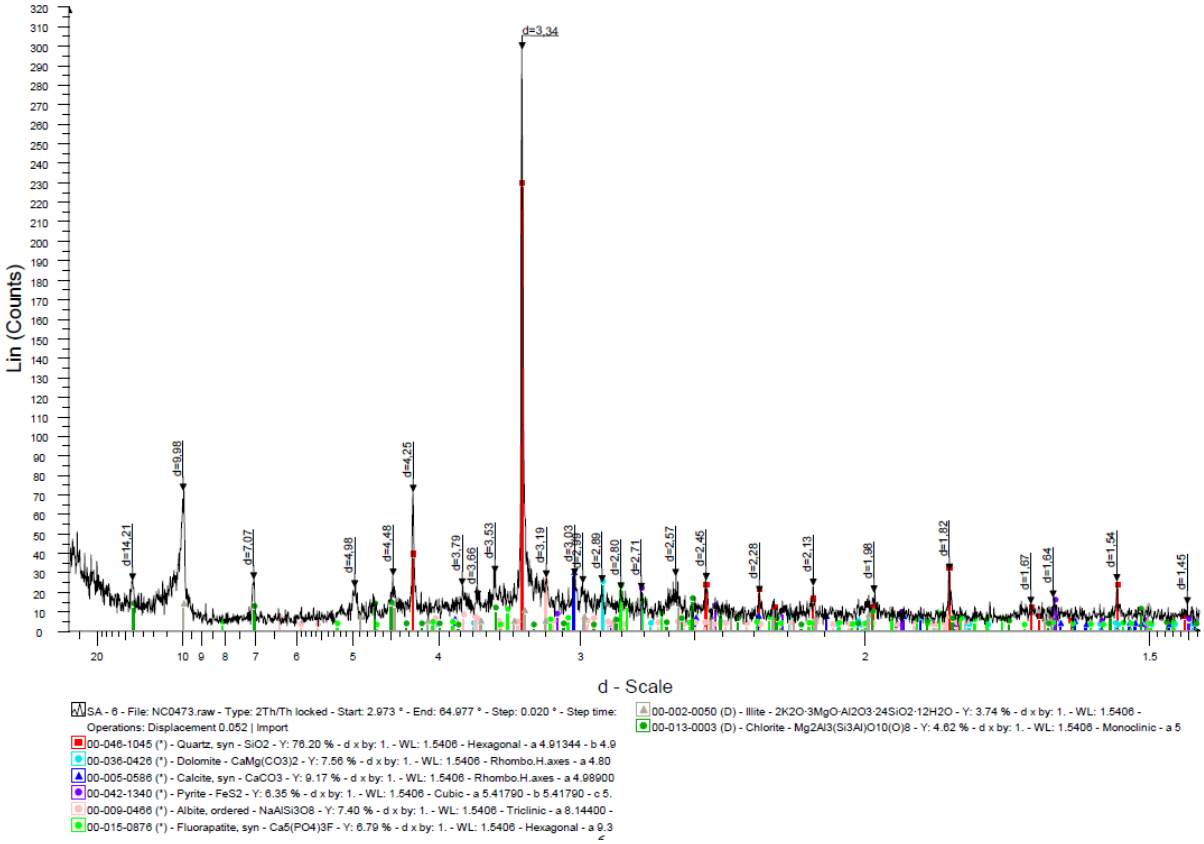
Lin (Counts)
d - Scale
d=3.34
d=14.21
d=9.98
d=7.07
d=4.98
d=4.48
d=4.25
d=3.79
d=3.66
d=3.53
d=3.19
d=3.03
d=2.98
d=2.89
d=2.80
d=2.71
d=2.57
d=2.45
d=2.28
d=2.13
d=1.98
d=1.82
d=1.67
d=1.64
d=1.54
d=1.45
SA - 6 - File: NC0473.raw - Type: 2Th/Th locked - Start: 2.973 ° - End: 64.977 ° - Step: 0.020 ° - Step time:
Operations: Displacement 0.052 | Import
00-046-1045 (*) - Quartz, syn - SiO2 - Y: 76.20 % - d x by: 1. - WL: 1.5406 - Hexagonal - a 4.91344 - b 4.9
00-036-0426 (*) - Dolomite - CaMg(CO3)2 - Y: 7.56 % - d x by: 1. - WL: 1.5406 - Rhombo.H.axes - a 4.80
00-005-0586 (*) - Calcite, syn - CaCO3 - Y: 9.17 % - d x by: 1. - WL: 1.5406 - Rhombo.H.axes - a 4.98900
00-042-1340 (*) - Pyrite - FeS2 - Y: 6.35 % - d x by: 1. - WL: 1.5406 - Cubic - a 5.41790 - b 5.41790 - c 5.
00-009-0466 (*) - Albite, ordered - NaAlSi3O8 - Y: 7.40 % - d x by: 1. - WL: 1.5406 - Triclinic - a 8.14400 -
00-015-0876 (*) - Fluorapatite, syn - Ca5(PO4)3F - Y: 6.79 % - d x by: 1. - WL: 1.5406 - Hexagonal - a 9.3
00-002-0050 (D) - Illite - 2K2O·3MgO·Al2O3·24SiO2·12H2O - Y: 3.74 % - d x by: 1. - WL: 1.5406 -
00-013-0003 (D) - Chlorite - Mg2Al3(Si3Al)O10(O)8 - Y: 4.62 % - d x by: 1. - WL: 1.5406 - Monoclinic - a 5

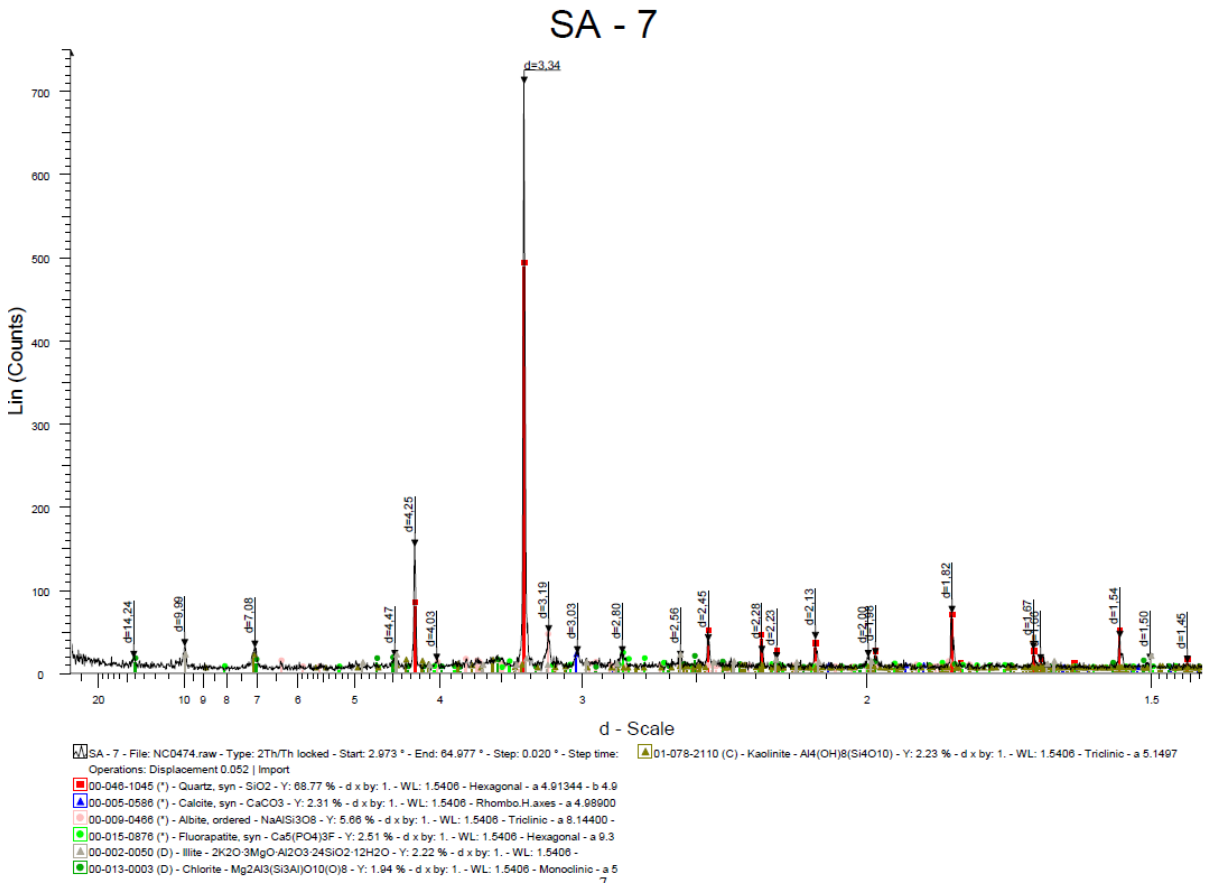
SA - 7
Lin (Counts)
d - Scale
d=3.34
d=4.25
d=14.24
d=9.99
d=7.08
d=4.47
d=4.03
d=3.19
d=3.03
d=2.80
d=2.56
d=2.45
d=2.28
d=2.23
d=2.13
d=2.00
d=1.98
d=1.82
d=1.67
d=1.60
d=1.54
d=1.50
d=1.45
SA - 7 - File: NC0474.raw - Type: 2Th/Th locked - Start: 2.973 ° - End: 64.977 ° - Step: 0.020 ° - Step time:
Operations: Displacement 0.052 | Import
00-046-1045 (*) - Quartz, syn - SiO2 - Y: 68.77 % - d x by: 1. - WL: 1.5406 - Hexagonal - a 4.91344 - b 4.9
00-005-0586 (*) - Calcite, syn - CaCO3 - Y: 2.31 % - d x by: 1. - WL: 1.5406 - Rhombo.H.axes - a 4.98900
00-009-0466 (*) - Albite, ordered - NaAlSi3O8 - Y: 5.66 % - d x by: 1. - WL: 1.5406 - Triclinic - a 8.14400 -
00-015-0876 (*) - Fluorapatite, syn - Ca5(PO4)3F - Y: 2.51 % - d x by: 1. - WL: 1.5406 - Hexagonal - a 9.3
00-002-0050 (D) - Illite - 2K2O·3MgO·Al2O3·24SiO2·12H2O - Y: 2.22 % - d x by: 1. - WL: 1.5406 -
00-013-0003 (D) - Chlorite - Mg2Al3(Si3Al)O10(O)8 - Y: 1.94 % - d x by: 1. - WL: 1.5406 - Monoclinic - a 5
01-078-2110 (C) - Kaolinite - Al4(OH)8(Si4O10) - Y: 2.23 % - d x by: 1. - WL: 1.5406 - Triclinic - a 5.1497

SA-8

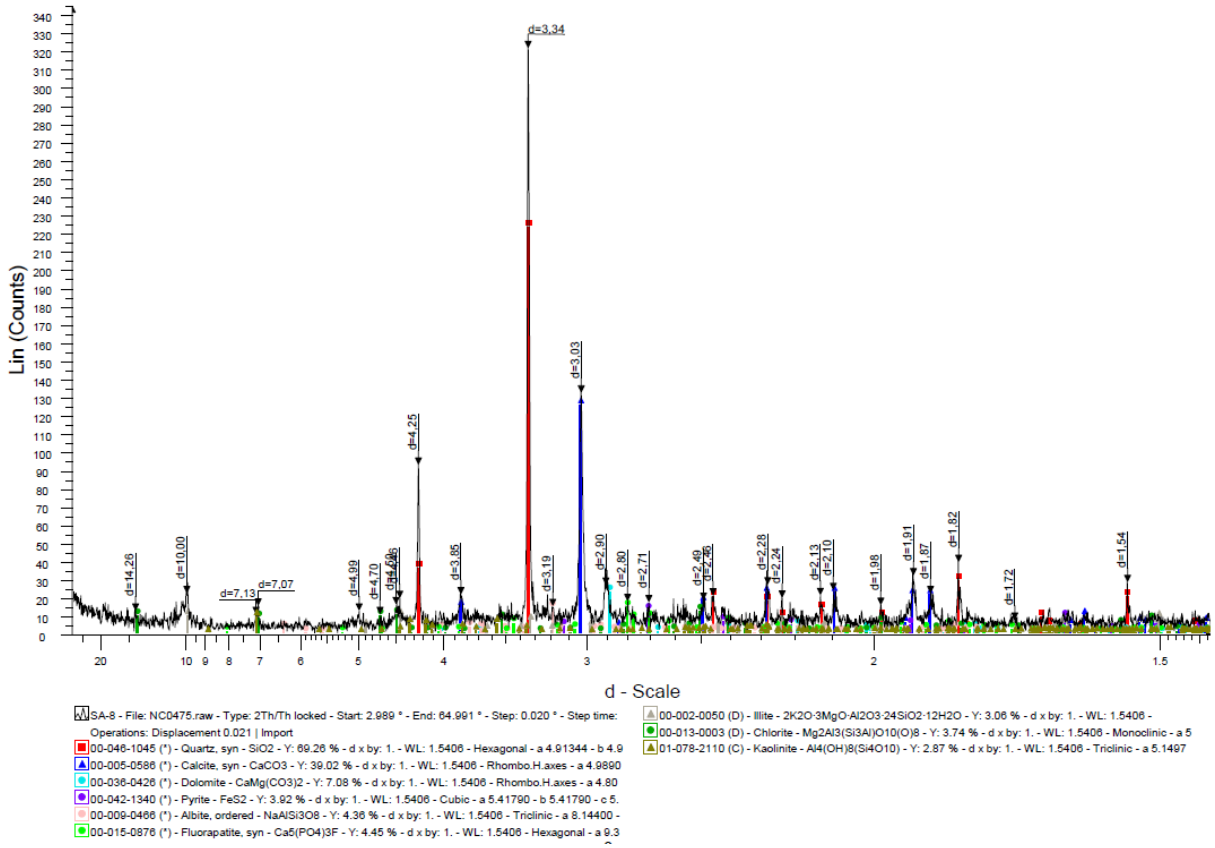
Lin (Counts)
d - Scale
d=3,34
d=4,25
d=3,03
d=14,26
d=10,00
d=7,13
d=7,07
d=4,99
d=4,70
d=3,85
d=3,19
d=2,90
d=2,80
d=2,71
d=2,49
d=2,45
d=2,28
d=2,24
d=2,13
d=2,10
d=1,98
d=1,91
d=1,87
d=1,82
d=1,72
d=1,54
SA-8 - File: NC0475.raw - Type: 2Th/Th locked - Start: 2.989 ° - End: 64.991 ° - Step: 0.020 ° - Step time:
Operations: Displacement 0.021 | Import
00-046-1045 (*) - Quartz, syn - SiO2 - Y: 69.26 % - d x by: 1. - WL: 1.5406 - Hexagonal - a 4.91344 - b 4.9
00-005-0586 (*) - Calcite, syn - CaCO3 - Y: 39.02 % - d x by: 1. - WL: 1.5406 - Rhombo.H.axes - a 4.9890
00-036-0426 (*) - Dolomite - CaMg(CO3)2 - Y: 7.08 % - d x by: 1. - WL: 1.5406 - Rhombo.H.axes - a 4.80
00-042-1340 (*) - Pyrite - FeS2 - Y: 3.92 % - d x by: 1. - WL: 1.5406 - Cubic - a 5.41790 - b 5.41790 - c 5.
00-009-0466 (*) - Albite, ordered - NaAlSi3O8 - Y: 4.36 % - d x by: 1. - WL: 1.5406 - Triclinic - a 8.14400 -
00-015-0876 (*) - Fluorapatite, syn - Ca5(PO4)3F - Y: 4.45 % - d x by: 1. - WL: 1.5406 - Hexagonal - a 9.3
00-002-0050 (D) - Illite - 2K2O·3MgO·Al2O3·24SiO2·12H2O - Y: 3.06 % - d x by: 1. - WL: 1.5406 -
00-013-0003 (D) - Chlorite - Mg2Al3(Si3Al)O10(O)8 - Y: 3.74 % - d x by: 1. - WL: 1.5406 - Monoclinic - a 5
01-078-2110 (C) - Kaolinite - Al4(OH)8(Si4O10) - Y: 2.87 % - d x by: 1. - WL: 1.5406 - Triclinic - a 5.1497

SA-10

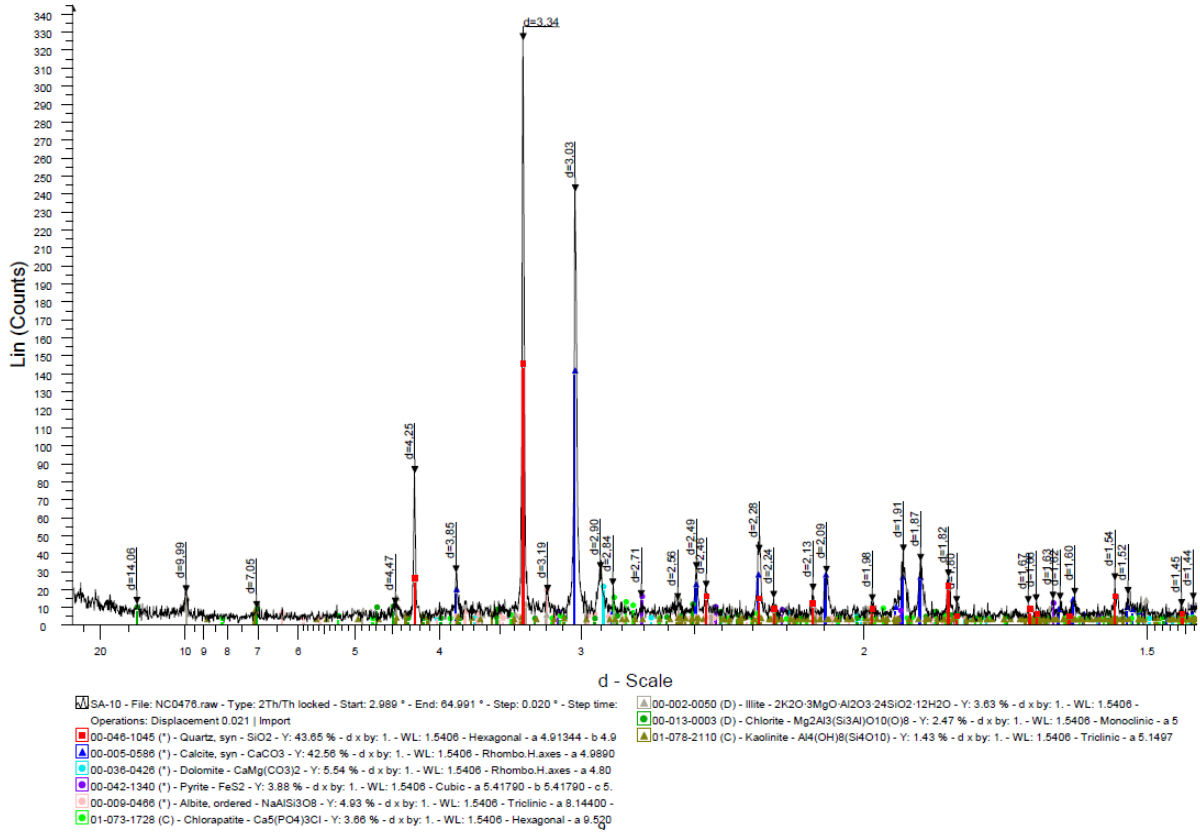
Lin (Counts)
d - Scale
d=3.34
d=3.03
d=4.25
d=14.06
d=9.99
d=7.05
d=4.47
d=3.85
d=3.19
d=2.90
d=2.84
d=2.71
d=2.96
d=2.49
d=2.46
d=2.28
d=2.24
d=2.13
d=2.09
d=1.98
d=1.91
d=1.87
d=1.82
d=1.60
d=1.54
d=1.52
d=1.45
d=1.44
SA-10 - File: NC0476.raw - Type: 2Th/Th locked - Start: 2.989 ° - End: 64.991 ° - Step: 0.020 ° - Step time:
Operations: Displacement 0.021 | Import
00-046-1045 (*) - Quartz, syn - SiO2 - Y: 43.65 % - d x by: 1. - WL: 1.5406 - Hexagonal - a 4.91344 - b 4.9
00-005-0586 (*) - Calcite, syn - CaCO3 - Y: 42.56 % - d x by: 1. - WL: 1.5406 - Rhombo.H.axes - a 4.9890
00-036-0426 (*) - Dolomite - CaMg(CO3)2 - Y: 5.54 % - d x by: 1. - WL: 1.5406 - Rhombo.H.axes - a 4.80
00-042-1340 (*) - Pyrite - FeS2 - Y: 3.88 % - d x by: 1. - WL: 1.5406 - Cubic - a 5.41790 - b 5.41790 - c 5.
00-009-0466 (*) - Albite, ordered - NaAlSi3O8 - Y: 4.93 % - d x by: 1. - WL: 1.5406 - Triclinic - a 8.14400 -
01-073-1728 (C) - Chlorapatite - Ca5(PO4)3Cl - Y: 3.66 % - d x by: 1. - WL: 1.5406 - Hexagonal - a 9.520
00-002-0050 (D) - Illite - 2K2O·3MgO·Al2O3·24SiO2·12H2O - Y: 3.63 % - d x by: 1. - WL: 1.5406 -
00-013-0003 (D) - Chlorite - Mg2Al3(Si3Al)O10(O)8 - Y: 2.47 % - d x by: 1. - WL: 1.5406 - Monoclinic - a 5
01-078-2110 (C) - Kaolinite - Al4(OH)8(Si4O10) - Y: 1.43 % - d x by: 1. - WL: 1.5406 - Triclinic - a 5.1497

Appendix C – XRD of random powder samples < 2 µm fraction clays

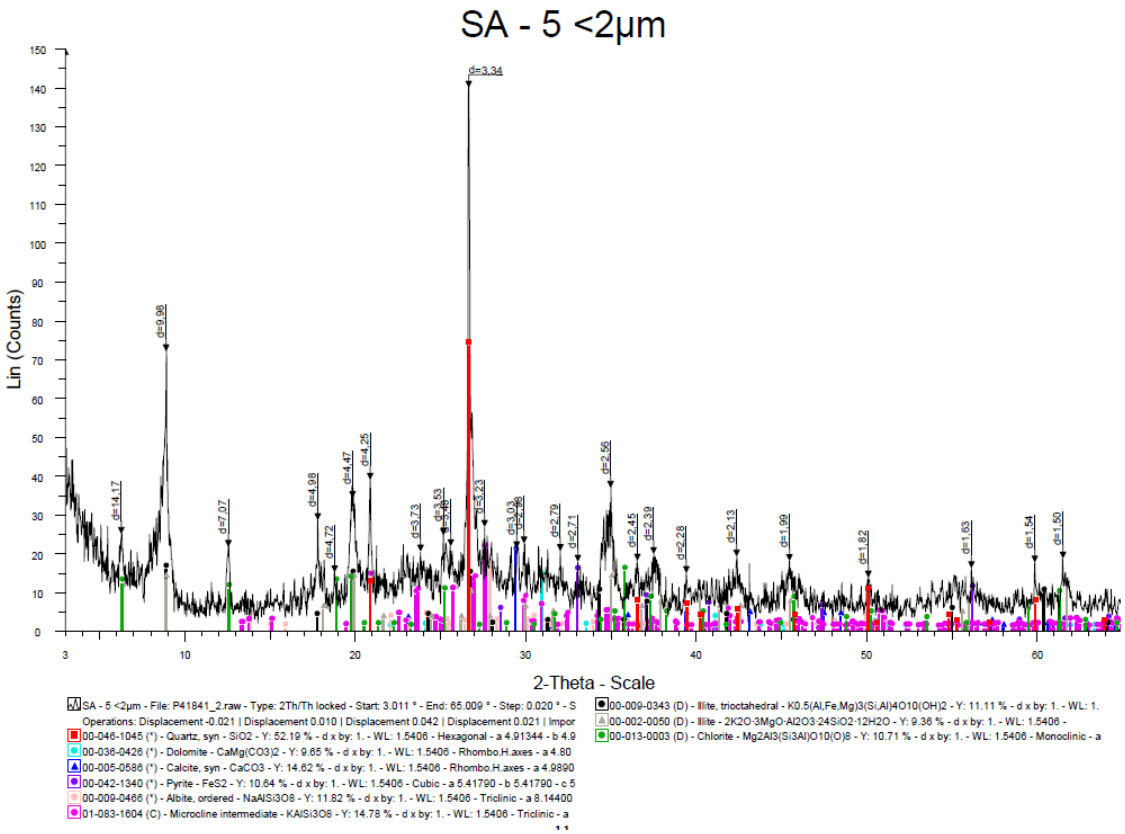

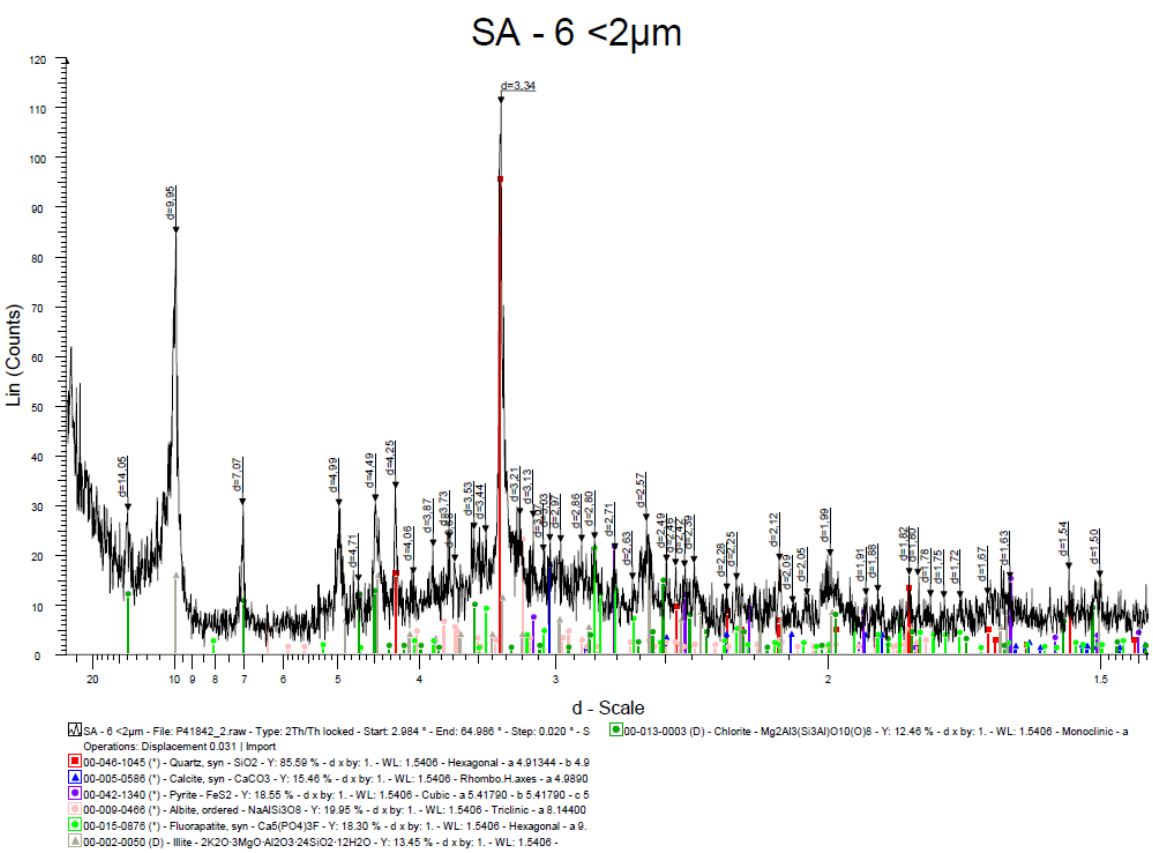
SA - 6 <2µm
Lin (Counts)
d - Scale
d=14.05
d=9.95
d=7.07
d=4.99
d=4.71
d=4.49
d=4.25
d=4.06
d=3.87
d=3.73
d=3.53
d=3.44
d=3.34
d=3.21
d=3.13
d=3.03
d=2.97
d=2.86
d=2.80
d=2.71
d=2.63
d=2.57
d=2.49
d=2.46
d=2.42
d=2.39
d=2.28
d=2.25
d=2.12
d=2.09
d=2.05
d=1.99
d=1.91
d=1.88
d=1.82
d=1.80
d=1.76
d=1.75
d=1.72
d=1.67
d=1.63
d=1.54
d=1.50
SA - 6 <2µm - File: P41842_2.raw - Type: 2Th/Th locked - Start: 2.984 ° - End: 64.986 ° - Step: 0.020 ° - S
Operations: Displacement 0.031 | Import
00-046-1045 (*) - Quartz, syn - SiO2 - Y: 85.59 % - d x by: 1. - WL: 1.5406 - Hexagonal - a 4.91344 - b 4.9
00-005-0586 (*) - Calcite, syn - CaCO3 - Y: 15.46 % - d x by: 1. - WL: 1.5406 - Rhombo.H.axes - a 4.9890
00-042-1340 (*) - Pyrite - FeS2 - Y: 18.55 % - d x by: 1. - WL: 1.5406 - Cubic - a 5.41790 - b 5.41790 - c 5
00-009-0466 (*) - Albite, ordered - NaAlSi3O8 - Y: 19.95 % - d x by: 1. - WL: 1.5406 - Triclinic - a 8.14400
00-015-0876 (*) - Fluorapatite, syn - Ca5(PO4)3F - Y: 18.30 % - d x by: 1. - WL: 1.5406 - Hexagonal - a 9.
00-002-0050 (D) - Illite - 2K2O·3MgO·Al2O3·24SiO2·12H2O - Y: 13.45 % - d x by: 1. - WL: 1.5406 -
00-013-0003 (D) - Chlorite - Mg2Al3(Si3Al)O10(O)8 - Y: 12.46 % - d x by: 1. - WL: 1.5406 - Monoclinic - a

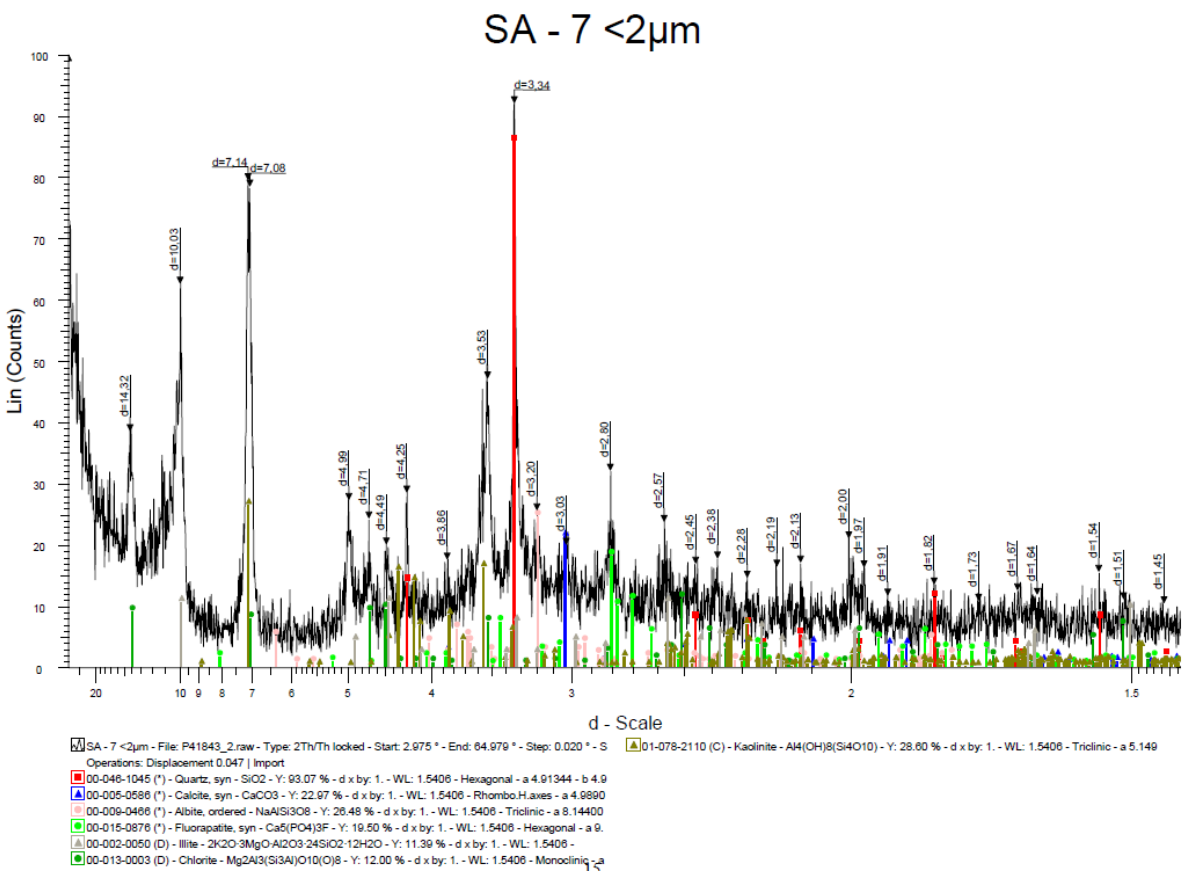
SA - 7 <2µm
Lin (Counts)
d - Scale
d=14.32
d=10.03
d=7.14
d=7.08
d=4.99
d=4.71
d=4.49
d=4.25
d=3.86
d=3.53
d=3.34
d=3.20
d=3.03
d=2.80
d=2.57
d=2.45
d=2.38
d=2.28
d=2.19
d=2.13
d=2.00
d=1.97
d=1.91
d=1.82
d=1.73
d=1.67
d=1.64
d=1.54
d=1.51
d=1.45
SA - 7 <2µm - File: P41843_2.raw - Type: 2Th/Th locked - Start: 2.975 ° - End: 64.979 ° - Step: 0.020 ° - S
Operations: Displacement 0.047 | Import
00-046-1045 (*) - Quartz, syn - SiO2 - Y: 93.07 % - d x by: 1. - WL: 1.5406 - Hexagonal - a 4.91344 - b 4.9
00-005-0586 (*) - Calcite, syn - CaCO3 - Y: 22.97 % - d x by: 1. - WL: 1.5406 - Rhombo.H.axes - a 4.9890
00-009-0466 (*) - Albite, ordered - NaAlSi3O8 - Y: 26.48 % - d x by: 1. - WL: 1.5406 - Triclinic - a 8.14400
00-015-0876 (*) - Fluorapatite, syn - Ca5(PO4)3F - Y: 19.50 % - d x by: 1. - WL: 1.5406 - Hexagonal - a 9.
00-002-0050 (D) - Illite - 2K2O·3MgO·Al2O3·24SiO2·12H2O - Y: 11.39 % - d x by: 1. - WL: 1.5406 -
00-013-0003 (D) - Chlorite - Mg2Al3(Si3Al)O10(O)8 - Y: 12.00 % - d x by: 1. - WL: 1.5406 - Monoclinic - a
01-078-2110 (C) - Kaolinite - Al4(OH)8(Si4O10) - Y: 28.60 % - d x by: 1. - WL: 1.5406 - Triclinic - a 5.149

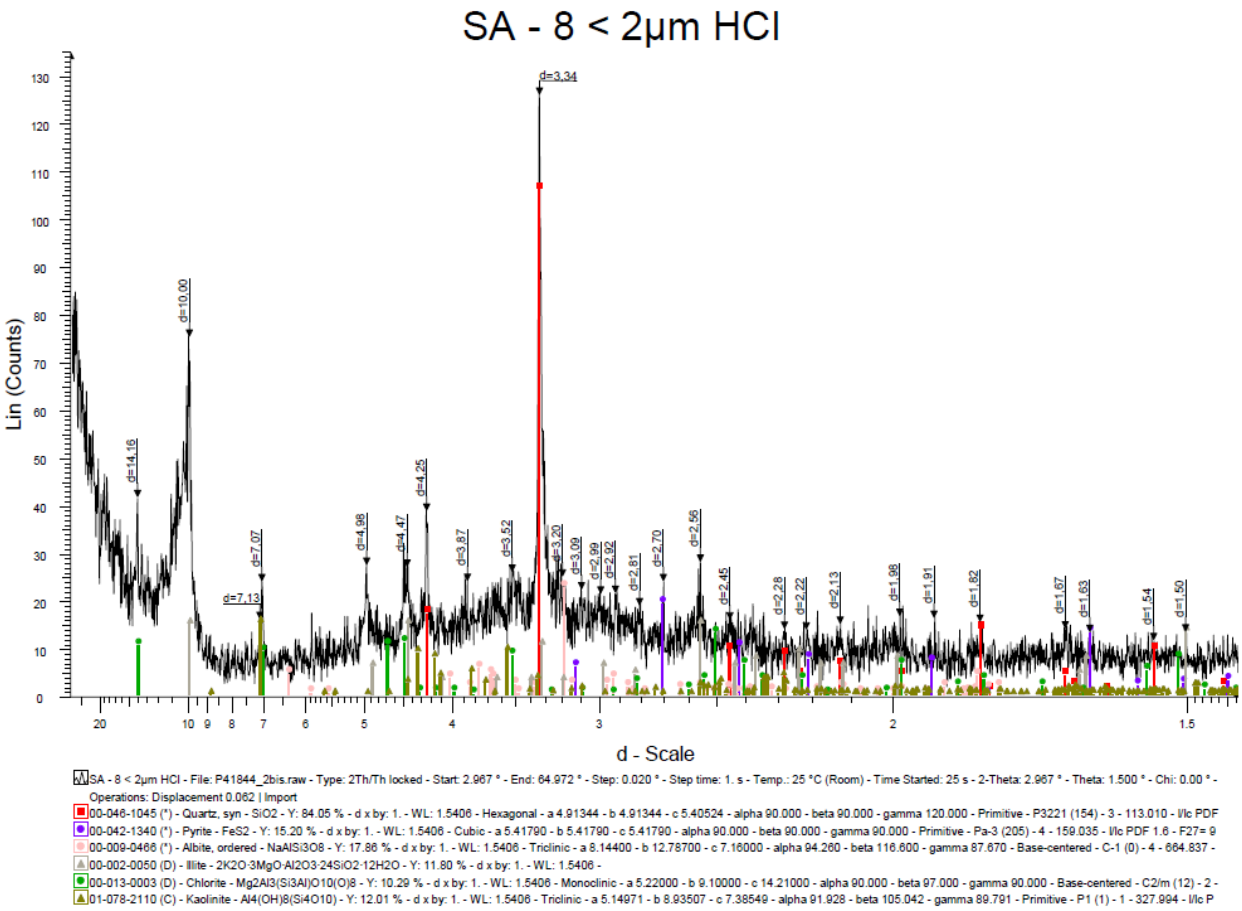
SA - 8 < 2µm HCl
Lin (Counts)
d - Scale
d=3,34
d=10,00
d=14,16
d=7,13
d=7,07
d=4,98
d=4,47
d=4,25
d=3,87
d=3,52
d=3,20
d=3,09
d=2,99
d=2,92
d=2,81
d=2,70
d=2,56
d=2,45
d=2,28
d=2,22
d=2,13
d=1,98
d=1,91
d=1,82
d=1,67
d=1,63
d=1,54
d=1,50
SA - 8 < 2µm HCl - File: P41844_2bis.raw - Type: 2Th/Th locked - Start: 2.967 ° - End: 64.972 ° - Step: 0.020 ° - Step time: 1. s - Temp.: 25 °C (Room) - Time Started: 25 s - 2-Theta: 2.967 ° - Theta: 1.500 ° - Chi: 0.00 ° -
Operations: Displacement 0.062 | Import
00-046-1045 (*) - Quartz, syn - SiO2 - Y: 84.05 % - d x by: 1. - WL: 1.5406 - Hexagonal - a 4.91344 - b 4.91344 - c 5.40524 - alpha 90.000 - beta 90.000 - gamma 120.000 - Primitive - P3221 (154) - 3 - 113.010 - I/Ic PDF
00-042-1340 (*) - Pyrite - FeS2 - Y: 15.20 % - d x by: 1. - WL: 1.5406 - Cubic - a 5.41790 - b 5.41790 - c 5.41790 - alpha 90.000 - beta 90.000 - gamma 90.000 - Primitive - Pa-3 (205) - 4 - 159.035 - I/Ic PDF 1.6 - F27= 9
00-009-0466 (*) - Albite, ordered - NaAlSi3O8 - Y: 17.86 % - d x by: 1. - WL: 1.5406 - Triclinic - a 8.14400 - b 12.78700 - c 7.16000 - alpha 94.260 - beta 116.600 - gamma 87.670 - Base-centered - C-1 (0) - 4 - 664.837 -
00-002-0050 (D) - Illite - 2K2O·3MgO·Al2O3·24SiO2·12H2O - Y: 11.80 % - d x by: 1. - WL: 1.5406 -
00-013-0003 (D) - Chlorite - Mg2Al3(Si3Al)O10(O)8 - Y: 10.29 % - d x by: 1. - WL: 1.5406 - Monoclinic - a 5.22000 - b 9.10000 - c 14.21000 - alpha 90.000 - beta 97.000 - gamma 90.000 - Base-centered - C2/m (12) - 2 -
01-078-2110 (C) - Kaolinite - Al4(OH)8(Si4O10) - Y: 12.01 % - d x by: 1. - WL: 1.5406 - Triclinic - a 5.14971 - b 8.93507 - c 7.38549 - alpha 91.928 - beta 105.042 - gamma 89.791 - Primitive - P1 (1) - 1 - 327.994 - I/Ic P

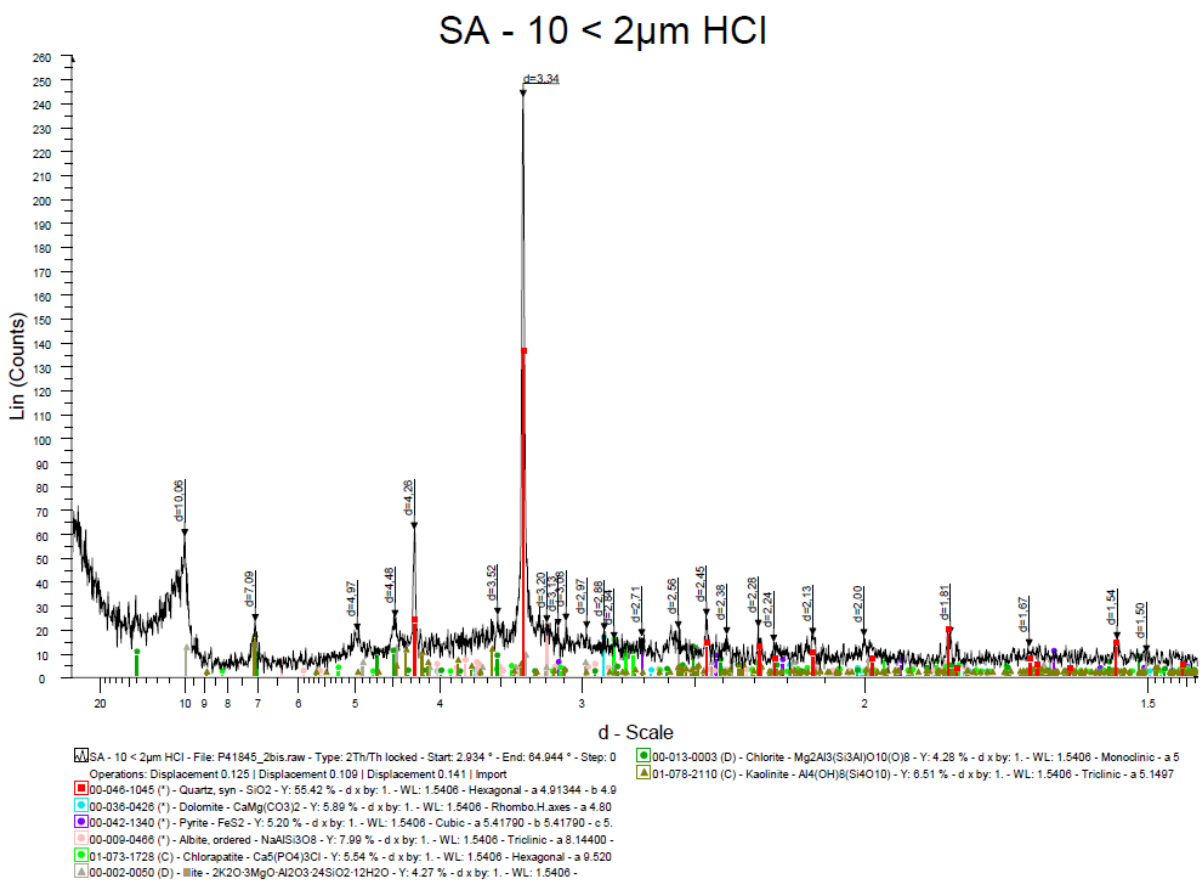
SA - 10 < 2µm HCl
Lin (Counts)
d - Scale
d=10.06
d=7.09
d=4.97
d=4.46
d=4.26
d=3.52
d=3.34
d=3.20
d=3.06
d=2.97
d=2.88
d=2.71
d=2.55
d=2.45
d=2.38
d=2.28
d=2.24
d=2.13
d=2.00
d=1.81
d=1.67
d=1.54
d=1.50
SA - 10 < 2µm HCl - File: P41845_2bis.raw - Type: 2Th/Th locked - Start: 2.934 ° - End: 64.944 ° - Step: 0
Operations: Displacement 0.125 | Displacement 0.109 | Displacement 0.141 | Import
00-046-1045 (*) - Quartz, syn - SiO2 - Y: 55.42 % - d x by: 1. - WL: 1.5406 - Hexagonal - a 4.91344 - b 4.9
00-036-0426 (*) - Dolomite - CaMg(CO3)2 - Y: 5.89 % - d x by: 1. - WL: 1.5406 - Rhombo.H.axes - a 4.80
00-042-1340 (*) - Pyrite - FeS2 - Y: 5.20 % - d x by: 1. - WL: 1.5406 - Cubic - a 5.41790 - b 5.41790 - c 5.
00-009-0466 (*) - Albite, ordered - NaAlSi3O8 - Y: 7.99 % - d x by: 1. - WL: 1.5406 - Triclinic - a 8.14400 -
01-073-1728 (C) - Chlorapatite - Ca5(PO4)3Cl - Y: 5.54 % - d x by: 1. - WL: 1.5406 - Hexagonal - a 9.520
00-002-0050 (D) - Illite - 2K2O·3MgO·Al2O3·24SiO2·12H2O - Y: 4.27 % - d x by: 1. - WL: 1.5406 -
00-013-0003 (D) - Chlorite - Mg2Al3(Si3Al)O10(O)8 - Y: 4.28 % - d x by: 1. - WL: 1.5406 - Monoclinic - a 5
01-078-2110 (C) - Kaolinite - Al4(OH)8(Si4O10) - Y: 6.51 % - d x by: 1. - WL: 1.5406 - Triclinic - a 5.1497

Appendix D – XRD of d_{060} plane

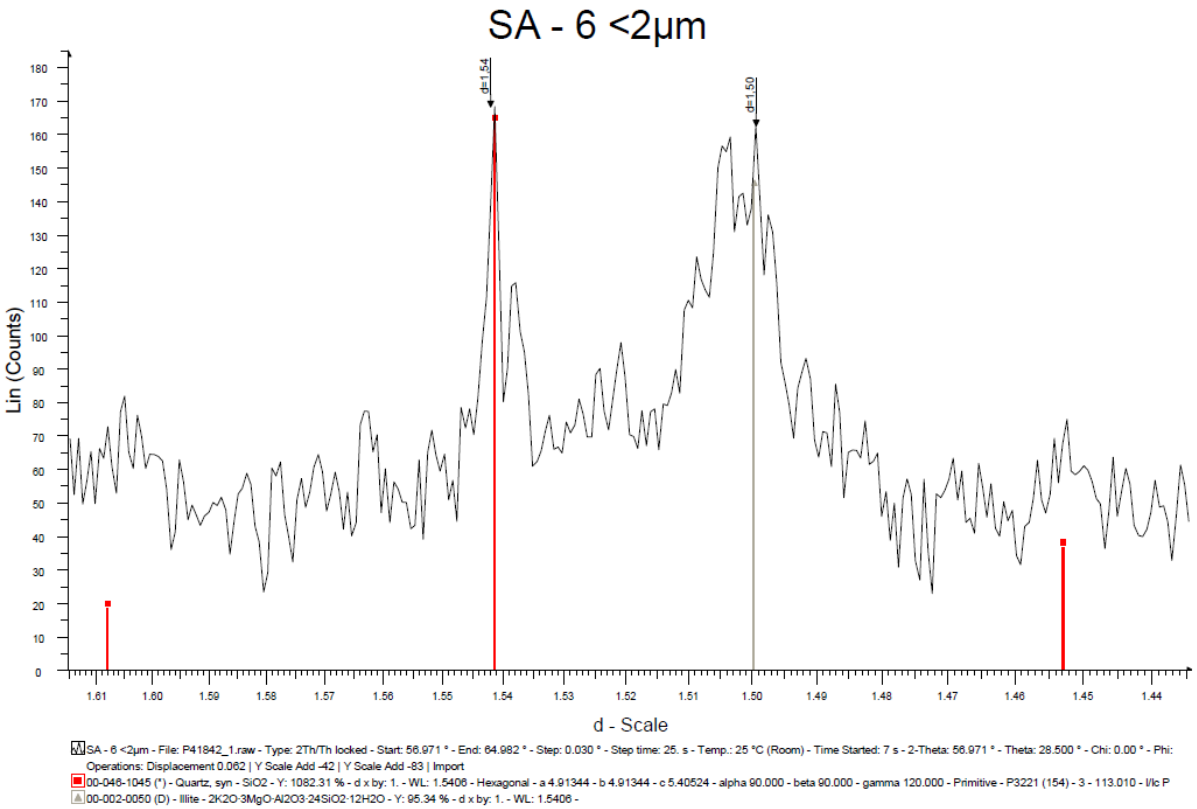

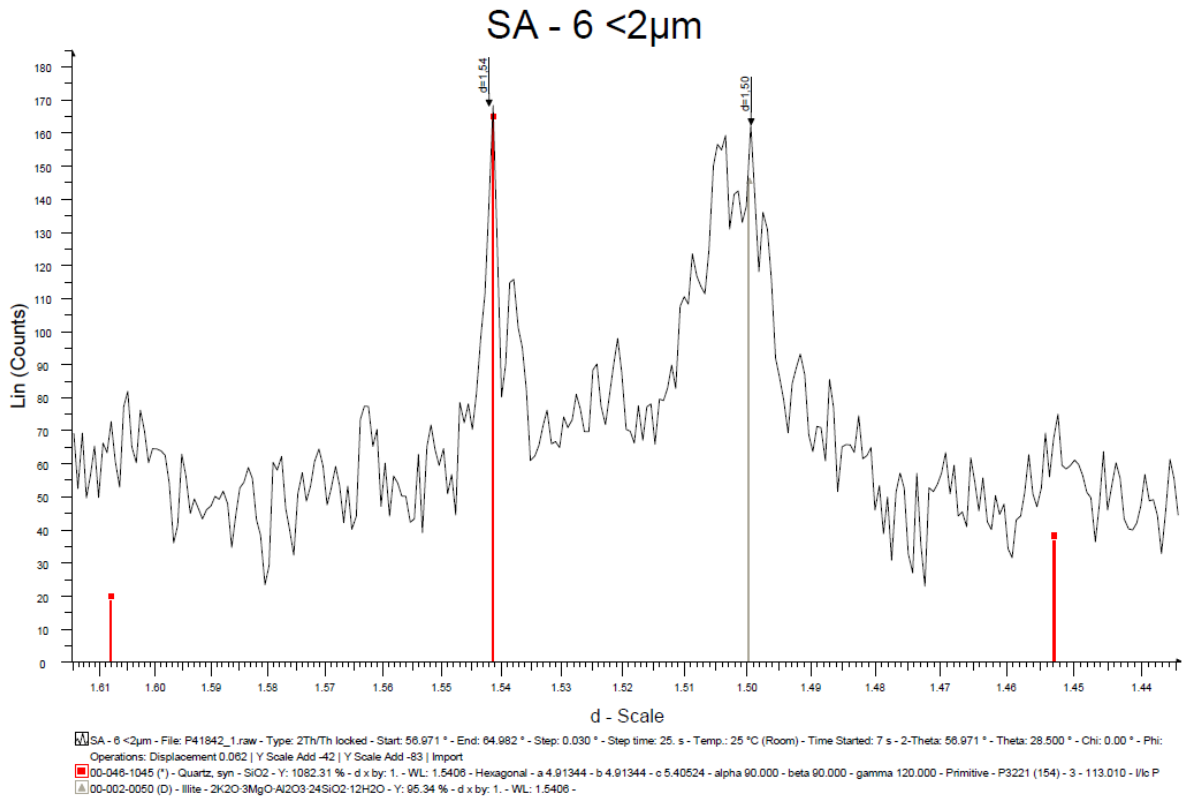
SA - 6 <2µm
d=1.54
d=1.50
Lin (Counts)
d - Scale
SA - 6 <2µm - File: P41842_1.raw - Type: 2Th/Th locked - Start: 56.971 ° - End: 64.982 ° - Step: 0.030 ° - Step time: 25. s - Temp.: 25 °C (Room) - Time Started: 7 s - 2-Theta: 56.971 ° - Theta: 28.500 ° - Chi: 0.00 ° - Phi:
Operations: Displacement 0.062 | Y Scale Add -42 | Y Scale Add -83 | Import
00-046-1045 (*) - Quartz, syn - SiO2 - Y: 1082.31 % - d x by: 1. - WL: 1.5406 - Hexagonal - a 4.91344 - b 4.91344 - c 5.40524 - alpha 90.000 - beta 90.000 - gamma 120.000 - Primitive - P3221 (154) - 3 - 113.010 - I/Ic P
00-002-0050 (D) - Illite - 2K2O·3MgO·Al2O3·24SiO2·12H2O - Y: 95.34 % - d x by: 1. - WL: 1.5406 -

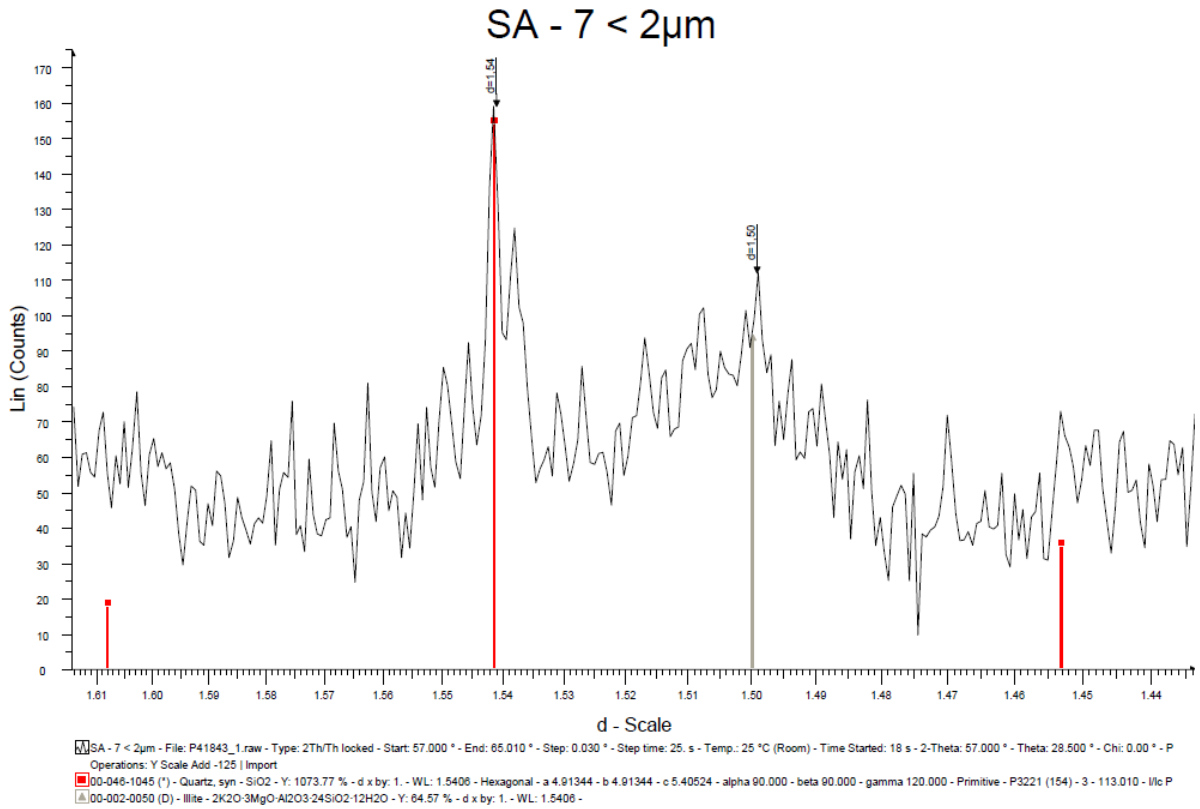
SA - 7 < 2µm
Lin (Counts)
d - Scale
d=1.54
d=1.50
SA - 7 < 2µm - File: P41843_1.raw - Type: 2Th/Th locked - Start: 57.000 ° - End: 65.010 ° - Step: 0.030 ° - Step time: 25. s - Temp.: 25 °C (Room) - Time Started: 18 s - 2-Theta: 57.000 ° - Theta: 28.500 ° - Chi: 0.00 ° - P
Operations: Y Scale Add -125 | Import
00-046-1045 (*) - Quartz, syn - SiO2 - Y: 1073.77 % - d x by: 1. - WL: 1.5406 - Hexagonal - a 4.91344 - b 4.91344 - c 5.40524 - alpha 90.000 - beta 90.000 - gamma 120.000 - Primitive - P3221 (154) - 3 - 113.010 - I/Ic P
00-002-0050 (D) - Illite - 2K2O·3MgO·Al2O3·24SiO2·12H2O - Y: 64.57 % - d x by: 1. - WL: 1.5406 -

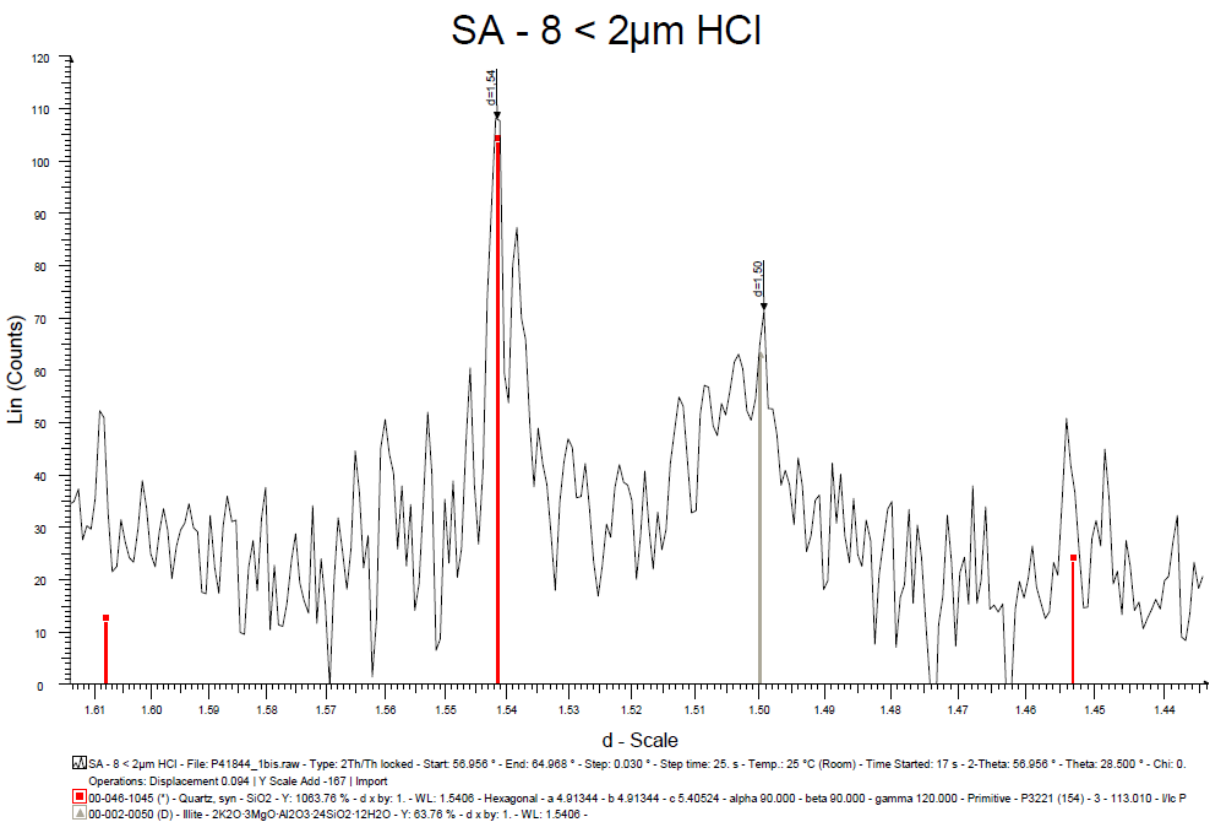
SA - 8 < 2µm HCl
Lin (Counts)
d - Scale
d=1.54
d=1.50
SA - 8 < 2µm HCl - File: P41844_1bis.raw - Type: 2Th/Th locked - Start: 56.956 ° - End: 64.968 ° - Step: 0.030 ° - Step time: 25. s - Temp.: 25 °C (Room) - Time Started: 17 s - 2-Theta: 56.956 ° - Theta: 28.500 ° - Chi: 0.
Operations: Displacement 0.094 | Y Scale Add -167 | Import
00-046-1045 (*) - Quartz, syn - SiO2 - Y: 1063.76 % - d x by: 1. - WL: 1.5406 - Hexagonal - a 4.91344 - b 4.91344 - c 5.40524 - alpha 90.000 - beta 90.000 - gamma 120.000 - Primitive - P3221 (154) - 3 - 113.010 - I/Ic P
00-002-0050 (D) - Illite - 2K2O·3MgO·Al2O3·24SiO2·12H2O - Y: 63.76 % - d x by: 1. - WL: 1.5406 -

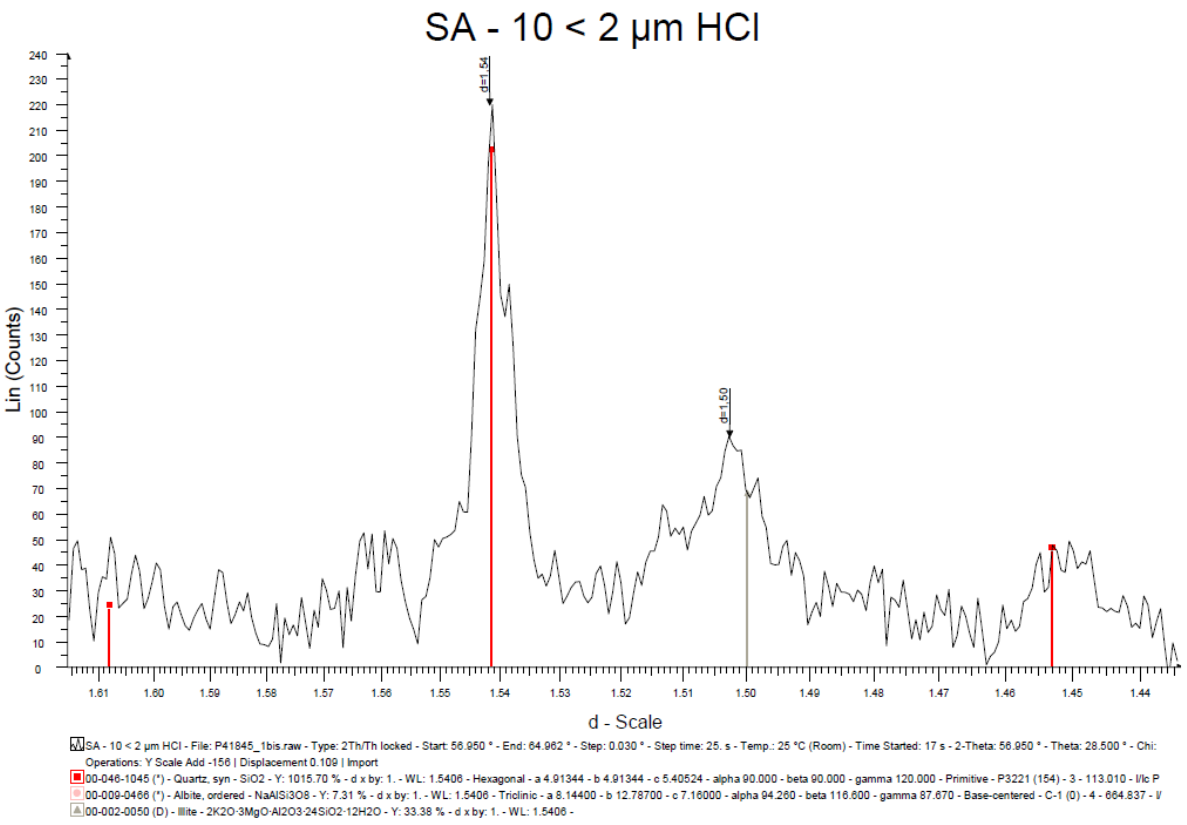
SA - 10 < 2 µm HCl
Lin (Counts)
d - Scale
d=1.54
d=1.50
SA - 10 < 2 µm HCl - File: P41845_1bis.raw - Type: 2Th/Th locked - Start: 56.950 ° - End: 64.962 ° - Step: 0.030 ° - Step time: 25. s - Temp.: 25 °C (Room) - Time Started: 17 s - 2-Theta: 56.950 ° - Theta: 28.500 ° - Chi:
Operations: Y Scale Add -156 | Displacement 0.109 | Import
00-046-1045 (*) - Quartz, syn - SiO2 - Y: 1015.70 % - d x by: 1. - WL: 1.5406 - Hexagonal - a 4.91344 - b 4.91344 - c 5.40524 - alpha 90.000 - beta 90.000 - gamma 120.000 - Primitive - P3221 (154) - 3 - 113.010 - I/Ic P
00-009-0466 (*) - Albite, ordered - NaAlSi3O8 - Y: 7.31 % - d x by: 1. - WL: 1.5406 - Triclinic - a 8.14400 - b 12.78700 - c 7.16000 - alpha 94.260 - beta 116.600 - gamma 87.670 - Base-centered - C-1 (0) - 4 - 664.837 - I/
00-002-0050 (D) - Illite - 2K2O·3MgO·Al2O3·24SiO2·12H2O - Y: 33.38 % - d x by: 1. - WL: 1.5406 -

Appendix E – SEM images

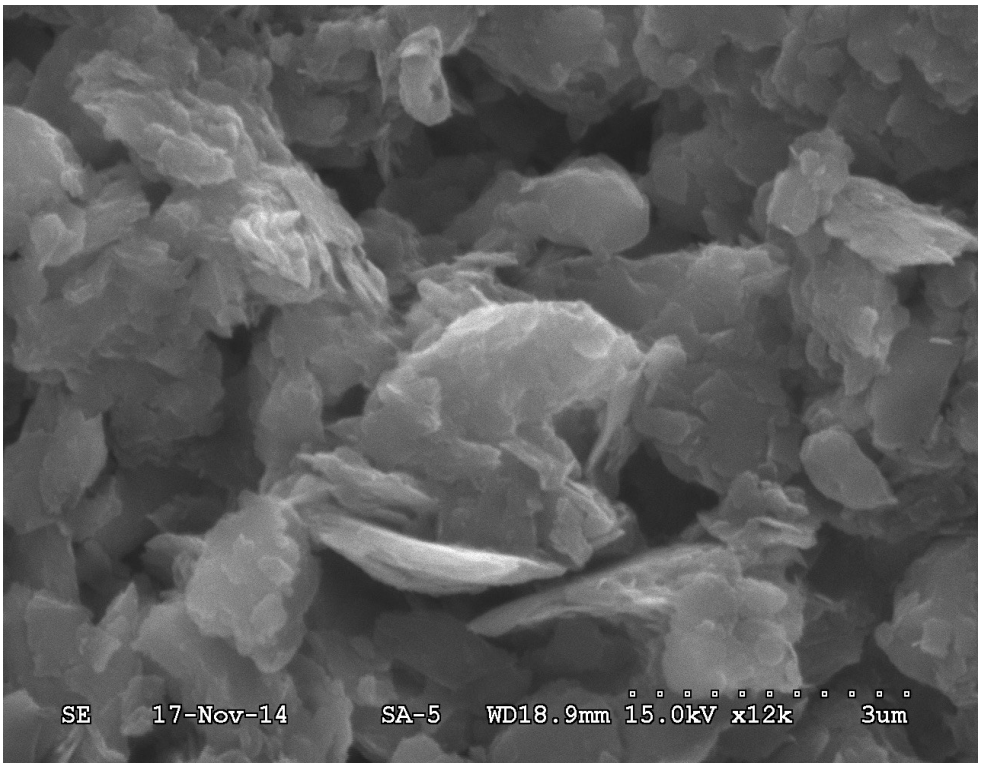

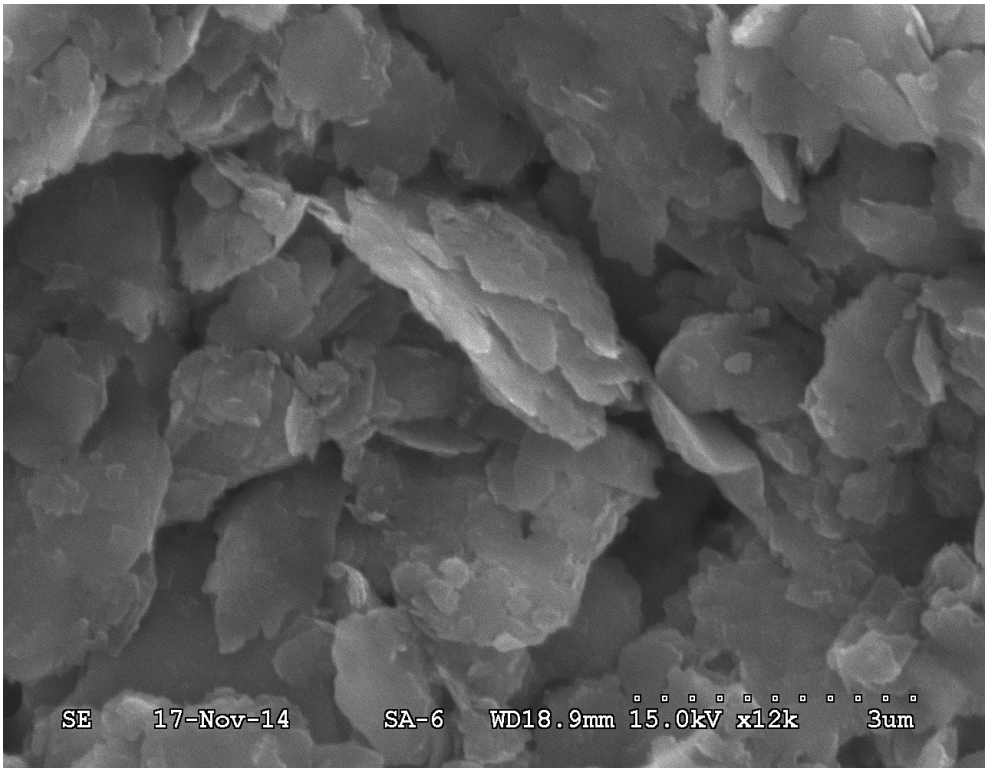
SE 17-Nov-14 SA-6 WD18.9mm 15.0kV x12k 3um

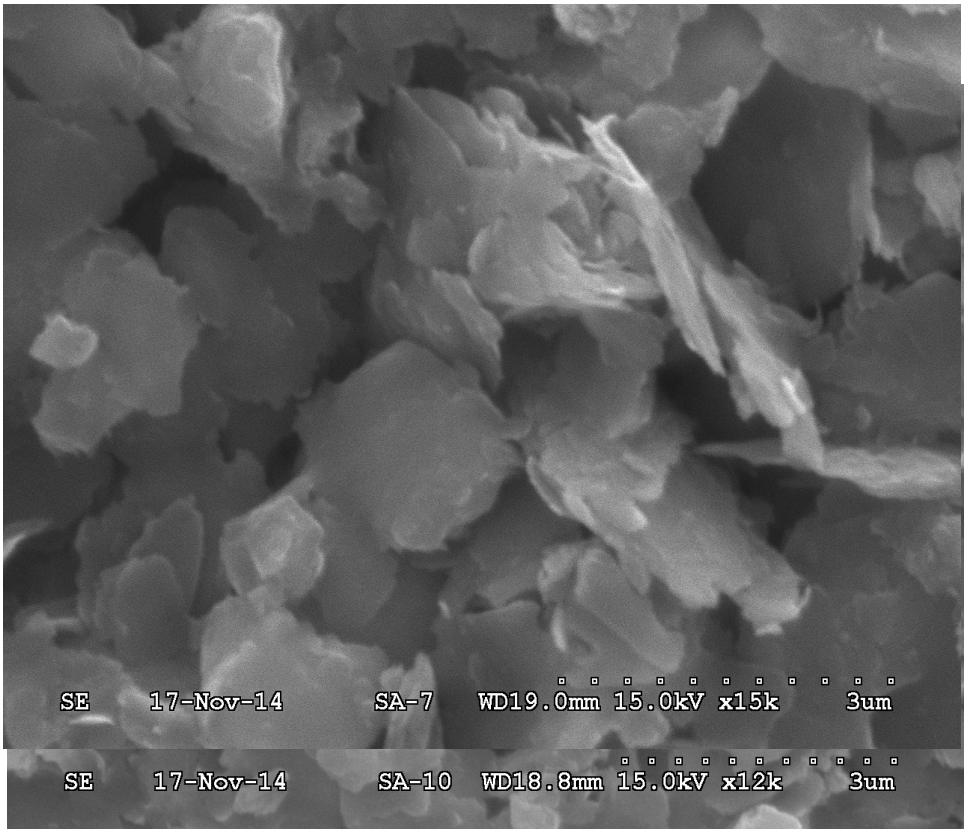
SE 17-Nov-14 SA-7 WD19.0mm 15.0kV x15k 3um
SE 17-Nov-14 SA-10 WD18.8mm 15.0kV x12k 3um